5-2013

An Examination of the Mechanisms and Environments Supportive of Bow Echo Mesovortex Genesis

George Limpert
University of Nebraska-Lincoln, george.limpert@unl.edu

AN EXAMINATION OF THE MECHANISMS AND ENVIRONMENTS SUPPORTIVE OF BOW ECHO MESOVORTEX GENESIS

by

George Limpert

A DISSERTATION

Presented to the Faculty of

The Graduate College at the University of Nebraska

In Partial Fulfillment of Requirements

For the Degree of Doctor of Philosophy

Major: Earth and Atmospheric Sciences

Under the Supervision of Professor Adam Houston

Lincoln, Nebraska

May, 2013

AN EXAMINATION OF THE MECHANISMS AND ENVIRONMENTS SUPPORTIVE OF BOW ECHO MESOVORTEX GENESIS

George Limpert, Ph.D.

University of Nebraska, 2013

Adviser: Adam Houston

Low-level mesovortices are associated with enhanced surface wind gusts and high-end wind damage in quasi-linear thunderstorms. Although damage associated with mesovortices can approach that of moderately strong tornadoes, skill in forecasting mesovortices is low. The overarching goal of this work is to understand mesovortices and how they develop, to improve the skill in forecasting them. This was done by developing a climatology of mesovortices, which required a tracking algorithm, and numerical simulations were conducted to answer questions that could not be answered through the observational data. A climatology of mesovortices was constructed from 44 events during 2009 and 2010 to examine mesovortex characteristics and origins. Approximately 60% of the mesovortices were cyclonic and were longer-lived and stronger at low levels than the anticyclonic mesovortices. A barotropic mechanism that redistributes ambient low-level vorticity was found to generate numerous cyclonic mesovortices in some events with strong vertical shear over lowest 500 m. The modeling component revealed that vorticity is generated in a region of strong horizontal shear between the ambient low-level winds and flow within the cold pool, and concentrated into mesovortices by releasing shearing instability. Upward tilting of baroclinic vorticity was found to generate mesovortices above the cold pool but did not produce significant vorticity near the surface. Low-level

mesovortices developed when the updraft remained near the gust front instead of advecting rearward. Cold air is lifted by the updraft and moves rearward and descends, tilting down vorticity atop the cold pool and generating near-surface mesovortices. The initial downward tilting is large for moderate and strong cold pools where there is substantial horizontal vorticity. Stretching of vertical vorticity intensifies the mesovortices and produces the strongest vortices where negative buoyancy in the cold pool is not too strong. Presented in this paper is an algorithm for the tracking of mesovortices across multiple radar domains, a climatology of bow echo mesovortices, and a series of model simulations to evaluate the stability hypothesis.

Computational resources were provided by the University of Nebraska Holland Computing Center. The development of AALTO was supported by the National Science Foundation award AGS-0758509. Partial funding was provided by a grant-in-aid from the Center for Great Plains Studies at the University of Nebraska-Lincoln. Valliappa Lakshmanan licensed the Warning Decision Support System—Integrated Information for use in portions of this research.

Acknowledgments

First and foremost, I would like to acknowledge and thank my Lord and Saivior Jesus Christ. There are many people I would like to acknowledge who supported me by encouraging me to complete my dissertation and making graduate school an enjoyable experience for me. In fact, there are too many to name here, but I'll do my best. I'd like to thank my parents, George Limpert and Rosanna Limpert, for assisting me in many ways with surviving graduate school. I want to thank my committee, Dr. Michael Hayes (M-I-Z), Dr. Robert Oglesby, Dr. Clinton Rowe, and especially my adviser, Dr. Adam Houston. I also want to acknowledge Noah Lock for collaborating with me on many aspects of my research and for not arguing with me that Mizzou is better than kU. I'd like to thank a few of my friends from the University of Missouri for collaborating with me on various projects that I found enjoyable and gave me the opportunity to explore topics that went beyond my doctoral research, as well as encouraging me through graduate school. These people include Dr. Anthony Lupo, Dr. Neil Fox, Steve Lack, Katy McCullough (sorry, can't join you in rooting for the Reds, though), Brittany Quick-Warner, and Jeff La Montia (sorry, you're still much more of a Husker fan than I am. I want to thank Eric Holt for encouraging me to spend many late nights in the computer lab working when I wanted to be at home watching ESPN and for his love of all things Mountain Dew, tree rat, and mythical bird. I definitely want to acknowledge many of my friends from the UNL Newman Center including Alli Harvey, Will Green, Gracie Morin, Matt Perlinger, Fr. Ben Holdren, Fr. Robert Matya, Logan Burda, and so many others for welcoming me and giving me many reasons to get out of the office, go sing, have fun,

and strengthen my relationship with God. I'd like to thank some of my fellow graduate students who made me feel welcome and supported me in getting through the doctoral program including Amy Kessner, Tim Hubbard, Alex Gibbs, David Peterson, and Xiaoguang Xu. I also want to thank many of the undergrads, especially Casey Griffin and Andrew Kalin, and Carlie McAlister for working with me on the Nebraska Storm Chase Team and putting up with my many obnoxious antics. I'm sure I haven't thanked everyone I should, because this would take several pages, but know that if I haven't mentioned you by name, I still appreciate the things you've done. M-I-Z! S-E-C!

Table of Contents

Chapter 1: Introduction 1

Chapter 2: The Advanced Algorithm for Tracking Objects (AALTO) 5

2.1. Introduction 5

2.2. Algorithm Design 6

a. Object Identification 7

b. Tracking 8

2.3. Implementation 18

2.4. Results 22

2.5. Conclusion 28

Chapter 3: A Climatological Examination of Mesovortex Genesis 31

3.1. Introduction 31

3.2. Methodology 36

a. Event Identification 36

b. Detection of Circulations 39

c. Mesovortex Tracking and Track Filtering 41

d. Couplet Identification 46

3.3. Climatology Results 48

3.4. Storm Environments 56

a. Hypothesis and Methods 56

b. Results and Discussion 59

3.5. Conclusion 67

Chapter 4: Effects of Low-Level Stability 70

4.1. Introduction 70

4.2. Methodology 72

4.3. Results 77

4.4. Conclusion 101

Chapter 5: Concluding Remarks 106

References 111

List of Figures

Figure 2.1: AALTO Default Search Radii Page 11

Figure 2.2: AALTO Default Search Area Angle Page 12

Figure 2.3: AALTO Default Minimum Search Area Angle Page 13

Figure 2.4: Example Search Area Configurations Page 15

Figure 2.5: AALTO Flowchart Page 19

Figure 2.6: AALTO Candidate Track Example Page 22

Figure 2.7: Diagram of Thunderstorm Tracks Page 26

Figure 2.8: Diagram of Circulation Tracks Page 27

Figure 3.1: Diagram of Baroclinic Mechanisms Page 33

Figure 3.2: Diagram of the Barotropic Mechanism Page 34

Figure 3.3: Minimum Search Area Angle Page 43

Figure 3.4: Search Radii Page 44

Figure 3.5: Search Area Angle Page 45

Figure 3.6: Couplet Orientation in Upward and Downward Tilting Page 47

Figure 3.7: Example Mesovortex Couplet Page 48

Figure 3.8: Diagram of Climatology Tracks Page 50

Figure 3.9: Selected Mesovortex Tracks from 24 March 2009 Event Page 51

Figure 3.10: Mesovortex Tracks Rearward of Convective Region Page 53

Figure 3.11: Peak Mesocyclone Strength Index Distribution Page 54

Figure 3.12: Mesovortex Longevity Distribution Page 55

Figure 3.13: Mesovortex Low-Level Shear Distribution Page 56

Figure 3.14: Event with Numerous Cyclonic Mesovortices Page 58

Figure 3.15: 0-500 m Shear and Mesovortex Correlation Page 63

Figure 3.16: 0-1 km Shear and Mesovortex Correlation Page 64

Figure 3.17: Static Stability and 0-500 m Shear Correlation Page 66

Figure 4.1: Cooling Rate Determined by Theta Perturbations Page 75

Figure 4.2: Example of KH Billows Page 79

Figure 4.3: Mesovortex Genesis through Downward Tilting Page 81

Figure 4.4: Lofting of Cold Parcels Page 84

Figure 4.5: Stretching of Downward Tilted Vorticity Page 85

Figure 4.6: Mesovortex Couplet Pairs Page 86

Figure 4.7: Vortex Lines in Mesovortex Couplet Pairs Page 87

Figure 4.8: Low-Level Vorticity Tendency Page 89

Figure 4.9: Instantaneous Tilting of Horizontal Vorticity Page 92

Figure 4.10: Peak Vertical Vorticity at Low Levels Page 93

Figure 4.11: Low-Level Vorticity in 100 m Simulations Page 95

Figure 4.12: Mid-Level Vorticity and Horizontal Grid Spacing Page 97

Figure 4.13: Theta Time Series in 100 m and 500 m Simulations Page 99

List of Tables

Table 3.1: List of Storm Environment Parameters Page 61

Table 3.2: List of Storm Environment Parameters (cont'd) Page 62

Table 3.3: Correlation between Environmental Parameters Page 65

Table 3.4: Correlation between Low-Level Shear and Mesovortices Page 67

Table 4.1: Heat Sink Parameters Page 76

Table 4.2: List of Simulations and Parameters Page 77

List of Equations

Equation 4.1: Heat Sink Theta Tendency Equation Page 74

Chapter 1: Introduction

Many recent studies have linked the strongest and most damaging winds in quasi-linear convective systems (QLCSs) to small low-level embedded circulations that develop on or near the leading edge of the cold outflow from the thunderstorms (Przybylinski et al. 2000; Schmocker et al. 2000; Wakimoto et al. 2006; Wheatley et al. 2006), and have correlated the low-level mesovortices with swaths of enhanced surface winds and damage on par with some tornadoes. Mesovortices are storm-scale circulations, typically with a diameter of a few kilometers, which differ from mesocyclones in that they originate at low levels and are not necessarily spatially correlated with updrafts. Despite the significance of these mesovortices, they are poorly understood and forecasted compared to the low-level mesocyclones that develop in supercell thunderstorms (e.g., Atkins et al. 2004; Wheatley et al. 2006; Lese and Martinaitis 2010). As a result, they present a significant challenge in warning decisions made by forecasters (Lese 2006). Although many mechanisms have been proposed to explain the genesis of mesovortices (e.g., Trapp and Weisman 2003; Wheatley and Trapp 2008, Atkins and St. Laurent 2009), it remains unclear which of these mechanisms are most important in explaining the formation of these circulations, and as a result it is not yet entirely clear what atmospheric conditions are supportive of the development of low-level rotation in QLCSs.

Several processes have been proposed to explain the development of low-level mesovortices and can fundamentally be divided into baroclinic processes that generate horizontal vorticity within buoyancy gradients within thunderstorm outflow (Trapp and

Weisman 2003; Wheatley and Trapp 2008, Atkins and St. Laurent 2009) and barotropic processes (Wheatley and Trapp 2008), or those that redistribute ambient vorticity. It is generally agreed that the baroclinic processes create horizontal vorticity that is tilted to produce vertical vorticity; however, it is unclear whether updrafts or downdrafts are responsible for this tilting, and therefore whether vertical vorticity is generated through upward or downward tilting. When crosswise horizontal vorticity is tilted vertically, the result is a mesovortex couplet, consisting of a cyclonic and an anticyclonic circulation. The barotropic process involves the upward tilting of ambient horizontal vorticity, associated with strong low-level vertical wind shear, and the release of shearing instability to generate mesovortices. Both the baroclinic and barotropic mechanisms are likely associated with mesovortex genesis, depending on whether the storm characteristics support the baroclinic mechanism and if the storm environment containis sufficiently strong low-level vertical wind shear to support the barotropic mechanism. The overarching goal of this work is to provide insight as to which of the aforementioned processes are most frequently responsible for mesovortex genesis and the storm environments and configurations that are most conducive to the development of low-level mesovortices. To satisfy this objective, both empirical and numerical modeling approaches are adopted. Chapter 3 presents an examination of many severe wind cases from 2009 and 2010 to try to determine the processes responsible for the development of mesovortices. Additional work was done to try to ascertain what environmental factors and characteristics of thunderstorm outflow would be most conducive for the generation of mesovortices.

A climatology of low-level mesovortices was constructed using 44 events from 2009 and 2010 over the eastern United States. Both cyclonic and anticyclonic mesovortices were tracked and cataloged to try to determine which processes are most relevant throughout the climatology. Chapter 2 presents the Advanced Algorithm for the Tracking of Objects (AALTO), which was used to construct the mesovortex tracks. AALTO was developed because the limitations of existing tracking algorithms rendered them unsuitable for the development of the climatology. Chapter 3 describes how the climatology was constructed and examines the results with a focus on the barotropic mechanism of mesovortex genesis. Observed proximity soundings to mesovortex events were used to identify relationships between low-level storm environments and the ability of the barotropic mechanism to generate mesovortices. Additionally, the tracks were examined for evidence of the baroclinic mechanism and whether upward or downward tilting of horizontal vorticity is responsible for the generation of mesovortices.

Chapter 4 focuses on a baroclinic mechanism in which crosswise horizontal vorticity within thunderstorm outflow is tilted upward (Atkins and St. Laurent 2009), similar to one hypothesis to explain tornadogenesis (Straka et al. 2007; Markowski et al. 2008). It has been proposed that very cold supercell outflows generate horizontal vorticity efficiently while resisting tilting, whereas weak outflows do not generate large quantities of vorticity but do permit tilting, suggesting that an intermediate outflow strength is most favorable for tornadogenesis (Markowski et al. 2002; Markowski et al. 2003; Grzych et al. 2007; Markowski et al. 2010). A primary hypothesis of this research is that the so-called Goldilocks problem of tornadogenesis can be extended to the

analogous baroclinic mechanism that has been proposed to explain the genesis of low-level mesovortices. Chapter 4 presents the results of a series of numerical simulations of a highly idealized thunderstorm outflow and updraft to evaluate the role of cold pool stability in the generation of mesovortices.

Chapter 2: The Advanced Algorithm for Tracking Objects (AALTO)

2.1. Introduction

This chapter presents an algorithm for tracking objects such as thunderstorms or mesocyclones, which was used to construct the mesovortex climatology described in chapter 3. Automated tracking of meteorological phenomena such as thunderstorms and mesocyclones is useful in many applications such as the development of climatologies and the nowcasting of severe weather. While existing algorithms designed to detect thunderstorms (e.g., Dixon and Wiener 1993; Johnson et al. 1998), mesocyclones (Stumpf et al. 1998), and tornado vortex signatures (Mitchell et al. 1998) in radar data include a tracking component, improvements such as better initial estimates of storm motion and constraining track direction have been suggested (Johnson et al., 1998). Furthermore, the current operational WSR-88D severe weather algorithms used to identify and track thunderstorms (Johnson et al. 1998), mesocyclones (Stumpf et al. 1998), and tornadoes (Mitchell et al. 1998) generally are designed to operate within the range of a single radar, thereby limiting the ability to track objects through a larger domain. This article presents a new algorithm for tracking objects within weather radar data that have been detected by other algorithms. The Advanced Algorithm for the Tracking of Objects (AALTO) tracks objects across the domains of multiple, possibly overlapping, radars and adopts a number of strategies designed to improve the quality of tracking compared to existing methods. These strategies have been developed according to 1) the best practices of existing tracking algorithms and 2) the techniques that human meteorologists apply in manually tracking objects.

2.2. Algorithm Design

This section contains a literature review of existing tracking algorithms and a discussion of human-based tracking to explain how they influenced the development of AALTO. AALTO was developed incorporating the best practices from tracking algorithms such as the Storm Cell Identification and Tracking (SCIT; Johnson et al. 1998), the National Severe Storms Laboratory (NSSL) Mesocyclone Detection Algorithm (MDA; Stumpf et al. 1998), Thunderstorm Identification, Tracking, Analysis, and Nowcasting (TITAN; Dixon and Wiener 1993), and Thunderstorm Observation by Radar (ThOR; Barjenbruch and Houston 2006; Barjenbruch 2008; Lahowetz et al. 2010). Each of these algorithms adopt different approaches to forecasting object motion, searching for new objects, and identifying the best object to use in continuing a track. A review of the best practices of these algorithms and methods to avoid their limitations formed much of the basis for the techniques implemented in AALTO. The use of assumptions applied by human meteorologists in tracking is justified because the verification of tracking algorithms is typically done against a dataset of "truth" tracks created by meteorologists (Lakshmanan and Smith 2010). Human-based tracking is generally better than automated tracking; however, the latter is necessary in practice to process large data sets and when real-time tracking is necessary. If human-based tracks the "truth," then the practices that are used by humans to manually create these tracks should guide the development of an algorithm that is based on the best tracking practices. As applied to AALTO, this involves looking at both prior and future times to establish continuity in the motion of an

object and identify the best track, a practice that is not widely employed, especially for nowcasting algorithms.

a. Object Identification

SCIT and MDA detect and track objects within reflectivity and velocity data from a single radar, not incorporating data from nearby radars that may provide overlapping coverage. This approach does not make the best use of data in areas with numerous radars such as multiple WSR-88Ds, Terminal Doppler Weather Radars (TDWRs), and perhaps other radars such as the UMass Collaborative Adaptive Sensing of the Atmosphere (CASA; Junyent et al. 2010) radars. The single-radar limitations of SCIT and MDA could be avoided by first creating a mosaic of the product being analyzed, such as radar reflectivity (the proportion of energy backscattered by targets such as hydrometeors), or radial velocity (the component of the mean motion of the targets towards or away from the radar). However, velocity should not be mosaicked because it is relative to the radar location. More importantly, the identification of objects in mosaicked reflectivity or radial velocity data would require new multi-radar algorithms likely based on local maxima or minima (Lakshmanan et al. 2009).

AALTO adopts an alternate approach to avoid the single-radar limitation: instead of merging the data used to identify objects, the objects are identified independently by individual radars and then synthesized into a single composite. AALTO does not require the development of new multi-radar algorithms; AALTO can track objects identified by existing single-radar algorithms such as those used by NOAA/NWS for severe weather detection based on WSR-88D data. There are a number of challenges to such an approach

including overlapping areas of radar coverage resulting in multiple detections of the same object and the lack of synchronization in radar scan times, resulting in portions of the domain being updated at different times than other regions. The approach used in AALTO to resolve these challenges will be discussed below.

b. Tracking

MDA tracking is very similar to the approach employed by the SCIT algorithm, which extrapolates the motion of an object, based either on prior motion or a first guess for new objects, and searches in progressively larger radii around the forecast position of the object to create or continue a track. The first guess of object motion for a new track depends either on a forecast storm motion that is based on upper-air data, or the mean motion of all existing tracks within the domain. Implicitly, this assumes that the mean motion of tracks should be similar throughout the domain, and thus an average of existing tracks should be representative enough to suffice as a first guess for new tracks. This is acknowledged as a limitation of SCIT by Johnson et al. (1998), and could decrease the accuracy of tracking if the assumption is violated. This limitation will be particularly severe for domains covered by multiple radars. An alternative to the approaches of SCIT and MDA is implemented in the ThOR algorithm (Barjenbruch and Houston 2006; Barjenbruch 2008; Lahowetz et al. 2010), which derives an initial motion estimate from archived North American Regional Reanalysis (NARR; Mesinger et al. 2006) wind fields near an object. AALTO adopts a similar approach by searching storm motion estimates near the time and position of an object to produce the best initial estimate of storm motion.

For established tracks, the existing algorithms rely on prior object motion to extrapolate the position of an object and create a forecast position. SCIT uses the previous ten forecast positions (Johnson et al. 1998) while MDA maintains a history of the previous 30 minutes (Stumpf et al. 1998). ThOR uses NARR motion estimates for the first 10 minutes of a track, weights the NARR motion and observed motion between 10 and 30 minutes, and uses only the observed motion beyond 30 minutes (N. Lock, University of Nebraska-Lincoln, 2012, personal communication). AALTO defaults to using the motion history over the previous 30 minutes of the track. If the track is younger than 30 minutes, a combination of the initial motion estimate and the prior motion of the track is used. If the length of the time interval used to determine previous object motion is too short, then object tracks are likely to be overly influenced by erroneous variations in object velocity, referred to as jitter. This jitter is a consequence of the inability to exactly determine the position of the object due to the radar beam width and height, the noise inherent to radar data sets, and the difficulty in an algorithm assigning a point to an object with area and mass. These issues tend to be exacerbated when multiple radars are involved. However, if the history interval is too large, it will restrict the ability of the algorithm to detect actual changes in the bearing of the object.

To continue an object track forward in time, algorithms such as MDA and SCIT search for the closest object within a specified radius of the forecast position of the track. ThOR adopts a variable search radius that depends on the speed of the object being tracked, decreasing the size of the search radius for faster objects (Barjenbruch 2008). The ThOR approach assumes that slower-moving objects are more likely to deviate

significantly from their track than faster-moving objects (Barjenbruch 2008). ThOR uses this method because the motion of fast-moving storms is likely primarily determined by strong upper-level winds that are reasonably homogeneous over small distances. Other factors are more likely to impact the motion of slower features significantly, suggesting that their tracks may experience greater directional deviation from the prior track. Taken to the extreme, pulse thunderstorms in an environment with very weak upper-level winds may drift in almost any direction.

In AALTO, as in ThOR, the search radius is dynamic and related to the speed of the storm. The relationship between search radius and object motion (Figure 2.1) has been derived empirically based on tests conducted using storms identified by an algorithm that clusters regions of strong reflectivity(w2segmotion; Lakshmanan et al. 2006, 2007, 2009) and optimized to produce longer tracks, following the philosophy of Lakshmanan and Smith (2010). The distribution of search radii as a function of object speed is justified as follows. If an object is moving slowly, it is not physically reasonable to associate a distant object with the track, which is why the search radius is relatively small, while still allowing for jitter. As the speed of the object increases, so does the search radius, to account for the greater distance that an object could travel. For object motions greater than ~30 km hr^{-1}, the search radius decreases with increasing object motion. This is included to account for the relative contributions of translation and propagation to the object motion. Translation is the transport of an object, such as by the background wind field in the atmosphere. Propagation, such as caused by a thunderstorm growing preferentially on one of its flanks, would cause the motion to deviate from the

translation of the object. In AALTO it is assumed that propagation is smaller for objects that are moving particularly rapidly, with the motion governed by strong background flow, thus not requiring such a large search radius.

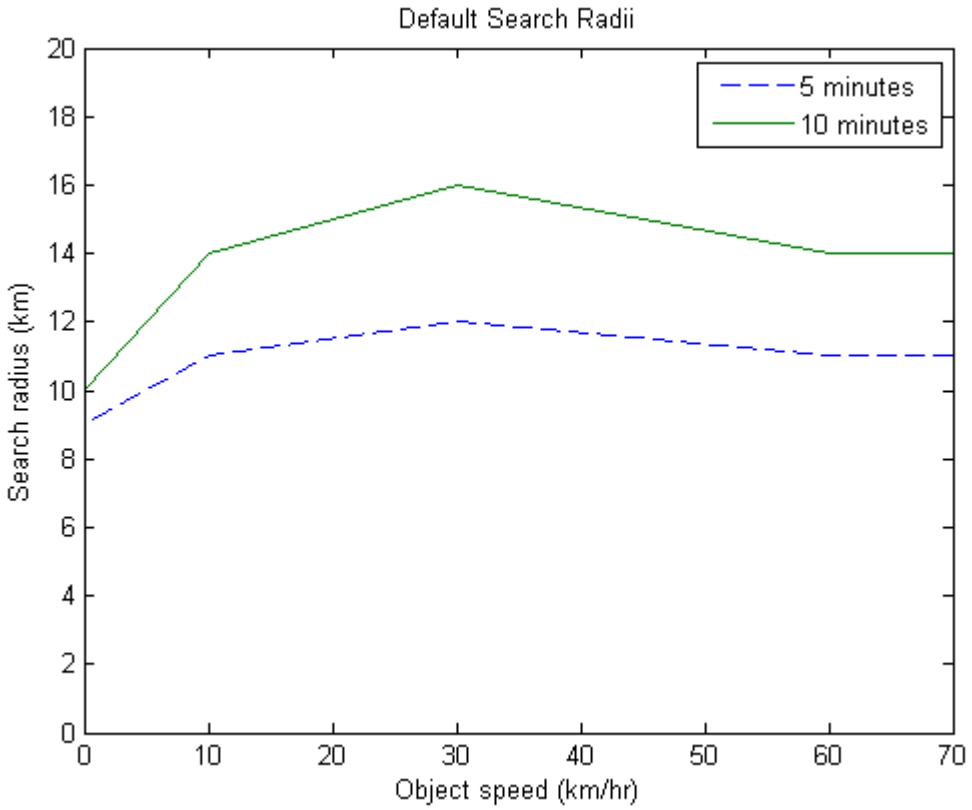

Figure 2.1: The relationship between object speed and the search radius for tracks of ages 5 and 10 minutes as solid and dashed lines, respectively.

If new objects for track continuation are sought within a full circle around the forecast position, increasing the search radius allows for more opportunity to jump to a neighboring track, especially when the correct choice would be to terminate the track. Johnson et al. (1998) noted similar issues with SCIT and recommended an approach of "directional thresholding" that would restrict the change in bearing of a track from one time to the next. AALTO implements a directional threshold to restrict the search area to

be smaller than a full circle around the forecast position. The directional threshold is dynamic and depends on 1) the amount of time elapsed since the last update to the track and 2) object speed.

For a track that has been recently updated, jitter, which is assumed to be independent of the time since the last update of the track and randomly distributed about the forecast position, is large compared with the actual object displacement. Therefore, it is necessary to search over a wide angle around the forecast position of the object. As the actual motion of the object becomes more significant compared to jitter, the search area is narrowed, as shown in the default settings for AALTO in Figure 2.2.

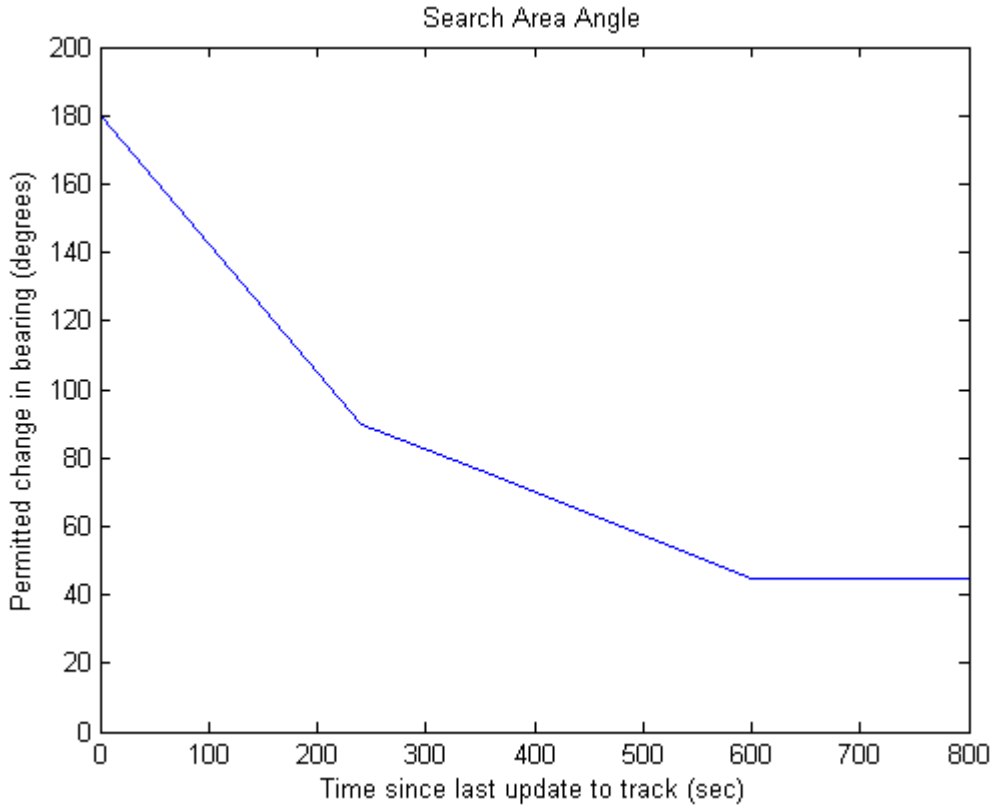

Figure 2.2: The permitted change in bearing of a track as a function of the time since a track was last updated.

AALTO also assumes the effects of propagation on the bearing of an object are related to speed of an object. Consider an object that propagates perpendicular to the direction of a track at a given speed. If the translation speed of an object is small, the effect of propagation is relatively large, necessitating a large search angle. If the translation speed is large, the effects of propagation are less significant relative to the displacement of the object, requiring a smaller search angle. The default settings for AALTO are shown in Figure 2.3.

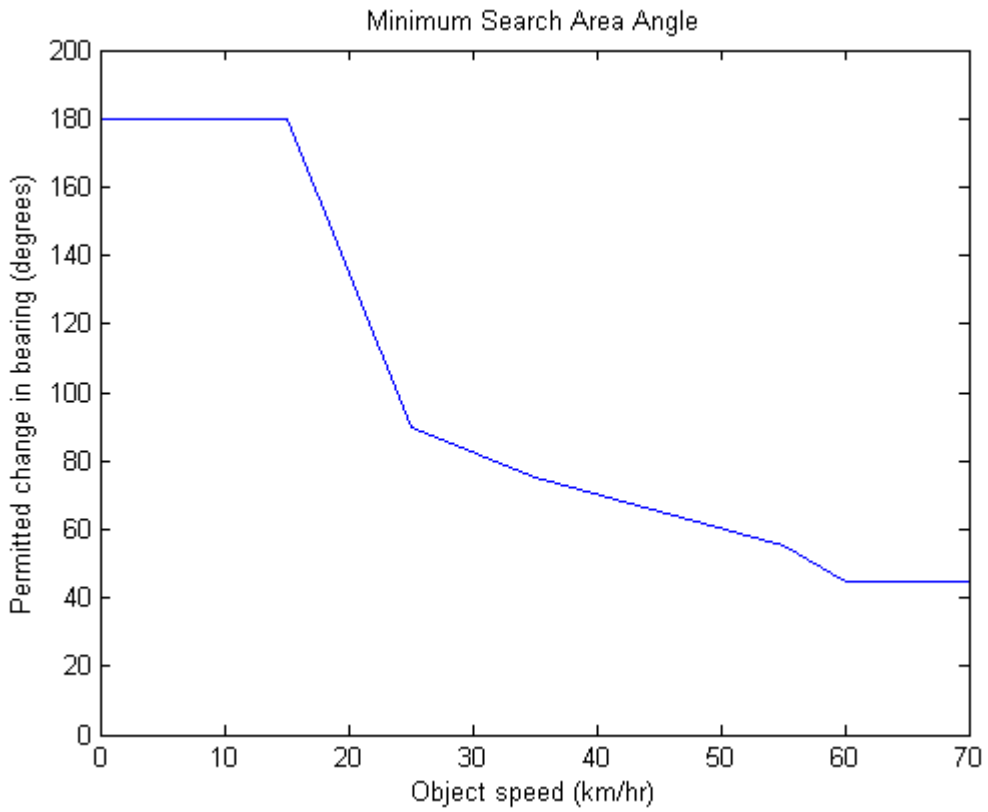

Figure 2.3: The permitted change in bearing of a track as a function of object speed.

The actual search angle is governed by choosing the larger of the angles from the previously defined criteria. It should be noted that the effects of propagation were used to partly justify both a dynamic search radius and a dynamic search angle. These are

somewhat independent because the dynamic search radius accounts for propagation that causes an object to move forward faster or slower while the search angle deals with track-perpendicular motion. Furthermore, because AALTO is designed to be versatile in tracking many types of objects, more flexibility is provided to users in determining the configuration of the search area. The combination of the dynamic search radius and dynamic search angle results in a total search area with a variety of configurations (Figure 2.4).

One unique aspect of ThOR is that it not only considers track history, but also the "future" of a track, in determining track continuity. This is fundamentally different from approaches used in SCIT, MDA, and many other algorithms that merely estimate the next position along a track using a weighted average of motion along previous track segments. This is because such algorithms operate by identifying objects within a volume scan in real time and then associating them with existing tracks. ThOR operates on archived data and considers all possible "future" tracks for a particular object by looking ahead until the end of an event The object track is determined by minimizing an error function. We denote this as a "track-at-once" approach to building tracks. This differs from the traditional approach, necessary for real-time algorithms, in which tracks are built from one volume scan to the next: a "time-at-once" approach. A ThOR-like approach of minimizing error globally is also employed by the TITAN (Dixon and Wiener 1993) system. However, TITAN does this in a time-at-once approach, rather than a track-at-once approach as ThOR does, by considering all possible combinations of tracks from one time to the next, and minimizing a cost function through the entirety of the domain.

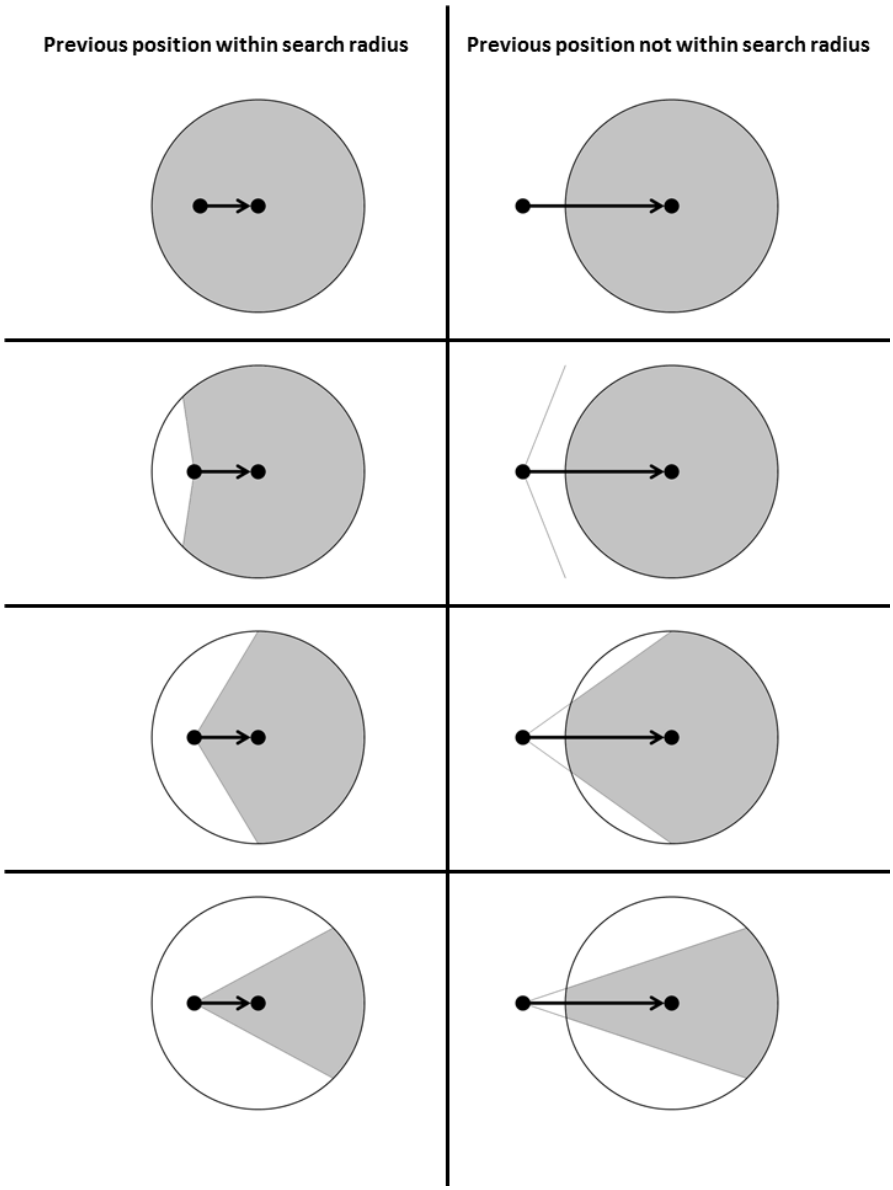

Figure 2.4: The possible configurations for search areas, depending on user-specified parameters. The gray area shows the actual search area. The left column shows a situation in which the initial position is within the search area. The right column shows a situation in which the initial position is outside the search area. The top row shows a situation in which there is no restriction on search angle. Progressively smaller search angles are shown towards the bottom of the figure. The search angle is narrowed for faster moving objects or tracks that have been updated less recently.

The ThOR and TITAN approaches both offer benefits over the traditional approach of continuing tracks in that additional information beyond the history of a single track is used in establishing continuity. Using archived data, a human manually tracking objects would likely look at a few previous volume scans and a few future volume scans to find the next object along the path of a track. AALTO uses a ThOR-like approach to tracking objects by considering future positions of the object in addition to the past. This approach is most appropriate when operating on archived data but could be used in nowcasting to retroactively refine real-time tracks. Furthermore, use of high-resolution ensemble numerical weather prediction for nowcasting is increasing. In model output from such simulations, data are available at several lead times, so that future position information could be available for simulated objects.

Although AALTO is ThOR-like in looking ahead to future positions, it still operates from one time to the next rather than in a track-at-once approach; that is, in contrast to ThOR, an entire track is not developed before the next object at a given time is considered. Instead, only the continuation of a track to the next time (defined as a first-order branch) is developed before the next object is considered. The role of future object positions (constituting higher-order branches) is to inform the decisions made concerning the first-order branch. Specifically, as in ThOR, AALTO develops all possible candidate tracks and then traverses the tree to find the track that has the lowest mean position error, defined as the distance between the forecast position and actual position along the track. For higher-order branches, all possible positions within an interval of time, defaulting to 12 minutes, are considered, which can skip some times for which positions are available.

This allows for the creation of straighter candidate tracks, in which position errors at future times are primarily due to changes in object displacement and not due to jitter. The first-order branch that contains the selected candidate track is chosen as the continuation of the track. However, unlike in ThOR, in AALTO the influence of higher-order branches decreases with order; it is unlikely that a human meteorologist would give the same weight to a tenth-order branch as the second-order branch. AALTO implements this by exponentially decreasing the weighting of the position errors from higher-order branches. The first-order branches are given a weight of 1. Each branch thereafter is exponentially weighted less, with an e-folding time defaulting to 400 seconds. Building and searching the tree is an exponentially complex problem, potentially increasing without bound if the tree is allowed to grow unchecked. AALTO addresses this issue by truncating the tree once the weight decreases to less than a user-specified threshold, defaulting to a weight of 0.01.

In AALTO, it is assumed that "stronger" objects, such as more rapidly rotating circulations and more intense thunderstorms, are more likely to be longer-lived. There is some evidence to support this assumption for thunderstorms (MacKeen et al. 1999). As such, the time-at-once processing of object motion in AALTO is done such that "stronger" objects are considered first. As a consequence, these "stronger" objects would also have a better chance of continuing into the future. Because of this strength weighting, the full track developed for a particular object at a particular time and used to inform the choice of the first-order branch is rarely the actual path produced by AALTO once it completes the tracking of all objects and all times.

2.3. Implementation

The overall processing by AALTO is shown in the flowchart in Figure 2.5. The first step in the algorithm is to develop initial object motion estimates, which are specified from an external data source and can be gridded or irregularly spaced. This allows for versatility in how the algorithm estimates the motion of objects initially while maintaining the best practice of using spatiotemporally heterogeneous initial motion estimates. Next, AALTO ingests the objects to be tracked. AALTO permits any number of fields to be associated with each object, all of which are preserved through the algorithm and written in the output. However, a few fields are required in the input: latitude, longitude, a timestamp, and a strength parameter. For circulations, a parameter such as the shear or rotational velocity might be an appropriate strength parameter. If the objects are thunderstorms, vertically integrated liquid or maximum reflectivity could be appropriate. If the data set is comprised of data from multiple radars, an identifier for the radar and the distance from the radar are also required parameters, which are necessary for filtering collisions, as defined and explained below. Because radars are not synchronized to scan at the same time, and different volume coverage patterns require different amounts of time to complete a volume scan, objects in the database appear at irregular intervals. The objects are matched with the nearest initial motion estimate in time and space as they are ingested.

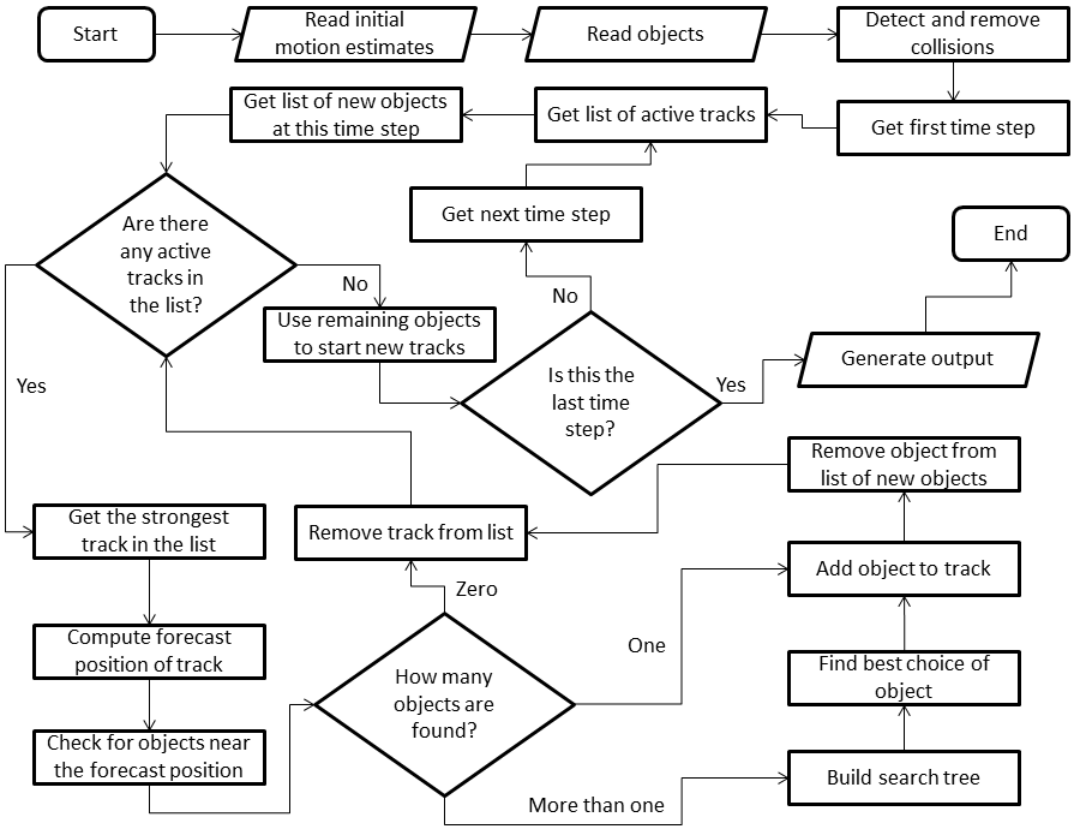

Figure 2.5: The flowchart showing the general steps in the AALTO tracking algorithm.

It is possible for multiple radars to scan the same object at precisely the same time (to the granularity of a second), which means that one object would be counted two or more times at the same time step. Multiple instances of the same object at the same time step could adversely affect the results of the tracking. While this occurs rarely, it was found in some of the data sets used to test AALTO. Such an instance is referred to as a collision, which AALTO detects and resolves once all the objects have been ingested. At any particular time step, if two objects are detected by different radars and are within a specified radius of each other, defaulting to a distance of 5 km, it is considered to be a collision. Collisions are resolved by retaining the object with the smallest distance to its

detecting radar. All objects colliding with this particular object are deleted from the data set. This step is repeated for each time step until all collisions have been resolved.

At any particular time step, all active tracks are examined, beginning with the strongest track and iterating to the weakest track, to search for possible continuations of the track. Active tracks are all tracks that have been updated within a specified amount of time, defaulting to 12 minutes (slightly longer than two typical WSR-88D volume scans). The track motion is estimated based on a combination of prior motion and the initial motion estimates provided to AALTO, and a forecast location is produced for the object being tracked, to provide the best guess of the position of the object. Forecast motion is estimated by calculating the motion over a prior length of the track. Using this motion estimate, a forecast position is produced. The region around the forecast position is searched for objects that are candidates to continue the track. This region is restricted based on the proximity to the forecast position and the change in bearing between the estimated motion and the actual motion from the last track position to the candidate track. To account for the possibility that an object identification algorithm misses an object at a given time or calculates an object centroid that is removed from the correct track, AALTO considers all possible object positions within 12 minutes from the time of the latest position on the candidate track.

If more than one candidate object are found within the search area, additional processing is done to determine which object is the best continuation of the track. Each of the tracks to candidate objects is treated as a first-order branch. From these branches, the procedure is repeated recursively, adding higher-order branches for the duration the track

would remain active. Tracks are added until the exponentially decaying branch weight passes below a threshold value. The exponentially decaying branch weights are used to calculate the weighted average error, as defined by the distance between the forecast position and the position of each object, for each candidate path. The first-order branch associated with the candidate path with the minimum weighted error is selected to continue the track. An illustration of the concept of a search tree is shown in Figure 2.6. Only the next position is retained, not the entire track, because this is a time-at-once approach rather than a track-at-once approach.

Any objects that have not been added to existing tracks at the end of a time step are used as the first position in new tracks. The process is repeated for each time step until the end of available data.

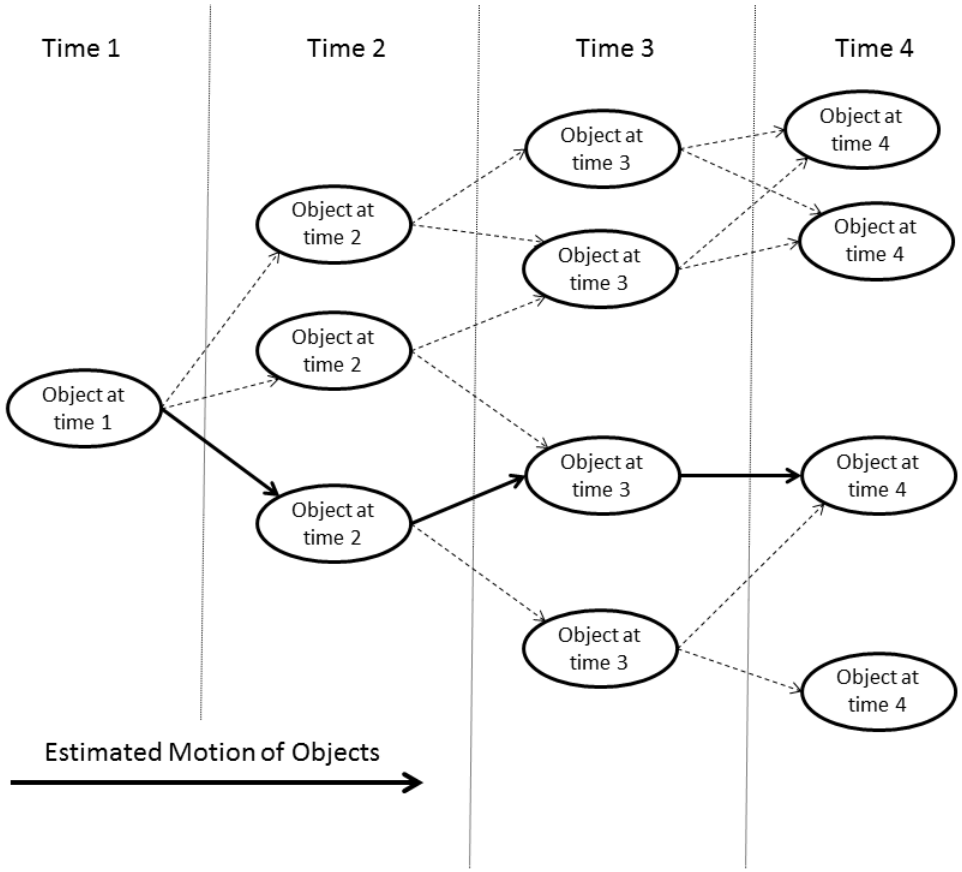

Figure 2.6: The approach of building trees to find the best path. Candidate tracks are dashed lines and the actual best track is the solid line. Although the middle object at time 2 is closest to the forecast position for that time, based on the estimated motion, the bottom object is chosen to continue the track because it reduces the forecast error at later times and minimizes the overall error.

2.4. Results

In this section, results of running AALTO on two different types of data, thunderstorms and storm-scale circulations, will be presented. Each event will be analyzed individually along with an overall summary of the performance of the algorithm. As noted by Lakshmanan and Smith (2010), construction of a truth data set through human tracking is both difficult and subjective, especially when there are large numbers of objects. Rather than attempting to do explicit verification, Lakshmanan and Smith (2010) offer suggestions for how to objectively evaluate the performance of an

algorithm. Specifically, algorithms that produce longer tracks tend to be superior to those identifying many short tracks. They also recommend additionally examining the continuity of a parameter, such as vertically integrated liquid for thunderstorms, to evaluate whether the tracks are realistic. Parameter continuity was not used for this work since objects detected by multiple radars are likely to have large variations of such parameters from one position to the next owing to differences in resolution due to the varying distances of radars from a particular object. However, when objects such as thunderstorms or circulations are directed by larger-scale flow such as the mean wind over a deep layer, tracks should tend to be generally parallel within a region. Following Lakshmanan et al (2010), longer tracks that tended to be parallel were indicative of good performance by the algorithm. Some variability in position from one time to the next is to be expected due to jitter, but at a broader scale, the tracks should be consistent if the algorithm is performing well.

Four thunderstorm data sets and two storm-scale circulation data sets were used to demonstrate the performance of AALTO. The thunderstorm data sets were created by merging together reflectivity from multiple radars using the w2merger algorithm (Lakshmanan et al. 2006), creating a lat-lon-height grid, and calculating composite reflectivity (strongest reflectivity at any height at every point). The w2segmotion algorithm (Lakshmanan et al. 2009) was used to identify storms from composite reflectivity. Storm-scale circulations are treated separately because a different set of parameters were used in tracking and the data set includes detections from multiple radars. Circulations were identified using the NSSL MDA (Stumpf et al. 1998) with the

default settings. Because AALTO is tuned by default to track thunderstorms, settings were adjusted to account for the smaller scale of the circulations. Specifically, search radii and the permitted change in bearing were decreased from the default settings (which are shown in Figs. 2.1-2.3) to limit contamination from jitter. Furthermore, because the storm-scale circulations are smaller than the actual thunderstorms, there are more objects in close proximity. Using the default settings allowed the search trees to grow very large, requiring large amounts of computing resources, especially computation time. This would be undesirable in a nowcasting environment when rapid updates are necessary for forecasting decisions. Furthermore, because high-order branches are unlikely to cause a different first-order branch to be chosen, decreasing the size of search trees is not likely to substantially diminish the quality of the tracking. For these reasons, the weighting of future positions was more rapidly diminished for circulations than in the default AALTO settings, decreasing the size of search trees and the computational resources used.

Thunderstorm events were chosen of varying durations and numbers of storms. This was done primarily for the purpose of benchmarking the performance of AALTO and to assess the scalability of the algorithm for large data sets. For these events, objects are coherent regions of strong reflectivity (defined as reflectivity clusters) and serve as a proxy for thunderstorms. For many of these events, the full domain is not shown, instead showing a smaller region to show individual tracks more clearly. The 1-6 January 2005 event, shown in Figure 2.7a, covers multiple thunderstorm events, with many sets of generally parallel tracks moving east or northeast. A total of 7,034 reflectivity cluster tracks are observed for this event, with the longest tracks persisting slightly longer than

five hours. The second thunderstorm event is 14-23 April 2005, illustrated in Figure 2.7b, producing a total of 8,609 tracks. As with the previous event, this encompasses multiple thunderstorm events, which is why some tracks are directed to the northeast, while others are roughly parallel to each other but pointing nearly north. The longest tracks are slightly longer than six hours during this event. The third storm event is 1-2 May 2005 over the southern Great Plains, shown in Figure 2.7c. Because the storms during this event were small and weak, reflectivity cluster tracks were generally shorter, but again exhibit roughly parallel motions and appear generally coherent. The longest tracks last nearly two and a half hours, with a total of 327 tracks. The final thunderstorm event is 18-21 October 2005, with tracks shown in Figure 2.7d. The tracks are generally parallel and long-lived throughout much of the domain. There are a total of 2,738 tracks, the longest of which persist nearly nine hours.

The first event for which circulations are tracked is 4-5 June 2009 in west Texas, with results shown in Figure 2.8a. In total, 386 tracks are identified, the longest of which are approximately four hours in duration. The other event in which circulations are tracked is 8 March 2009, shown in Figure 2.8b. In total, 1,546 tracks are identified, with the longest tracks approaching two hours in duration. Faster-moving objects in this event than in the 4-5 June 2009 event likely resulted in longer, straighter tracks. This event also illustrates the need for more than one first guess of object motion for a large domain; in the southern portion of this figure, circulations generally tracked eastward, as opposed to northeasterly in the northern part of the domain. Using a single estimate of motion throughout the entire domain would likely have reduced the quality of the tracking. In

both events, multiple radars were used for identifying portions of the longest tracks. The effects of jitter are more pronounced in the circulation tracks than in the reflectivity clusters, resulting in a larger deviation in direction from the prior motion along the track. This occurs because circulations are detected independently by multiple radars, as opposed to the reflectivity clusters, which are created by a mosaicking algorithm that smooths out some of the effects of jitter.

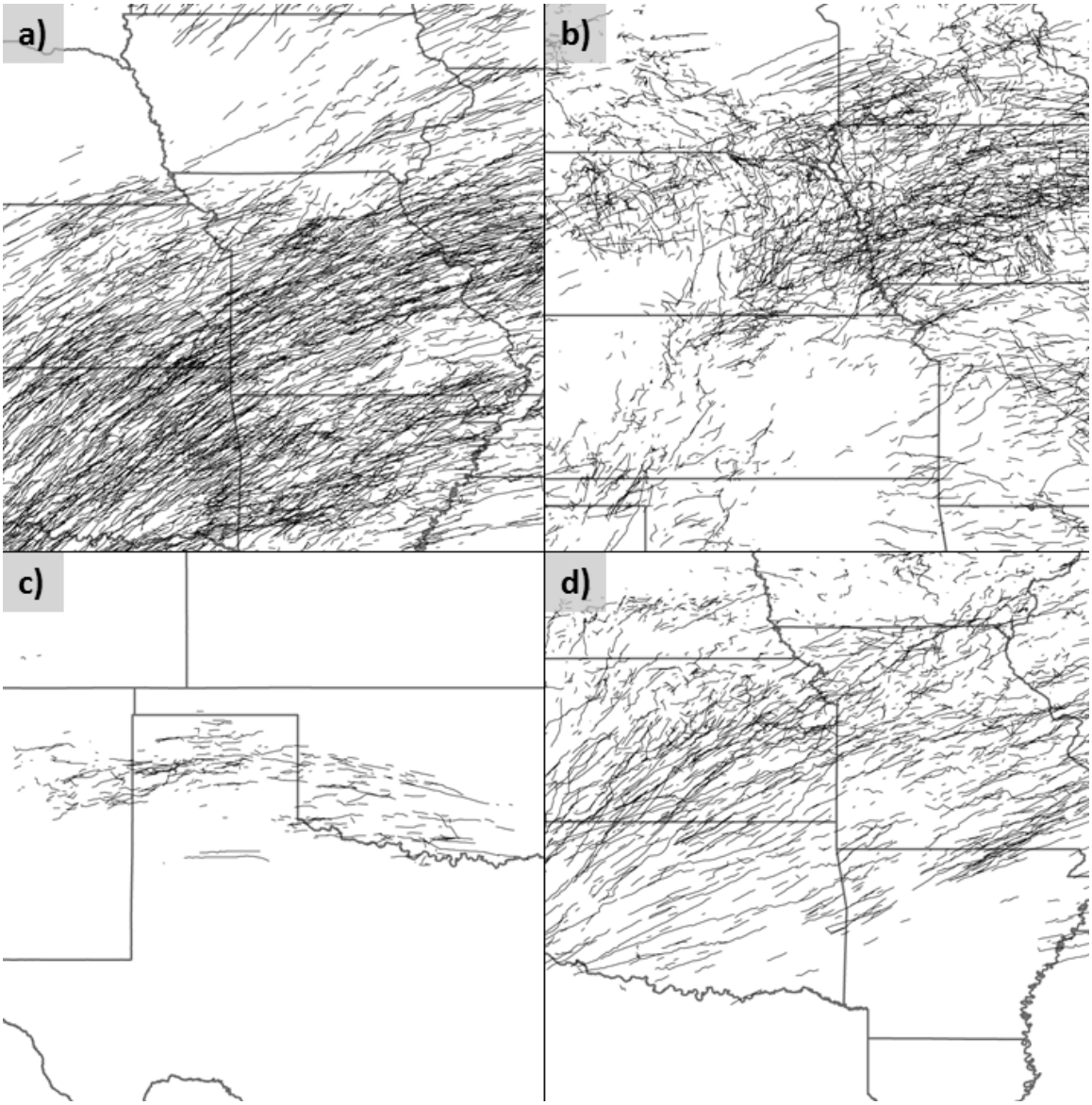

Figure 2.7: Reflectivity cluster tracks for the events a) 1-6 January 2005, b) 14-23 April 2005, c) 1-2 May 2005, d) 18-21 October 2005.

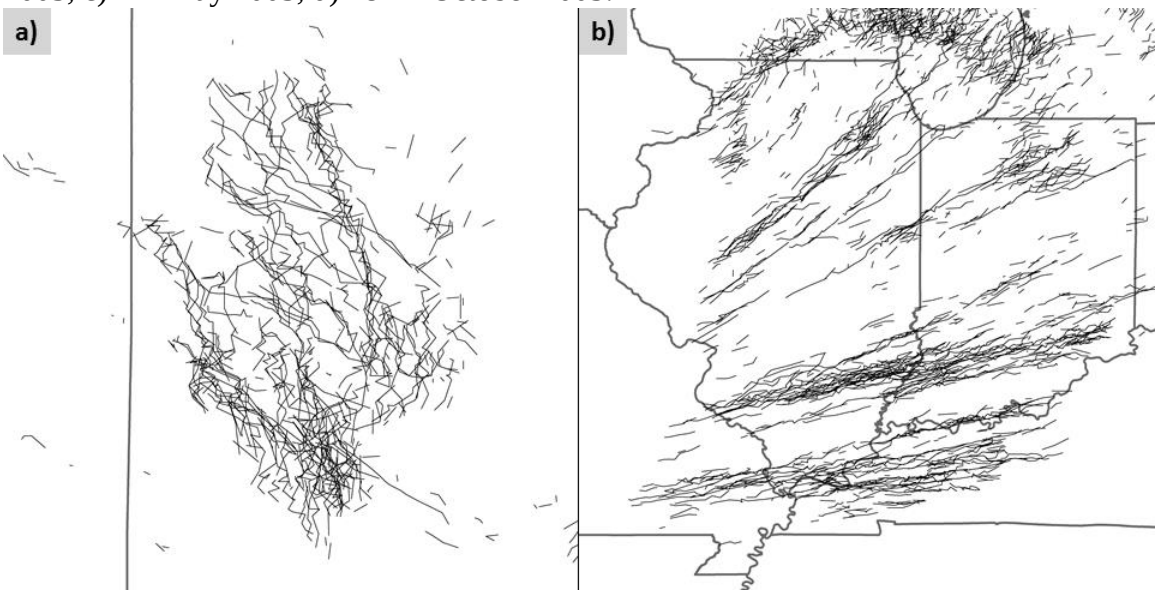

Figure 2.8: Circulation tracks for the events a) 4-5 June 2009 and b) 8 March 2009. Panel a is centered over the Texas Panhandle.

Based on qualitative analysis of these examples, tracking appeared to be improved for faster-moving objects, largely due to the smaller amount of jitter relative to the actual motion of the object. The potential for error was greatest for data sets such as circulations, which are smaller scale features than thunderstorms, and may have many objects in close proximity. Even for relatively slow-moving circulations, many long, coherent tracks were still identified by AALTO.

Very few search trees were built when reflectivity clusters were being tracked. Recall that search trees result when multiple objects reside within the search area around a forecast position. Only about 0.25% to 0.5% of the time were search trees constructed while tracking reflectivity clusters. This is because the objects are large, and rarely was more than one object found within the search area. Significantly more search trees were built for circulations, simply because the objects are closer together and frequently, more

than one choice was found near the forecast position. This resulted in search trees being constructed between 10% and 15% of the time. For both types of data, the construction of a search tree resulted in a selection of a first-order branch that did not connect to the object closest to the forecast position roughly 10% of the time. While search trees are not built particularly often, the cases in which trees are built are when two or more objects are relatively close to the forecast position, which would present the greatest degree of difficulty in tracking. So, although the building of search trees is infrequent, it should not be interpreted that building search trees does little to improve the skill of the tracking.

2.5. Conclusion

AALTO offers the versatility of tracking many different types of objects detected in weather radar data while addressing many known limitations of existing tracking algorithms. AALTO can track objects over large domains using both previously-mosaicked data sets and the output of legacy single-radar severe weather detection algorithms. Furthermore, AALTO resolves some known limitations of existing tracking algorithms by implementing a better approach to estimating the initial motion of objects than a single vector for an entire domain and by implementing a search area for track continuance that is restricted not only by range but also bearing. The approach of examining future positions to improve track continuity more closely mimics how a human would track objects, and should produce better tracks in instances where there are multiple possible objects that could be the extension of an existing track. The instance when there are multiple options to continue a track is one of the more challenging situations for an algorithm. Adding the additional information of future positions to

establish the continuity of the track should offer additional skill over merely selecting the object closest to the forecast position at the next time.

The legacy severe weather algorithms have been operational since shortly after the WSR-88D network became operational, resulting in a long period of record for which data are available. There are many research applications to developing climatologies of severe weather phenomena such as thunderstorms and storm-scale circulations. AALTO allows the existing output from the legacy algorithms to be mosaicked over a large domain rather than developing a new suite of tools. Despite the known limitations of the legacy severe weather algorithms, they have been tested in operational settings for over a decade; the benefits and limitations of the algorithms have been well-studied, allowing for better interpretation of their outputs than that of a new and relatively untested severe weather algorithm. Although the development of AALTO was primarily for the purpose of creating climatologies, the principles of the algorithm are also applicable to nowcasting settings. In such an environment, using the legacy severe weather detection algorithms is beneficial because operational forecasters are familiar with their outputs.

The design of AALTO was based on the best practices of a variety of existing tracking algorithms and the methods a human would employ in tracking objects. The design decisions incorporated good practices of existing algorithms while attempting to address known limitations of those algorithms. Furthermore, AALTO offers substantial versatility in its inputs, tracking both single-radar and multi-radar object detections of any sort, and allowing significant flexibility in how the tracking occurs including the choice of an initial motion for new tracks and many parameters to determine how objects are

added to tracks at subsequent times. These advances allow for the development of climatologies over large domains while also permitting use in a nowcasting setting.

Chapter 3: A Climatological Examination of Mesovortex Genesis

3.1. Introduction

Studies have found that mesovortices within QLCSs are frequently associated with the strongest surface straight-line winds and, therefore, the greatest potential for wind damage (e.g., Wakimoto et al. 2006; Wheatley et al. 2006). Prior to the Bow Echo and MCV Experiment (BAMEX) in 2003, it was widely believed that the strongest straight-line winds in QLCSs were found at the apices of bow echoes (Wheatley et al. 2006). BAMEX and other recent studies (e.g., Przybylinski et al. 2000; Schmocker et al. 2000; Wheatley et al. 2006) found that the most damaging winds were often correlated with the tracks of low-level mesovortices. Despite the significance of mesovortices, there is less skill in nowcasting mesovortices compared with similar phenomena such as mesocyclones because of their transient nature (e.g., Atkins et al. 2004; Wheatley et al. 2006; Lese and Martinaitis 2010), which poses significant challenge for operational forecasters (Lese 2006). The overarching goal of the research presented herein is to contribute to the ability to forecast and nowcast mesovortices and their associated hazards.

The hypotheses that have been proposed to explain the genesis of mesovortices attribute the vertical vorticity generation to either the tilting of baroclinically generated horizontal vorticity (a baroclinic process) or the redistribution of ambient horizontal vorticity (a barotropic process). The baroclinic processes require temperature gradients within the outflow of a QLCS, in which horizontal vorticity is generated and subsequently tilted vertically. Several specific baroclinic processes have been proposed

including tilting up of streamwise vorticity (Atkins and St. Laurent 2009; see their fig. 15), tilting up of crosswise vorticity shown in Figure 3.1a (Atkins and St. Laurent 2009; see their fig. 16), and tilting down of crosswise vorticity as shown in Figure 3.1b (Trapp and Weisman 2003; see their fig. 23). Wheatley and Trapp (2008) propose a barotropic mechanism in which strong horizontal shear between the ambient low-level flow and the outflow produces a layer of strong horizontal vorticity near the surface (Figure 3.2a) from which mesovortices are generated through the upward tilting of vorticity and the release of shearing instability (Figure 3.2b). Although these and other mechanisms have been proposed to explain the genesis of mesovortices, there is limited understanding of the environmental conditions and QLCS structure that contributes to a greater number of mesovortices and stronger circulations. The initial hypothesis was that baroclinic mechanisms are responsible for a large proportion of mesovortices and that tilting up is primarily responsible. This chapter describes a climatology of bow echo mesovortices and the environmental factors that appear to contribute to barotropic mechanisms for mesovortex genesis.

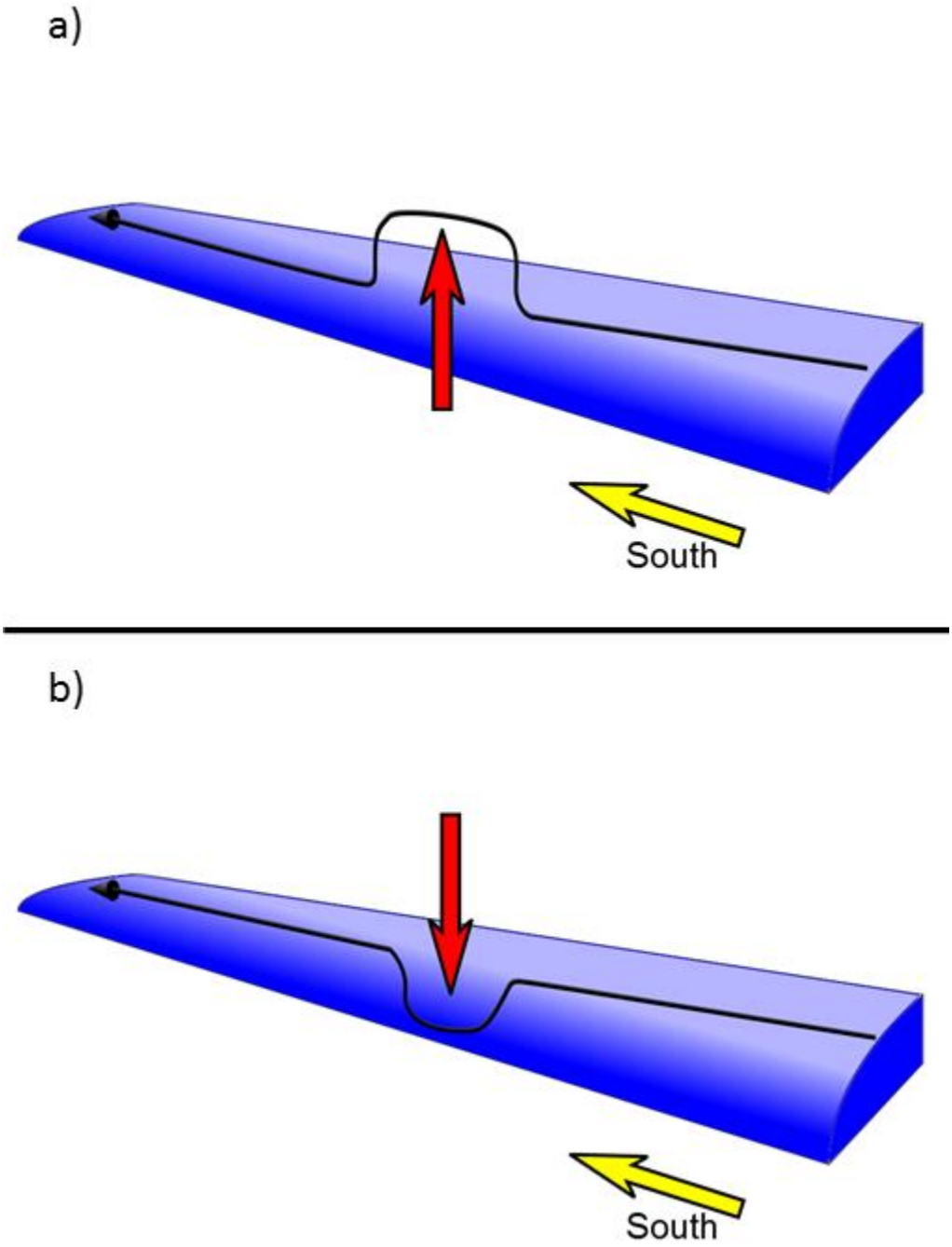

Figure 3.1: A vortex line, shown by the black arrow, indicates crosswise baroclinic horizontal vorticity within the outflow (blue). The red arrow shows vertical motion within an updraft in the upper panel tilting the vortex line upward and a downdraft within the lower panel tilting the vortex line downward.

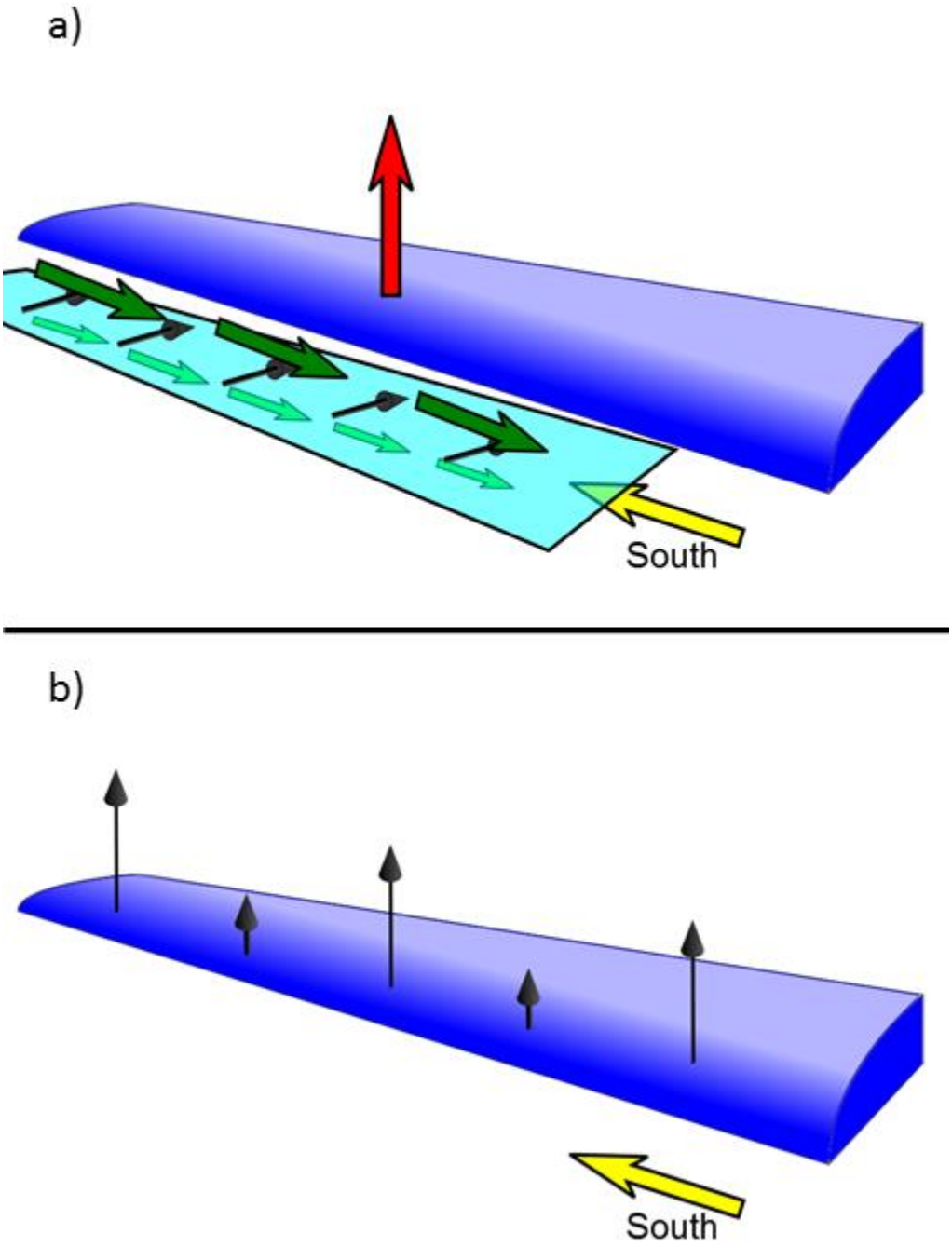

Figure 3.2: Vortex lines are shown by the black arrows and low-level winds are indicated by the green arrows at two levels. The upper panel shows a layer of horizontal vorticity ahead of the gust front, which is tilted upward. Vertical vorticity is amplified by barotropic instability, shown by the longer vortex lines in the lower panel.

The results of a climatology of bow echo mesovortices are presented in this chapter, encompassing 44 events from 2009 and 2010. The purposes of the climatology are twofold: to offer insight into which processes are responsible for the genesis of mesovortices and to sample the range of storm environments associated with mesovortices. This is accomplished by automated detection and tracking of storm-scale vortices, identification of mesovortex tracks, and analysis of proximity soundings.

Both the baroclinic and barotropic mechanisms discussed above require that the tilting align horizontal vorticity vertically and concentrate it through stretching by thunderstorm updrafts. Methods of mesovortex genesis that involve tilting of baroclinically-generated crosswise vorticity predict the formation of mesovortex couplets consisting of a cyclonic and an anticyclonic circulation. Trapp and Weisman (2003) predicted the absence of low-level anticyclonic mesovortices owing to the stretching of planetary and ambient synoptic-scale cyclonic vorticity. Observations of mesovortex couplets have been very limited, although two such couplets were identified by Lese and Martinaitis (2010). One primary impetus for developing this climatology was to search for the presence of mesovortex couplets over a larger data set. The barotropic mechanism for mesovortex genesis predicts periodically-spaced cyclonic mesovortices along or slightly ahead of the gust front, associated with strong horizontal shear supportive of barotropic instability that causes the growth of such mesovortices. Although the presence of shear instability predicts periodic vortices along a gust front, the mechanisms are similar to those responsible for non-supercell tornadoes, in which there is a second condition of vortex stretching: colocation of the low-level rotation with a thunderstorm

updraft (e.g., Wakimoto and Wilson 1989; Roberts and Wilson 1995). The implication is that mesovortices may not be evenly distributed along a gust front due to the unequal distribution of stretching. However, the presence of a large horizontal shear and numerous vortices would be expected if barotropic processes are responsible for mesovortex genesis. This forms the basis for attempting to ascertain vortex formation mechanisms from the results of the climatology.

3.2. Methodology

Creating this mesovortex climatology required identifying events that are likely to contain mesovortices, identifying bow echoes and quasi-linear features, tracking circulations, and associating circulations to linear and bowing storms. Events were identified using storm reports from the Storm Prediction Center database for the years of 2009 and 2010 (Section 3.2a). Radar mosaics, generated from level III base reflectivity and available at a frequency of five minute intervals, were used to identify which radar(s) were associated with each event (Section 3.2a). Circulations were identified using the National Severe Storms Laboratory (NSSL) mesocyclone detection algorithm (Stumpf et al. 1998) operating on level II radar data (Section 3.2b). Circulations were tracked and filtered (Section 3.2c) and circulation couplets were identified (Section 3.2d).

a. Event Identification

During the course of a single year, thousands of severe thunderstorm wind gusts are reported. These gusts originate from a variety of sources including microbursts, larger scale downbursts and mesovortices. Instead of processing hundreds or thousands of events, the event identification step serves the purpose of keeping the computation time

reasonable by identifying events that are very likely to contain mesovortices. It is sufficient to only select a limited number of events likely to contain mesovortices because the goal of this project is not to track every mesovortex, but rather to draw conclusions about mesovortex properties from a large data set. The event selection process may introduce biases in the properties of cyclonic and anticyclonic mesovortices. For example, if anticyclonic mesovortices are generally weaker than cyclonic mesovortices, selecting high-end events, likely associated with generally stronger mesovortices, would potentially result in increasing the percentage of anticyclonic mesovortices that are strong enough to be detected.

One criterion was to eliminate all severe wind reports west of the 105°W meridian. Primarily this is due to the sparse coverage of radars and high potential for beam blockage in the western United States. Additionally, there is a climatological reason to eliminate reports in the western U.S.: severe wind events in the western United States are frequently associated with dry microbursts and inverted-V soundings (Johns and Doswell 1992).

Analysis of damage surveys has frequently associated the greatest damage in bow echo events with embedded mesovortices (e.g., Wakimoto et al. 2006; Wheatley et al. 2006). Wakimoto et al. (2006) used dual-doppler data from an event containing mesovortices and found that adding the effect of the pressure gradient force associated with mesovortices was sufficient to explain the locations of the greatest damage. Without the influence of mesovortices, the background wind field associated with the rear inflow jet was insufficient to explain the intensity and location of the strongest winds. Derecho

climatologies have considered a threshold requiring at least three high-end wind events producing F1 damage or winds in excess of 65 knots (Johns and Hirt 1987; Bentley and Mote 1998; Coniglio and Stensrud 2004). The proposed link between high-end thunderstorm wind events and mesovortices forms the basis for the first criterion: a threshold based on high-end wind gust reports. For the purpose of identifying events, the first criterion was that storms must produce at least two reports of 65 knot or stronger winds.

Another major criterion in pruning the severe wind reports was to remove estimated wind reports. There are a variety of wind estimates in the severe reports database including estimates by trained weather spotters, based on the size of downed trees and other damage, or the results of a formal damage survey (Trapp et al. 2006). Due to the wide variety of severe wind report estimates and the potential for subjectivity and error, only measured wind reports are retained in identifying events.

The remaining wind reports were examined for geographic and temporal proximity. Thunderstorm wind gusts produced by the same thunderstorm complex were considered part of a single event even if the reports were many hours apart. However, reports that were close together spatially and temporally but associated with different thunderstorm complexes were classified as different events. After applying these methods and the above criteria, 44 events from 2009 and 2010 were identified. Events were considered to begin three hours prior to the first report of an event and to end three hours after the final report of an event, rounding to the nearest hour.

Radar composites of peak reflectivity were generated through the duration of an event. Regions where strong composite reflectivity of approximately 30 dBZ that did not appear to be within a stratiform region were outlined and classified as storms. The focus is on low-level (below 2 km above ground level) circulations. Because the center of the radar beam is above approximately 2 km above ground level beyond a range of 120 km, level II data were collected only from radars that were at most 120 km from storms. Due to the height and broadening of the radar beam at a distance of 120 km, low-level mesovortices would likely not be well-sampled beyond this range. Limiting the range serves to ensure accurate observations of circulation intensity and motion.

b. Detection of Circulations

Radar data were dealiased prior to the detection of circulations. Initial soundings from the approximate midpoint of each event were derived from Rapid Update Cycle (RUC; Benjamin et al. 2004) analyses and were used to improve the quality of the dealiasing. An input sounding was provided for each radar that was included in the event.

The NSSL Mesocyclone Detection Algorithm (MDA) (Stumpf et al. 1998) was used to identify circulations. The default parameters for the NSSL MDA in the build included in the Warning Decision Support System – Integrated Information (WDSS-II; Lakshmanan et al. 2007) were used in the processing, including using the default intensity threshold. The only exception is that the NSSL MDA only detects cyclonic circulations. This limitation was worked around by running the NSSL MDA twice – once to detect cyclonic circulations in the northern hemisphere and once for the southern

hemisphere, to detect anticyclonic circulations – generating two sets of storm-scale circulations.

Although the MDA is typically used for identifying mesocyclones, Stumpf et al. (1998) note that the NSSL MDA was designed for the purpose of detecting all types of storm-scale circulations. The approach of using the NSSL MDA to track non-mesocyclone vortices is not new; Wheatley et al. (2006) used the NSSL MDA to identify bow echo mesovortices. The default NSSL MDA thresholds are set to detect most significant vortices while minimizing the false alarm rate (Jones et al. 2004). Filtering of output based on the vortex strength rank has been adopted in previous applications of the MDA (e.g., Trapp et al. 2005); however, the default parameters generally appear adequate for identifying most potentially significant vortices. Filtering based on vortex depth has also been applied (e.g., Oppermann and Houston 2012); however, there is no definite depth criterion that distinguishes bow echo mesovortices from mesocyclones, and mesovortices deeper than 3 km have been observed (Dunn and Best 2010). Furthermore, deeper mesovortices are often associated with increased threats of tornadoes and damaging winds (Atkins et al. 2004, Atkins et al. 2005), and so these deeper vortices are of greater interest for inclusion in this analysis because of their greater impacts. For this reason, filtering of circulations based solely on depth was not implemented here, but was done at a later step.

Stumpf et al. (1998) describe the detection of vortices in detail, a process that will be summarized here. Segments of one-dimensional (1D) shear are identified by comparing velocities across adjacent radar radials for cyclonic shear. After 1D shear

segments are identified within a sweep, two-dimensional (2D) vortex signatures are identified applying rules based on the size and shape of the vortices to eliminate line shear and very broad circulations while combining together neighboring 1D shear segments. The 2D features are then vertically correlated to identify three-dimensional (3D) vortices. Although earlier MDA versions applied circulation strength thresholds early in the vortex identification process, the NSSL MDA does not perform strength thresholding until after 3D circulations have been identified, resulting in a more robust vortex identification algorithm (Stumpf et al. 1998).

c. Mesovortex Tracking and Track Filtering

Although the NSSL MDA does contain a tracking algorithm, MDA-identified tracks close to radars, where numerous circulations were detected within close proximity, were found to have erratic motions. Moreover, the MDA tracking is limited to the domain of a single radar; however, all of the events used for this work span many radars, which would result in splitting tracks between radar domains and possibly counting tracks twice when scanned by multiple radars. The Advanced Algorithm for the Tracking of Objects (AALTO) was used to track the circulations detected by the MDA. AALTO addresses the limitations of MDA tracking and incorporates many of the best practices of human tracking, such as establishing track continuity by examining possible future track positions, and of existing algorithms, such as the directional thresholding recommended by Johnson et al. (1998). The default parameters for AALTO are intended to track larger-scale objects such as entire thunderstorms, and were not suitable to track smaller-scale features such as circulations. The search areas for mesovortices were narrowed, both in

terms of search radius and search angle, from the defaults, shown in Figures 3.3-3.5. This was done because the default parameters frequently connected existing tracks to neighboring tracks when, in reality, the circulation being tracked ceased to exist. Additionally, the search trees for future positions were further limited from the default by e-folding the weighting of future positions at 300 seconds and truncating at a weight of 0.05. Cyclonic and anticyclonic circulations were tracked independently, requiring two runs of AALTO for each event. RUC (Benjamin et al. 2004) storm motion estimates, which are based on the Bunkers method (Bunkers et al. 2000, Earth System Research Laboratory 2013) were used as the first guess for the motion of circulations. The Bunkers method is used for estimating supercell motion, and is similar to the defaults of the NSSL MDA of using a first guess of mesocyclone motion that is right of the 0-6 km mean wind (Stumpf et al. 1998). This is a reasonable approach because the distinction between mesovortices and mesocyclones has not been made prior to the tracking for reasons discussed in Section 3.2b. The Bunkers method is generally considered the best existing estimate for the motion of supercells and their mesocyclones. It is unclear how to estimate the initial motion of mesovortices best, and AALTO begins transitioning away from the first guess as soon as a track is established and uses only observed motion to forecast vortex motion once the track has been present for at least 30 minutes (Limpert and Houston 2013).

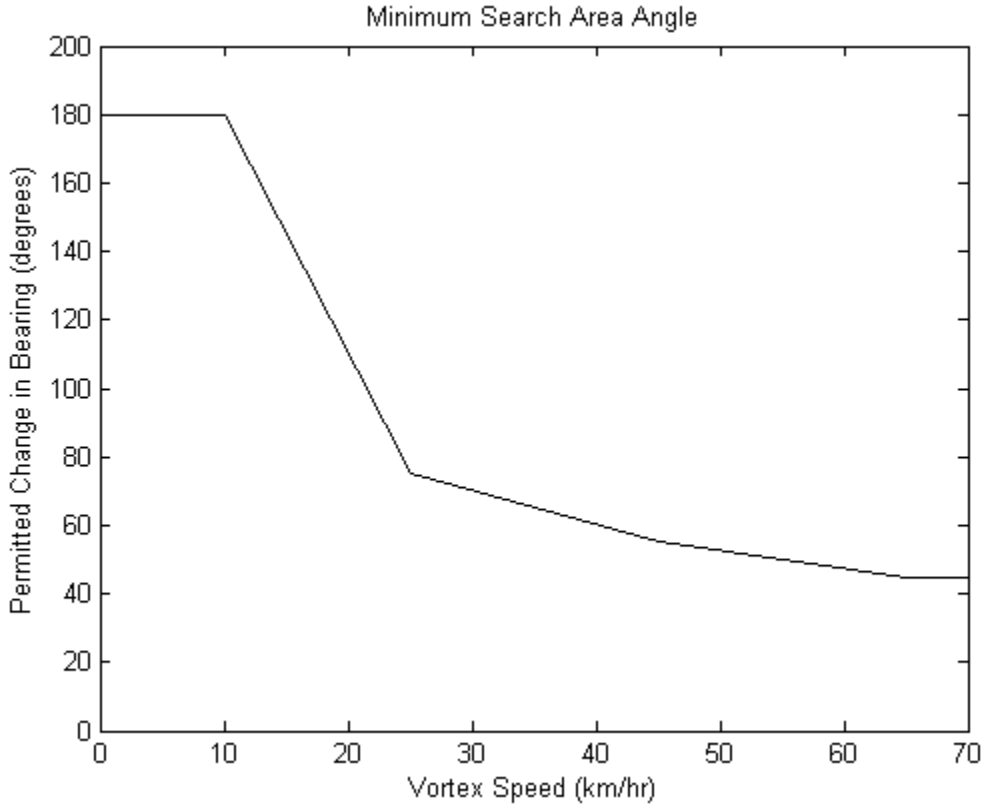

Figure 3.3: The relationship between vortex speed and how the track was permitted to change in direction.

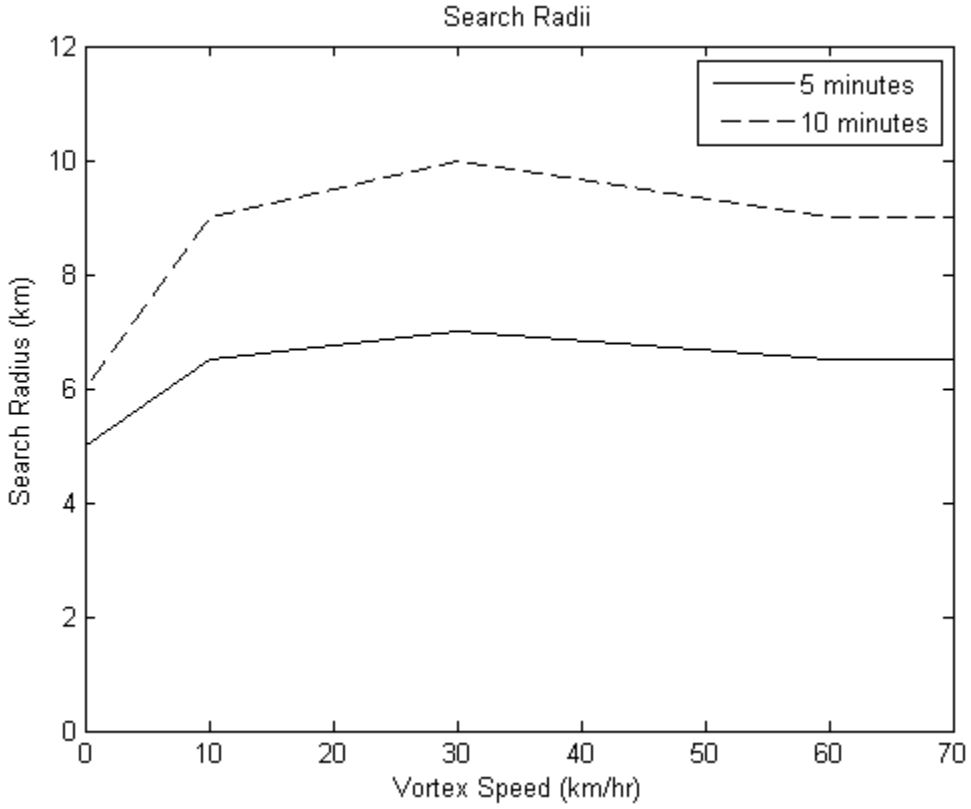

Figure 3.4: The relationship between vortex speed and the search radius.

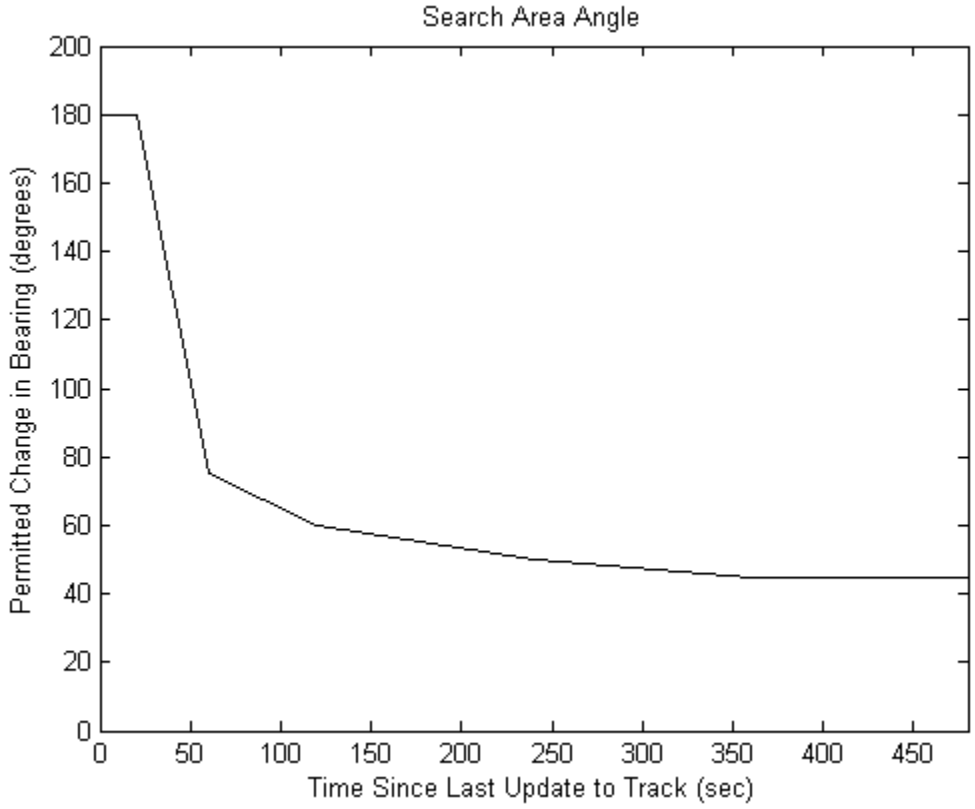

Figure 3.5: The relationship between the time since the last update to the track and how the track was permitted to change in direction.

The resulting tracks included vortex tracks from a variety of sources including spurious detections within clutter, mesocyclones, bow echo mesovortices, and a variety of other circulations that satisfied the criteria of MDA. One key difference between mesovortices and mesocyclones is that these mesovortices originate as low-level circulations whereas mesocyclones are initially strongest in the mid-levels. However, mesocyclones can develop strong low-level rotation and mesovortices may be stretched into the mid-levels. Circulations that were of duration shorter than 12 minutes or in which the height of the maximum shear exceeded 2 km at any point within the first 12 minutes were not considered in this analysis. This step eliminated over 90% of the tracks. The

remaining tracks can be considered persistent low-level circulations, although still of a variety of types.

The tracks were then manually associated with quasi-linear storms in reflectivity mosaics to eliminate circulations associated with discrete storms and those not associated with any storm. Generally, the circulations that were eliminated were those that were not within the convective region of storms, characterized by strong horizontal reflectivity gradients, and not within roughly 15 kilometers of the leading edge of such gradients. One exception was linear storms with leading stratiform precipitation, in which circulations on the trailing edge of convection were retained. The other exception was for the 8 May 2009 derecho event, in which numerous severe reports occurred within the comma head trailing the initial convective line. For this particular event, vortices that trailed the leading convective region were generally retained because of the significant wind damage that occurred behind the initial line of convection. Nearly 75% of the tracks retained by the previous step were discarded by this process.

d. Couplet Identification

Mesovortex couplets were manually identified by displaying both cyclonic and anticyclonic tracks and searching for roughly parallel tracks at similar times. Tracks that began within 10 minutes of each other were candidates to be couplets. This approach is similar to that of Lese and Martinaitis (2010) who identified a mesovortex couplet for which the anticyclonic mesovortex developed approximately nine minutes after the cyclonic mesovortex couplet was first detected. Additionally, a restriction was imposed that the vortices originated within 40 km of each other. Only relatively isolated couplets

were retained. There were many situations in which numerous, roughly parallel tracks occurred in a small area, generally close to a radar. In these instances, rarely were couplets identified, largely because it was unclear which vortices comprised the couplet, if one existed.

The collection of mesovortex tracks was examined to infer the generation mechanism. Couplets in which the cyclonic vortex was to the left (right) of the anticyclonic vortex were considered to be generated by tilting up (down) of baroclinically generated vorticity (Figure 3.6). Figure 3.7 shows an example of a mesovortex couplet presumed to be due to tilting up of vorticity.

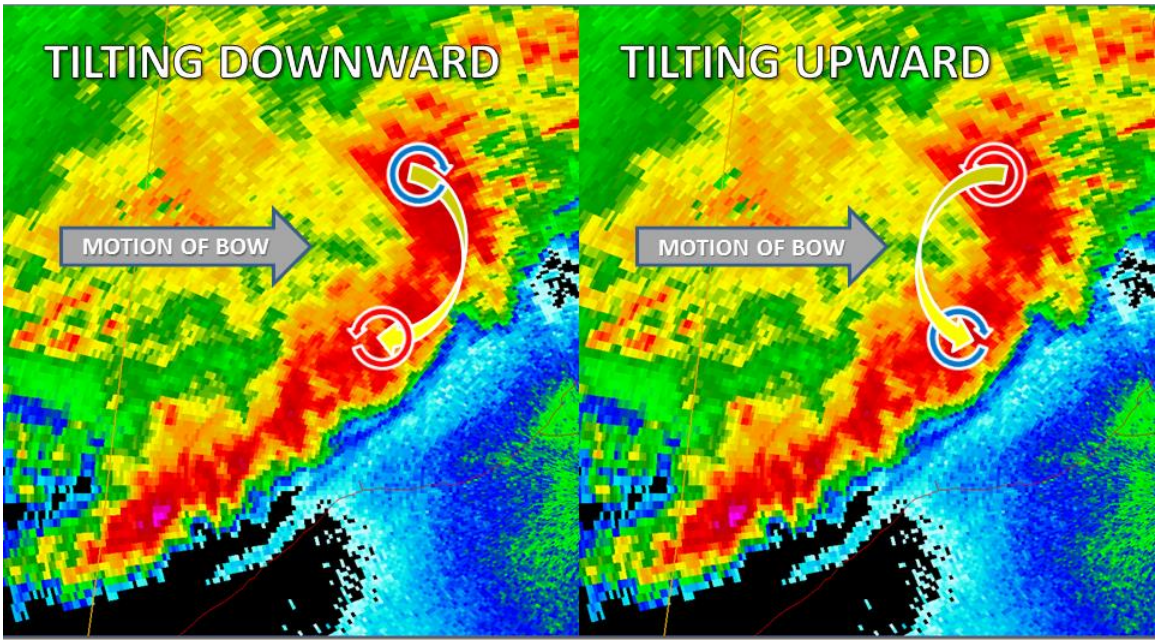

Figure 3.6: The relationship between the position of mesovortices within a bow and the direction that horizontal vorticity is tilted. When tilting up occurs, the cyclonic mesovortex is on the left side of the track. In the case of tilting down, the cyclonic mesovortex is shifted to the right side of the track.

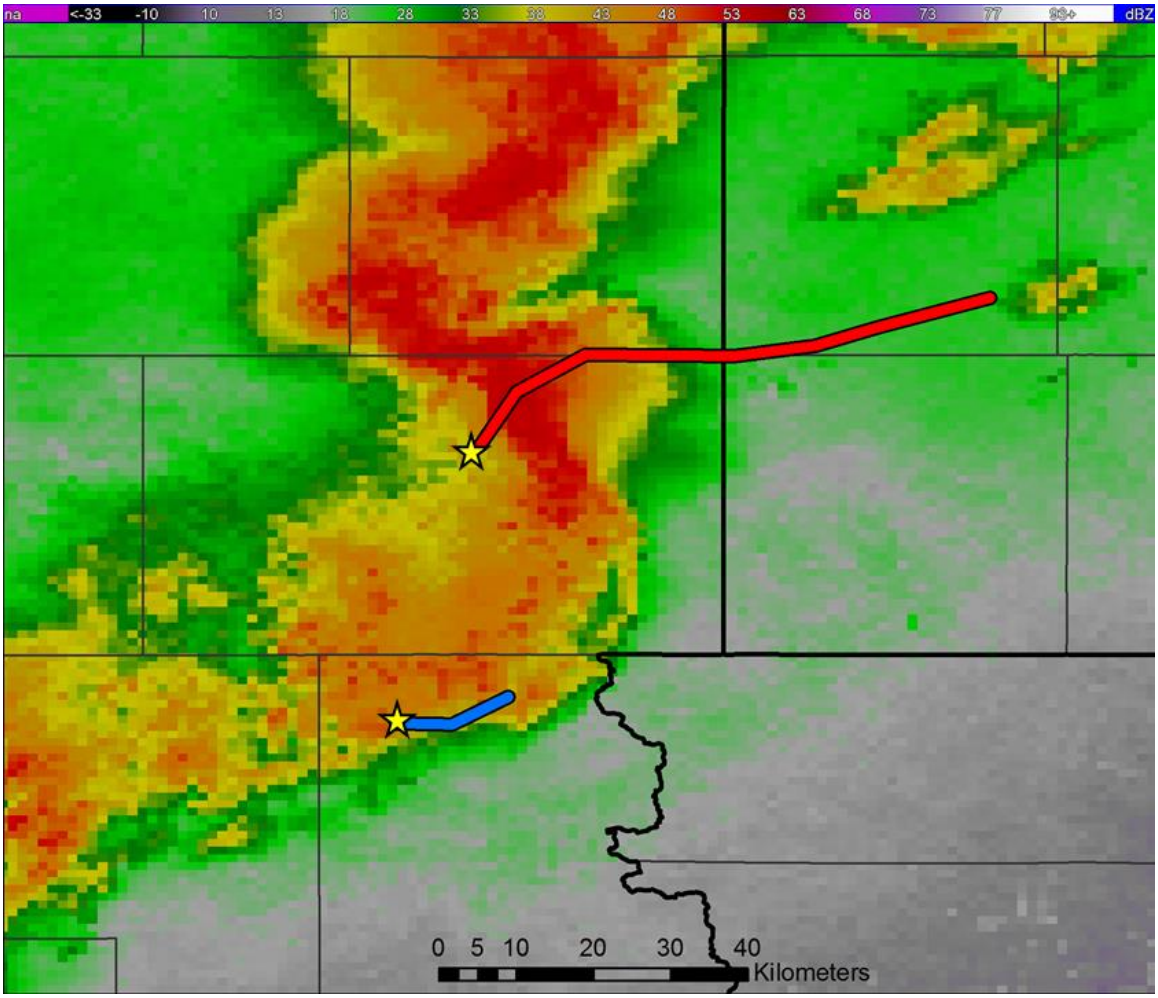

Figure 3.7: An example of a mesovortex couplet, with the composite reflectivity image from 0305 UTC on 24 July 2010 near Sioux Falls, SD. This was approximately the initial time both circulations appeared, with the track of the cyclonic mesovortex shown in red and the anticyclonic mesovortex track shown in blue. Yellow stars indicate the approximate mesovortex positions.

3.3. Climatology Results

Of the 4059 low-level circulation tracks identified from the 44 events, 1032 were retained after discarding tracks not associated with bow echoes or linear convective systems. Of these 1032 tracks, (Figure 3.8), 619 were cyclonic circulations and 413 were anticyclonic. Only 25 isolated couplets were identified, of which 12 appeared to result from the tilting up of vorticity and 13 appeared to occur from tilting down of vorticity.

While there were numerous cases for which it could not readily be determined which process was responsible, there were still a large number of both isolated cyclonic and anticyclonic mesovortices. The lack of couplets can be attributed to two factors: 1) many tracks were sufficiently isolated or surrounded by vortices of the same type with no possibility for a couplet and 2) for some events, many tracks were in such close proximity that the orientation (necessary for determining the generation mechanism) could not be determined. The lack of isolated couplets does not disprove the mechanisms of baroclinically generated horizontal vorticity contributing to mesovortices. Roughly 60% of the mesovortices were cyclonic, suggesting that the stretching of planetary vorticity is suppressing anticyclonic mesovortices (Trapp and Weisman 2003) and/or that tilting of streamwise horizontal vorticity (Atkins and St. Laurent 2009) may be responsible for generating some of the mesovortices. Also of note is that a few events contributed a very large number of vortices to the data set: 13.6% of the events contained 55.6% of the total 1032 circulations. Possible explanations are investigated through analysis of proximity soundings.

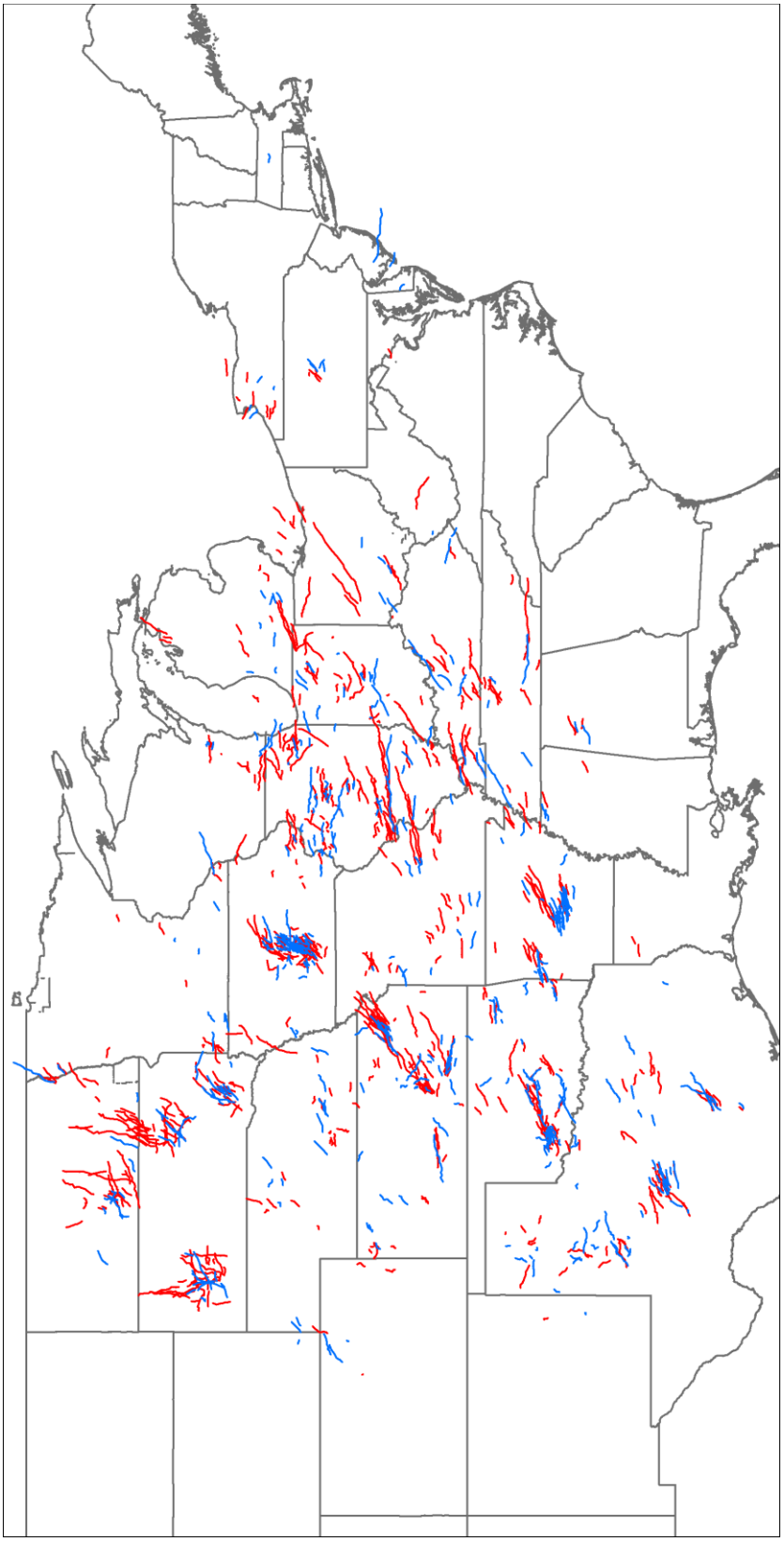

Figure 3.8: A map showing all of the mesovortices in the climatology. Cyclonic mesovortices are in red and anticyclonic mesovortices are in blue.

Many mesovortices were observed to develop along gust fronts, as indicated by convergence lines indicated by thin bands of increased reflectivity on radar. These vortices initially develop along the gust front before being overtaken by the developing thunderstorms (Figure 3.9). Although the track data are noisy due to the inherent nature of radial velocity data and the incorporation of data from multiple radars at varying ranges in the creation of the tracks, the patterns observed suggest a vortex development along the gust front, tethered to updrafts that intensify the vortices through stretching. As these updrafts move rearward and generate precipitation, as would be expected with the classic conceptual model of multicell thunderstorms, the vortices also move rearward and into the precipitation. The generation of these vortices, from the 23 March 2009 event, is likely due to barotropic mechanisms aided by stretching by thunderstorm updrafts, as inferred by the dominance of cyclonic mesovortices and the lack of couplets.

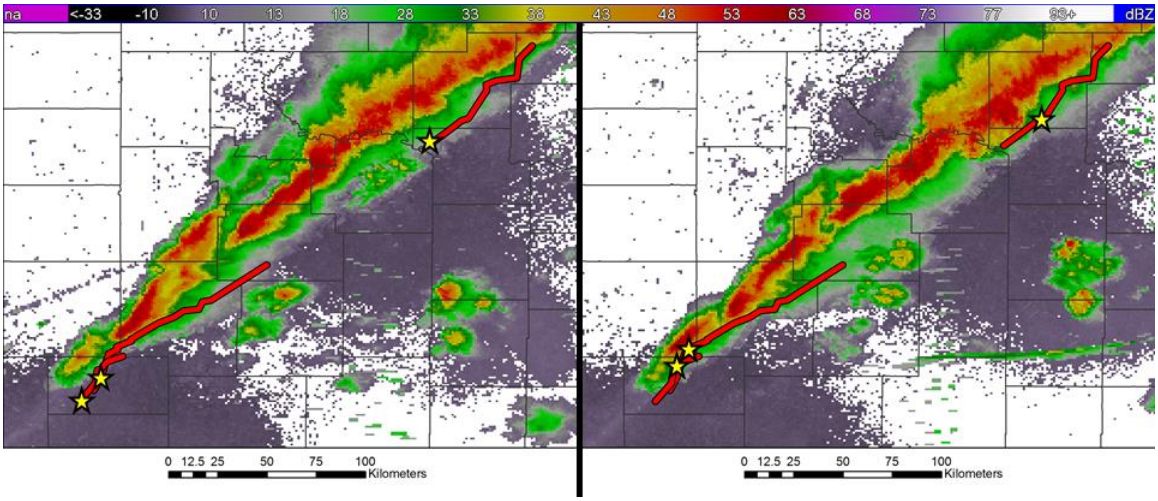

Figure 3.9: Composite reflectivity mosaics at 0245 UTC (left) and 0300 UTC (right) on 24 March 2009. Three cyclonic mesovortex tracks are shown, one originating at 0240 UTC and the others at 0245 UTC. The stars indicate approximate mesovortex position at the time of the mosaic.

Vortices were also observed trailing behind convective regions in some cases, including the 8 May 2009 case (Figure 3.10). These trailing vortices in this event are persistent and are generally very low-level features, with all but one of the seven vortices shown originating with a base at or below 0.5 km. The vortices from this event were not removed from the data set because many severe wind gusts were observed behind the convective region during this event. During the first few hours of this event, most of the mesovortices that developed were trailing the convective region, despite the production of winds in excess of 80 mph in neighboring counties associated with the QLCS. Similar vortices were observed in other events but were removed because of the lack of severe wind reports trailing the initial convective region. The genesis mechanism for these vortices is uncertain.

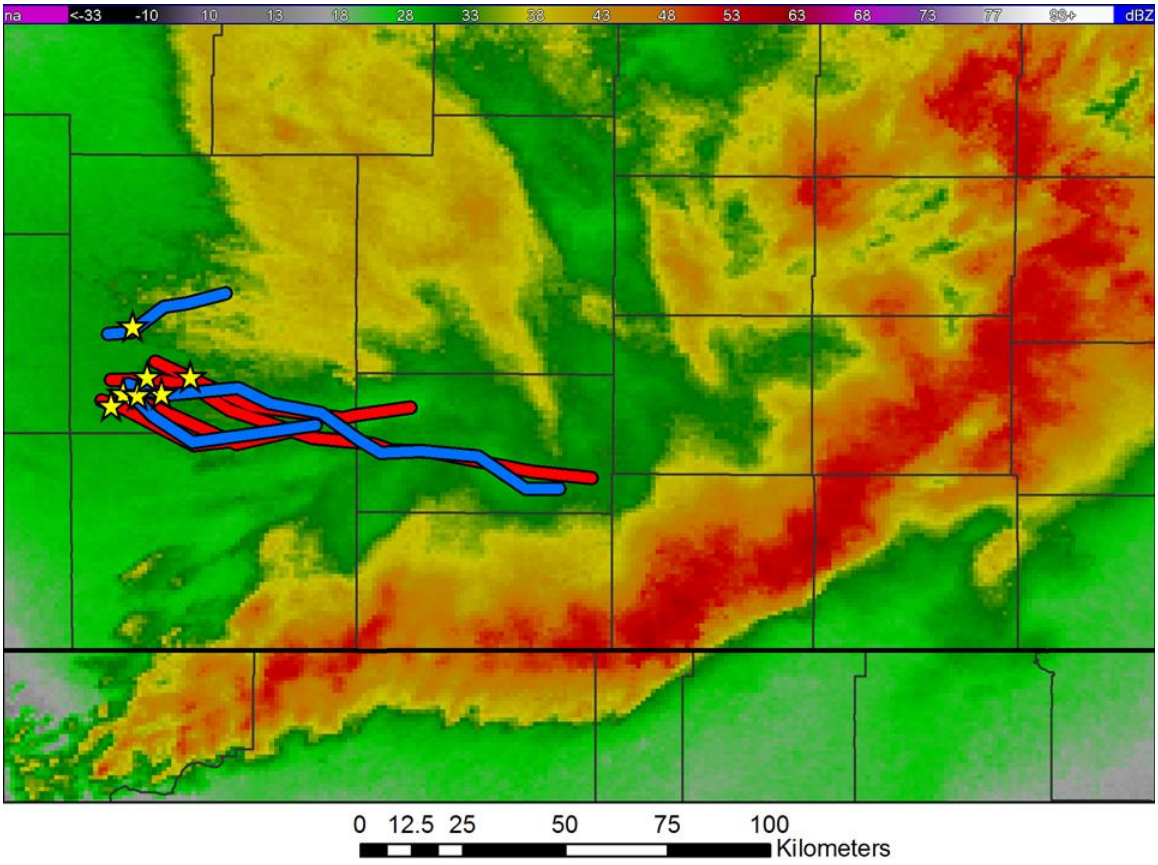

Figure 3.10: Cyclonic (red) and anticyclonic (blue) mesovortices originating at approximately 1125 and 1130 UTC on 8 May 2009. The composite reflectivity image is from 1130 UTC on 8 May 2009.

The entire data set of cyclonic and anticyclonic mesovortices was analyzed for duration and intensity. MSI is a vertically integrated measure of the strength of the vortex based on azimuthal shear that is normalized for the depth of the vortex (Stumpf et al. 1998). The cyclonic mesovortices are slightly stronger; however, this result is not statistically significant (Figure 3.11). Many of the meosovortices are short-lived: the mean duration of cyclonic mesovortices is 1875 seconds with a median of 1522 seconds; for anticyclonic mesovortices, the mean and median were 1624 seconds and 1379 seconds, respectively (Figure 3.12). Although the distinction is statistically significant with a p-value of 0.0003, this is likely due to the large number of vortices in the data set;

the overall distributions have substantial overlap. The greatest difference in vortex characteristics occurs in the peak low-level azimuthal shear during the duration of the mesovortex (Figure 3.13), with cyclonic mesovortices being 5.1 m s^{-1} km^{-1} stronger on average than anticyclonic vortices, a value that is statistically significant with a p-value of 8×10^{-16}.

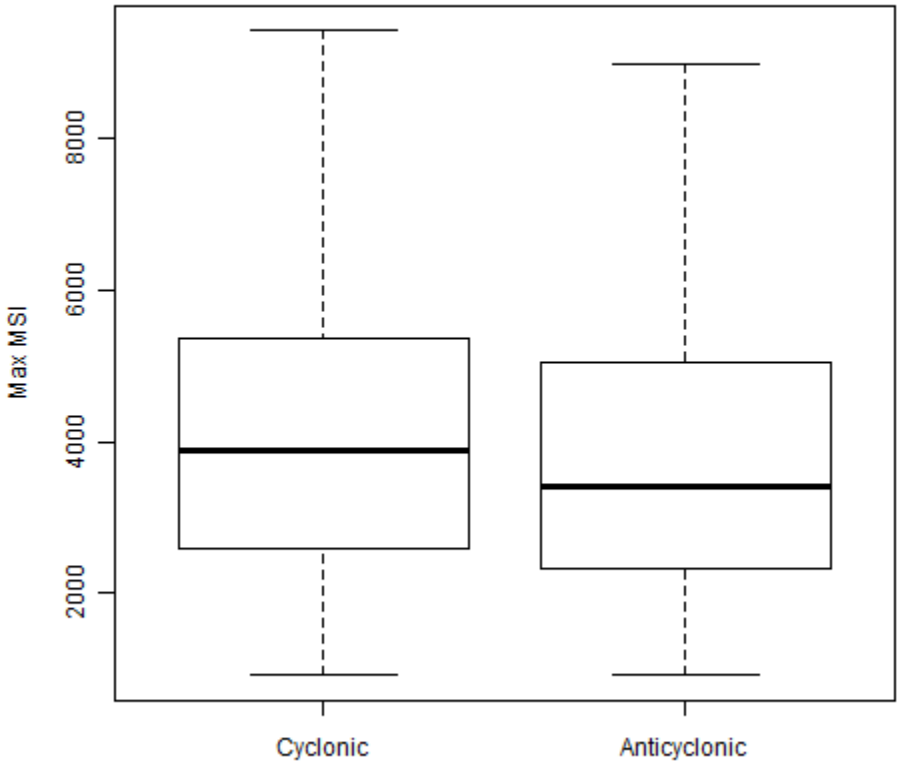

Figure 3.11: The peak mesocyclone strength index during the lifetime of the mesovortices.

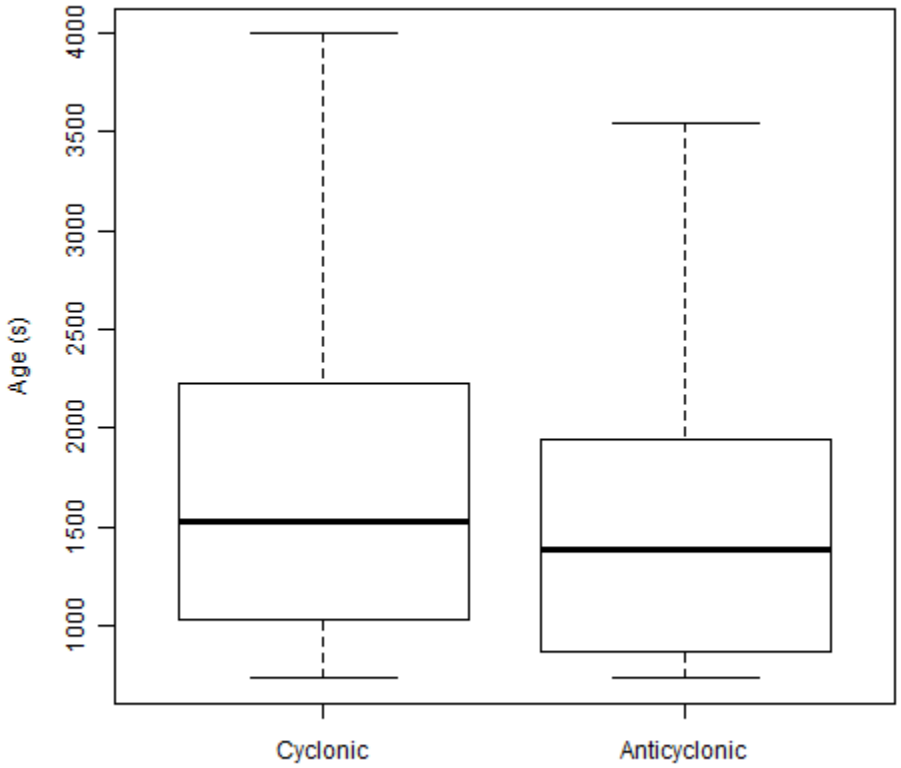

Figure 3.12: The duration of cyclonic and anticyclonic mesovortices.

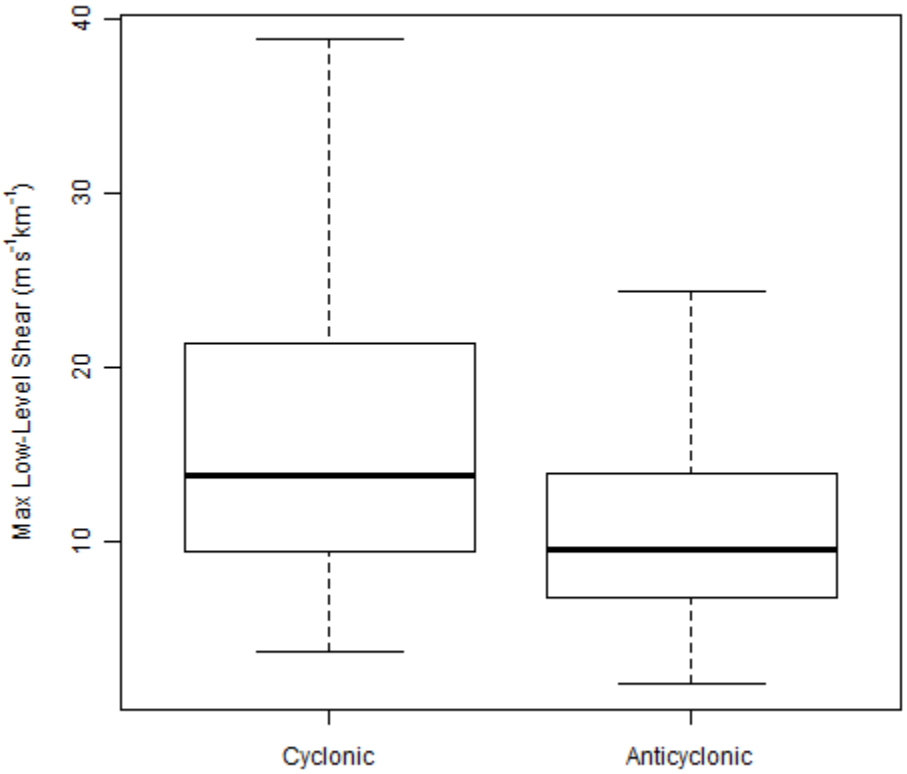

Figure 3.13: The maximum low level azimuthal shear parameter for cyclonic and anticyclonic mesovortices.

3.4. Storm Environments

a. Hypothesis and Methods

As stated previously, a few events were responsible for a disproportionate number of mesovortices, most of which were cyclonic, such as the 23 March 2009 event (Figure 3.14). Possible explanations for this observation will be addressed in this section by examining proximity soundings. Proximity soundings offer information about whether or not environments supportive of barotropic mechanisms are in place for events that produce numerous mesovortices. Mesovortices form through barotropic processes when a

low-level layer of strong horizontal vorticity is tilted upward by the gust front and shearing instability causes the growth of mesovortices. A proposed condition for the generation of vortices through this mechanism is the presence of strong low-level vertical wind shear. The orientation of low-level flow in the generation low-level vortices was examined by Lee and Wilhelmson (2000) who found that strong line-parallel flow favored the genesis of vortices whereas line-perpendicular flow was not necessarily favorable. In the presence of sufficiently ambient strong horizontal shear (Carbone 1983; Mueller and Carbone 1987) or the tilting of horizontal vorticity to produce horizontal shear (Wheatley and Trapp 2008), vortices should develop along the gust front, provided the horizontal shear is unstable to small perturbations (Rayleigh 1880). There are two roles of strong line-parallel, low-level shear: 1) strong line-parallel flow associated with such shears contrasts with weak line-parallel flow in the cold pool generating a strong shear and a vertical vorticity at the gust front (Lee and Wilhelmson 1997) and 2) the ambient horizontal vorticity at low levels is tilted vertically and vortices develop through the release of shearing instability.

To quantify these factors, proximity soundings were analyzed. Vertical shear magnitude, direction, and lapse rates were calculated between the surface and each subsequent level of the sounding. Wheatley and Trapp (2008) suggested that strong shear over the lowest 500 m was associated with the generation of mesovortices through the barotropic mechanism. Moreover, climatologies of proximity soundings to supercells have suggested a link between strong low-level vertical wind shear and tornadoes, especially significant tornadoes (Kerr and Darkow 1996; Markowski et al. 1998;

Montiverdi et al. 2003; Thompson et al. 2003; Craven and Brooks 2004; Dupilka and Reuter 2006; Miller 2006; Esterheld and Guiliano 2008). Although vertical wind shear is typically computed over the lowest 1 km operationally, some evidence has been found of a relationship between shear over the lowest 500 m and significant tornadoes (Miller 2006; Esterheld and Giuliano 2008). Because of the operational use of the 0-1 km layer and the hypothesized relationship between 0-500 m shear and the generation of low-level rotation, shear over both layers was computed.

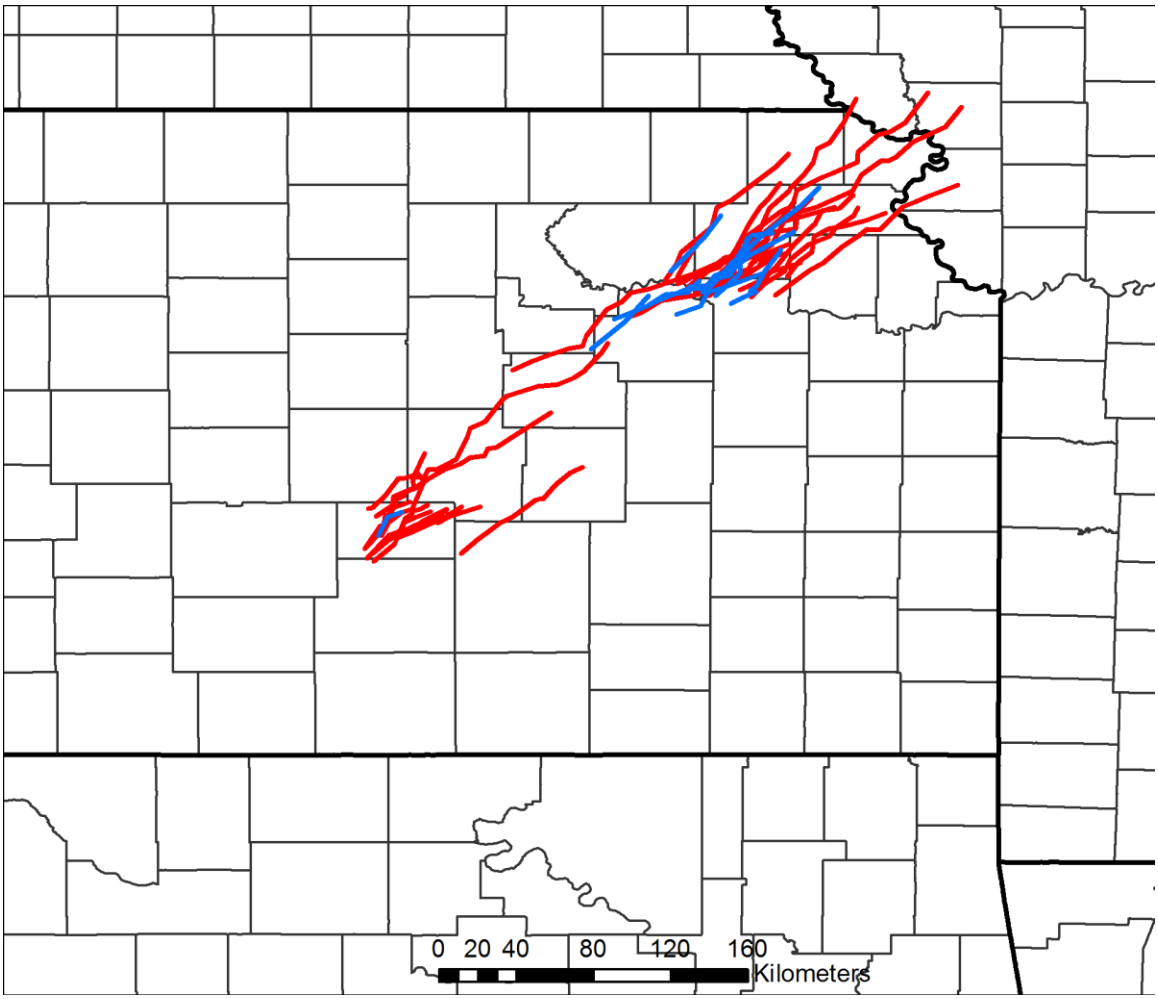

Figure 3.14: The 23 March 2009 event in Kansas. Cyclonic tracks are red; anticyclonic tracks are blue.

Of the 44 events from which mesovortices were identified and tracked, many were unsuitable for this analysis for several reasons: the lack of a proximity sounding, the proximity sounding did not represent the pre-storm environment, or the storms were from an isolated bow or highly curved line of convection from which the line orientation varied greatly over a short distance, thereby rendering the calculation of the line-parallel component of the shear unreliable. Due to the small number of suitable cases, only one or two radar sites were chosen from each event so that the results are not disproportionately influenced by a single event spanning a wide geographic area. Vertical shear and thermodynamic characteristics were computed from unmodified observed soundings at levels from the surface to approximately 500 m and 1000 m, using the closest available levels from the soundings. The number of mesovortices were computed from the number of mesovortex tracks passing within 120 km of the site during the period of four hours on either side of the sounding, or until the beginning or end of the event. Because the intensification of the vortices is due both to shear instability and stretching, the latter being distributed unevenly, this does not necessarily predict spatially periodic vortices along the gust front, which is why this analysis focuses on the number of vortices in relation to environmental factors and ignores their periodicity.

b. Results and Discussion

The results (Tables 3.1 and 3.2 and Figure 3.15) suggest the most obvious discriminator is the presence of a very large line-parallel vertical shear over the first approximately 500 m. The 0-1 km line-parallel vertical shear magnitude was less effective at making the distinction between events with many mesovortices and those

without (Figure 3.16). Fitting a linear model to the line-parallel 0-500 m vertical shear and the total number of mesovortices in the event results in a correlation coefficient of 0.7668 and a p-value of 0.0003, indicating that it is a statistically significant result. In contrast, the correlation coefficient and p-value for the 0-1 km line-parallel vertical shear and mesovortex count are 0.4783 and 0.0522, respectively.

Table 3.1: Values of vertical shear and static stability over the lowest 500 m for several events.

Event (Time/Date and WSR-88D Radar Used)	Mesovortex Count	0-500 m Layer Depth	Approx. 0-500 m Shear Direction	Approx. 0-500 m Shear Magnitude	Approx. 0-500 m Static Stability
00 UTC 24 Mar. 2009 KTOP	24 cyclonic, 11 anticyclonic, 35 total	387 m	188°	46.27 m s^{-1} km^{-1}	-2.58 K km^{-1}
12 UTC 08 May 2009 KSGF	10 cyclonic, 1 anticyclonic, 11 total	527 m	230°	29.72 m s^{-1} km^{-1}	9.87 K km^{-1}
00 UTC 14 May 2009 KILX	5 cyclonic, 2 anticyclonic, 7 total	472 m	206°	33.85 m s^{-1} km^{-1}	6.78 K km^{-1}
00 UTC 12 Jun. 2009 KBNA	2 cyclonic, 2 anticyclonic, 4 total	569 m	225°	9.04 m s^{-1} km^{-1}	0.53 K km^{-1}
18 UTC 12 Jun. 2009 KLZK	0 cyclonic, 1 anticyclonic, 1 total	616 m	226°	5.47 m s^{-1} km^{-1}	-1.95 K km^{-1}
00 UTC 16 Jun. 2009 KTOP	2 cyclonic, 1 anticyclonic, 3 total	470 m	104°	2.77 m s^{-1} km^{-1}	-0.64 K km^{-1}
00 UTC 25 Jul. 2009 KDVN	0 cyclonic, 0 anticyclonic, 0 total	510 m	209°	9.55 m s^{-1} km^{-1}	-0.59 K km^{-1}
00 UTC 30 Jul. 2009 KAMA	3 cyclonic, 3 anticyclonic, 6 total	378 m	199°	7.47 m s^{-1} km^{-1}	-0.26 K km^{-1}
12 UTC 10 Aug. 2009 KSGF	0 cyclonic, 0 anticyclonic, 0 total	527 m	173°	5.12 m s^{-1} km^{-1}	2.09 K km^{-1}
00 UTC 25 May 2010 KABR	21 cyclonic, 6 anticyclonic, 27 total	518 m	177°	38.79 m s^{-1} km^{-1}	8.30 K km^{-1}
00 UTC 18 Jun. 2010 KOAX	0 cyclonic, 0 anticyclonic, 0 total	532 m	220°	18.80 m s^{-1} km^{-1}	5.08 K km^{-1}
00 UTC 19 Jun. 2010 KILX	11 cyclonic, 8 anticyclonic, 19 total	432 m	195°	20.24 m s^{-1} km^{-1}	2.08 K km^{-1}
00 UTC 23 Jun. 2010 KLBF	1 cyclonic, 1 anticyclonic, 2 total	370 m	163°	7.36 m s^{-1} km^{-1}	-1.62 K km^{-1}
00 UTC 24 Jun. 2010 KILX	5 cyclonic, 3 anticyclonic, 8 total	432 m	207°	25.07 m s^{-1} km^{-1}	-0.93 K km^{-1}
00 UTC 28 Jun. 2010 KILN	0 cyclonic, 0 anticyclonic, 0 total	529 m	226°	18.73 m s^{-1} km^{-1}	-0.38 K km^{-1}
00 UTC 27 Jul. 2010 KBIS	2 cyclonic, 0 anticyclonic, 2 total	408 m	190°	15.13 m s^{-1} km^{-1}	-0.98 K km^{-1}
00 UTC 22 Sep. 2010 KTOP	1 cyclonic, 0 anticyclonic, 1 total	476 m	216°	18.05 m s^{-1} km^{-1}	0.00 K km^{-1}

Table 3.2: Values of 0-1 km vertical shear, the squall line orientation, and the difference between the orientation and the 0-500 m vertical shear.

Event (Time/Date and WSR-88D Radar Used)	Mesovortex Count	Approx. Squall Line Orientation	Approx. 0-1 km Shear Magnitude	0-1 km Layer Depth	Shear Difference
00 UTC 24 Mar. 2009 KTOP	24 cyclonic, 11 anticyclonic, 35 total	215°	15.19 m s^{-1} km^{-1}	949 m	27°
12 UTC 08 May 2009 KSGF	10 cyclonic, 1 anticyclonic, 11 total	220°	11.31 m s^{-1} km^{-1}	1050 m	10°
00 UTC 14 May 2009 KILX	5 cyclonic, 2 anticyclonic, 7 total	225°	16.04 m s^{-1} km^{-1}	996 m	19°
00 UTC 12 Jun. 2009 KBNA	2 cyclonic, 2 anticyclonic, 4 total	265°	9.31 m s^{-1} km^{-1}	1039 m	40°
18 UTC 12 Jun. 2009 KLZK	0 cyclonic, 1 anticyclonic, 1 total	200°	9.13 m s^{-1} km^{-1}	1047 m	26°
00 UTC 16 Jun. 2009 KTOP	2 cyclonic, 1 anticyclonic, 3 total	150°	3.95 m s^{-1} km^{-1}	949 m	46°
00 UTC 25 Jul. 2009 KDVN	0 cyclonic, 0 anticyclonic, 0 total	280°	7.24 m s^{-1} km^{-1}	991 m	71°
00 UTC 30 Jul. 2009 KAMA	3 cyclonic, 3 anticyclonic, 6 total	205°	4.57 m s^{-1} km^{-1}	1035 m	6°
12 UTC 10 Aug. 2009 KSGF	0 cyclonic, 0 anticyclonic, 0 total	285°	5.68 m s^{-1} km^{-1}	832 m	112°
00 UTC 25 May 2010 KABR	21 cyclonic, 6 anticyclonic, 27 total	165°	20.02 m s^{-1} km^{-1}	1034 m	12°
00 UTC 18 Jun. 2010 KOAX	0 cyclonic, 0 anticyclonic, 0 total	225°	13.35 m s^{-1} km^{-1}	869 m	5°
00 UTC 19 Jun. 2010 KILX	11 cyclonic, 8 anticyclonic, 19 total	245°	8.77 m s^{-1} km^{-1}	1013 m	50°
00 UTC 23 Jun. 2010 KLBF	1 cyclonic, 1 anticyclonic, 2 total	190°	4.77 m s^{-1} km^{-1}	980 m	27°
00 UTC 24 Jun. 2010 KILX	5 cyclonic, 3 anticyclonic, 8 total	255°	13.34 m s^{-1} km^{-1}	1041 m	48°
00 UTC 28 Jun. 2010 KILN	0 cyclonic, 0 anticyclonic, 0 total	235°	17.33 m s^{-1} km^{-1}	902 m	9°
00 UTC 27 Jul. 2010 KBIS	2 cyclonic, 0 anticyclonic, 2 total	245°	7.97 m s^{-1} km^{-1}	975 m	55°
00 UTC 22 Sep. 2010 KTOP	1 cyclonic, 0 anticyclonic, 1 total	285°	11.98 m s^{-1} km^{-1}	949 m	69°

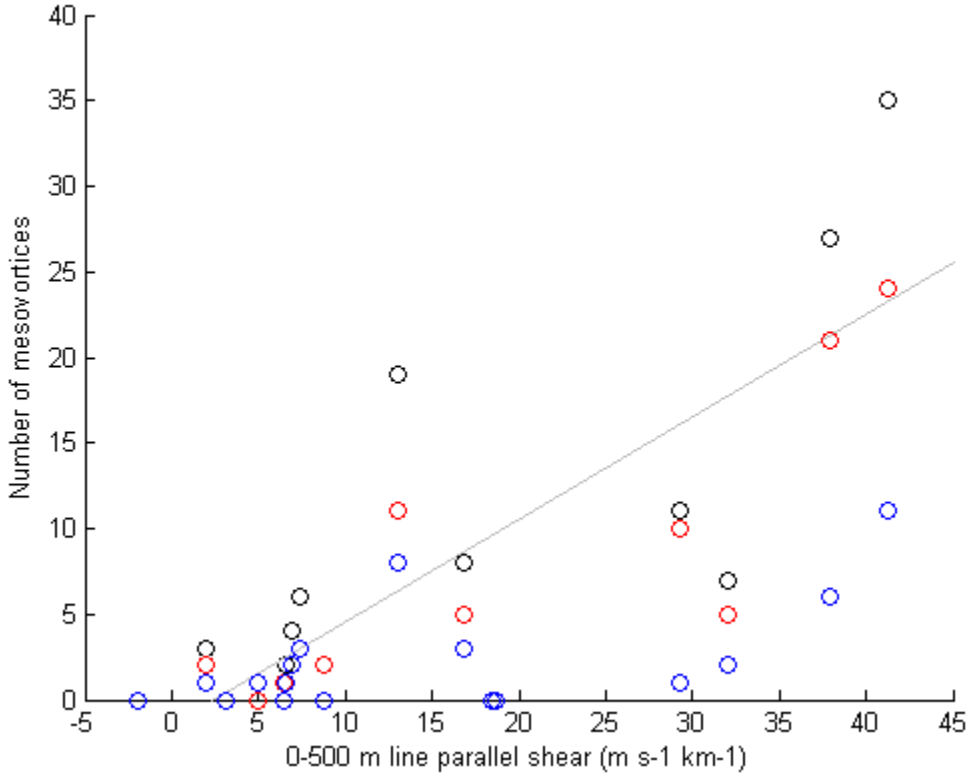

Figure 3.15: The relationship between 0-500m line-parallel shear and the number of mesovortices in the case. Plotted is the best fit line obtained using a linear model. The cyclonic mesovortex count is in red and the anticyclonic is in blue.

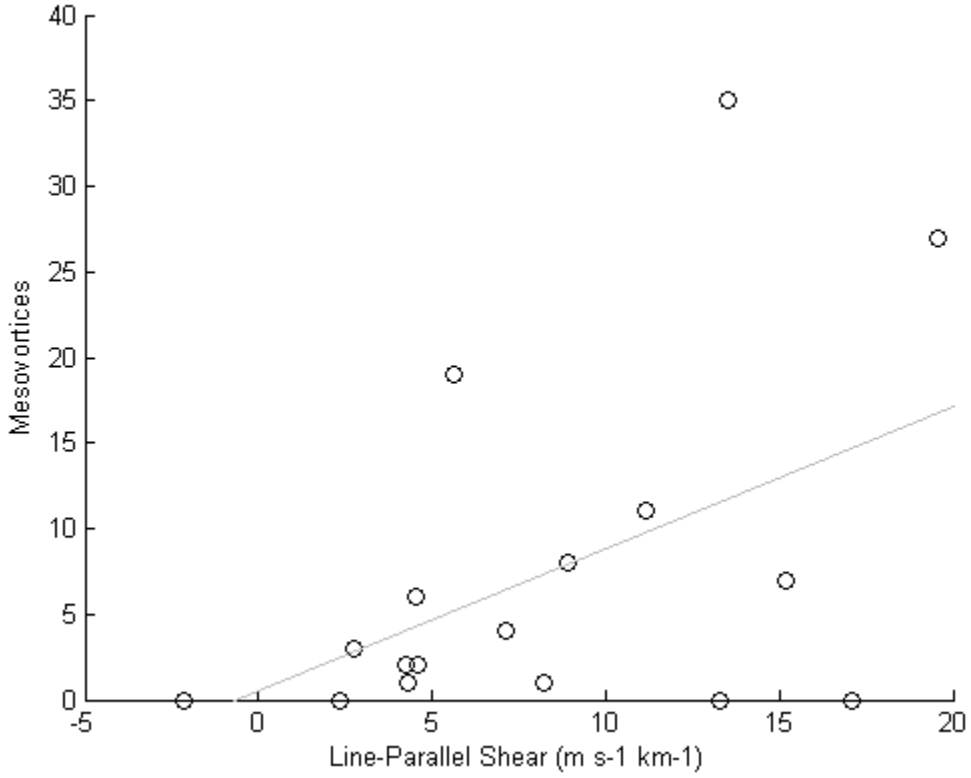

Figure 3.16: The relationship between 0-1km line-parallel shear and the number of mesovortices in the case. Plotted is the best fit line obtained using a linear model.

The correlation matrix and the p-value of the correlations for the mesovortex and environmental variable data that were recorded (Table 3.3) reveal the positive, although not strong, relationship between 0-500 m static stability and the 0-500 m vertical wind shear magnitude (Figure 3.17). When the outlier data point with a vertical shear magnitude of ~45 m s^{-1} km^{-1} (corresponding to the 00 UTC 24 March 2009 KTOP profile that is absolutely unstable in the 0-500 m layer but with a very large vertical wind shear, unlike other events with large shears) is removed, the correlation coefficient is 0.7634

and the p-value is 0.0006, indicating a statistically significant relationship between 0-500 m static stability and vertical shear magnitude. Although ambient static stability is considered unfavorable for the development of low-level rotation in supercells, increased static stability appears to be associated with more mesovortices. A likely explanation is that increasing the static stability reduces the influence of friction with at the top of the 0-500 m layer, which increases the vertical shear, which is proposed to be favorable for the barotropic mechanism.

Table 3.3: Correlation coefficients and p-values for linear models between mesovortices and the variables recorded.

	Total Mesovortices	**0-500 m Shear Magnitude**	**0-500 m Stability**	**Directional Difference**	**0-1 km Shear Magnitude**
Total Mesovortices	1.0000 (0.0000)				
0-500 m Shear Magnitude	0.7931 (0.0001)	1.0000 (0.0000)			
0-500 m Stability	0.2096 (0.4195)	0.4503 (0.0697)	1.0000 (0.0000)		
Directional Difference	-0.2632 (0.3074)	-0.3800 (0.1324)	-0.3165 (0.2159)	1.0000 (0.0000)	
0-1 km Shear Magnitude	0.4728 (0.0553)	0.8161 (0.0001)	0.4420 (0.0757)	-0.4341 (0.0817)	1.0000 (0.0000)

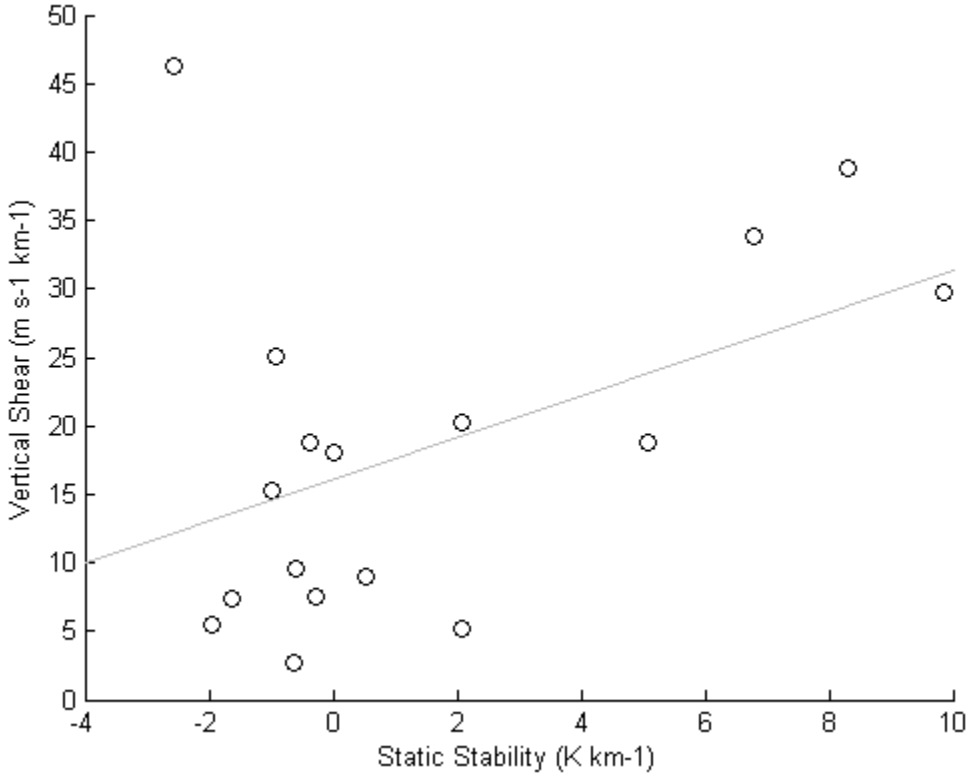

Figure 3.17: The relationship between 0-500 m static stability and the 0-500 m vertical wind shear. Plotted is the best fit line obtained using a linear model.

A second relationship of note is that the correlation between the number of mesovortices and the 0-500 m line-parallel vertical shear magnitude is actually higher than its correlation to the 0-500 m line-normal shear (Table 3.4). Moreover, the correlation between line-parallel shear and the number of cyclonic mesovortices is appreciably larger than the correlation between line-parallel shear and the number of anticyclonic mesovortices. There is also a statistically significant correlation between line-normal 0-500 m shear magnitude and the generation of mesovortices, likely owing to the influences of low-level vertical shear on the gust front as suggested by Lee and Wilhelmson (1997, 2000). However, given that the barotropic mechanism tends to favor cyclonic over anticyclonic mesovortices (Wheatley and Trapp 2008), these results

support the importance of the barotropic mechanism for events that produce numerous mesovortices.

Table 3.4: Correlation coefficients and p-values between total, cyclonic, and anticyclonic mesovortices and the various components of 0-500 m and 0-1 km vertical shear magnitude

	Total Mesovortices	**Cyclonic Mesovortices**	**Anticyclonic Mesovortices**
Total 0-500 m Shear Magnitude	0.7931/0.000145	0.8291/0.000039	0.6427/0.0054
Line-Parallel 0-500 m Shear Magnitude	0.7668/0.000329	0.8100/0.000081	0.6023/0.0105
Line-Normal 0-500 m Shear Magnitude	0.5309/0.0283	0.5007/0.0406	0.5559/0.0205
Total 0-1 km Shear Magnitude	0.4728/0.0553	0.5211/0.0320	0.3212/0.2087
Line-Parallel 0-1 km Shear Magnitude	0.4783/0.0522	0.5223/0.0315	0.3361/0.1872
Line-Normal 0-1 km Shear Magnitude	0.1315/0.6149	0.1078/0.6804	0.1752/0.5012

3.5. Conclusion

The objective of this work was to examine many events containing mesovortices to identify which genesis mechanisms are most frequently responsible for the development of mesovortices. Mesovortex tracks were constructed during 44 events over the conterminous United States east of 105°W from 2009 and 2010 to evaluate the frequency, longevity, and strength of cyclonic and anticyclonic mesovortices. In contrast with prior observational studies, anticyclonic mesovortices were found to be somewhat more frequent relative to cyclonic mesovortices. Mesovortex couplets were rare among the tracks that were compiled, though it does not rule out genesis mechanisms that suggest that such couplets should develop. Cyclonic mesovortices were longer-lived and stronger near the surface than their anticyclonic counterparts, likely owing to the concentration of planetary vorticity as hypothesized by Trapp and Weisman (2003). An additional factor to explain the lack of couplets was the large number of mesovortices in

some events; the close proximity of these mesovortices prevented determining the orientation of any possible mesovortex couplets within these regions.

The large number of mesovortices within these few events is likely due to low-level horizontal vorticity resulting from the strong vertical wind shear, which is tilted upward, and mesovortices develop through the release of shearing instability. Low-level vertical shear and static stability were computed from proximity soundings to provide support for this mechanism and suggest which storm environments are most conducive for the barotropic mechanism of mesovortex formation. In particular, strong line-parallel vertical shear over the lowest 500 m above ground level appears to be supportive of the development of mesovortices through the release of barotropic instability. A relationship between 0-1 km shear and tornado likelihood is often implied in operational tornado forecasting. However, similar to the findings of previous studies of tornadogenesis and bow echo mesovortices, this suggests that an even shallower layer is more relevant to the genesis of mesovortices, such as 0-500 m. The barotropic mechanism hypothesis predicts that events in which this process is relevant will be characterized by a dominance of cyclonic mesovortices. Line-parallel 0-500 m shear magnitude was much more strongly correlated to the frequency of cyclonic mesovortices than anticyclonic mesovortices. In contrast, the correlations of cyclonic and anticyclonic mesovortices to 0-500 m line-normal shear were much closer. This supports the conclusion that strong 0-500 m line-parallel shear is supportive of the barotropic mechanism and that this process is responsible for the numerous mesovortices observed in a few of the events. In contrast with the hypothesized role of low-level stability reducing the potential for

tornadogenesis, it appears that increased low-level static stability allows for strong vertical shear over the lowest few hundred meters above ground level that is necessary for the barotropic mechanism of mesovortex formation. Although there are likely several mechanisms that produce mesovortices, the barotropic mechanism is responsible when numerous mesovortices are generated within a single event. In a nowcasting setting, the strength of the 0-500 m line-parallel shear is a good predictor of whether numerous mesovortices are likely to develop.

Chapter 4: Effects of Low-Level Stability

4.1. Introduction

Observational studies have found that small circulations, or mesovortices, within bow echoes and quasi-linear convective systems (QLCSs) are frequently associated with swaths of enhanced wind damage (Przybylinski et al. 2000; Schmocker et al. 2000; Wheatley et al. 2006). Although mesovortices are a significant severe weather hazard, skill in forecasting and warning for their development is limited because of their rapid development and dissipation (Atkins et al. 2004, Wheatley et al. 2006, Lese and Martinaitis 2010). Moreover, the processes responsible for mesovortex genesis are not well understood, although a number of hypotheses have been proposed to explain their formation. The hypothesized processes can be divided into baroclinic mechanisms that generate and redistribute vorticity generated by cold pool temperature gradients and barotropic mechanisms that reorient and concentrate ambient vorticity. The hypotheses that implicate a baroclinic mechanism in mesovortex genesis begin with the creation of horizontal vorticity within the cold pool. Vertical vorticity of the mesovortex has been hypothesized to arise from upward tilting of streamwise horizontal vorticity to produce a cyclonic mesovortex (Atkins and St. Laurent 2009), upward tilting of crosswise vorticity to create arched vortex lines and couplets of cyclonic and anticyclonic mesovortices (Weisman and Davis 1998; Atkins and St. Laurent 2009), downward tilting of crosswise vorticity by downdrafts resulting in vortex line saddles and mesovortex couplets (Trapp and Weisman 2003). This chapter focuses on the hypothesized interaction between

updrafts and crosswise horizontal vorticity, and its similarities to analogous hypotheses that explain the development of low-level rotation in supercells.

Although most supercell tornadoes develop within regions of strong cyclonic vertical vorticity, many observations have been made of a neighboring region of weaker, anticyclonic vorticity, as summarized by Markowski et al. (2002). Analyses of vortex lines within the rear flank downdraft region of tornadic supercells has found arches in which tornadoes are frequently found within a region of strong cyclonic vorticity with weaker anticyclonic vorticity on the opposite side of the hook echo (e.g., Straka et al. 2007; Markowski et al. 2008). It is hypothesized that baroclinic vorticity develops within the rear flank region and is then tilted upward by an updraft to produce the arches. Many analyses have suggested that negative temperature perturbations within the rear flank downdraft are strongly related to the ability of the storm to produce vertical vorticity (e.g., Markowski et al. 2002; Markowski et al. 2003; Grzych et al. 2007). Generation of vorticity by baroclinic mechanisms is directly related to the negative potential temperature perturbations within the cold pool such that stronger cold pools have greater potential to generate strong horizontal vorticity. However, the negative buoyancy within a cold pool tends to inhibit the ascent of cold parcels, limiting the production of vertical vorticity through upward tilting as cold pool strength increases. An intermediate condition is hypothesized to be optimal, in which the temperature gradient is sufficiently strong to produce strong baroclinic vorticity while not resisting vertical displacement to the point that vertical vorticity does not develop (Markowski et al. 2010).

An analogous hypothesis is proposed here that relates the strength of a QLCS cold pool to the generation of mesovortices. A potentially significant difference between a supercell and a QLCS is that supercells typically have a quasi-steady updraft whereas updrafts in a QLCS may be advected rearward resulting in a series of cells periodically developing near the gust front (Chalon et al. 1976; Browning 1977; Thorpe and Miller 1978; Wilhelmson and Chen 1982; Droegemeier and Wilhelmson 1985; Fovell and Ogura 1988, 1989). Updrafts that have longer residence times over the gust front should allow for greater stretching of vertical vorticity, thereby resulting in stronger mesovortices. To evaluate the proposed hypothesis, a series of model simulations were performed in which the sensitivity of mesovortices to the cold pool strength and gust front relative updraft motion is tested. Experiment design is guided by the prior work such as that of Atkins and St. Laurent (2009) and Markowski et al. (2010). Results and analysis of these simulations will be presented in this chapter.

4.2. Methodology

A series of numerical simulations were conducted using the Cloud Model 1 (CM1) release 16 nonhydrostatic cloud model (Bryan and Fritsch 2002). Highly idealized, completely dry simulations were performed with the cold pool generated by a heat sink while a heat source located near the center of the domain created an updraft. Dry simulations were conducted because if moist convection was directly simulated, the necessary adjustments to test the parameter space would potentially introduce feedbacks affecting the moist convection (e.g. Rotunno et al. 1988; Weisman 1992) and the resulting cold pool (Xu 1992) and preclude testing only the effects of cold pool strength

and gust front relative updraft motion. The all dry assumption is not tested, though it is assumpted that the simulations are adequate to represent the relevant dynamic processes.

Simulations were conducted in a domain with a horizontal grid spacing of 500 m and a vertical grid spacing of 160 m in the low levels, consistent with that of Atkins and St. Laurent (2009). The grid was 13 km deep and stretched vertically to a 400 m spacing at the top of the domain. The domain was 80 km long in the zonal direction and 40 km long in the meridional direction. The north and south lateral boundary conditions were periodic while the east and west boundaries were open. The domain bottom and top were rigid with Rayleigh damping applied above 10 km to suppress reflection of waves off the domain top. The effects of Coriolis were enabled using a constant parameter throughout the domain consistent with mid-latitude regions. Surface momentum fluxes were enabled and coupled to the wind speed using the coefficient of drag formulation of Fairall et al. (2003) for low wind speeds and Donelan et al. (2004) for high wind speeds. The simulations used Klemp-Wilhelmson time splitting with acoustic modes handled implicitly in the vertical direction and explicitly for the horizontal directions. A fifth order horizontal and vertical advection scheme was used with implicit diffusion.

Initialization was from a statically stable base state sounding with a 0.5 K km^{-1} potential temperature increase over the lowest 1 km with a 1 K km^{-1} increase from 1 km and 10 km, and a 10 K km^{-1} increase from 10 km to the model top. There was no meridional flow in the base state. Surface winds were from the east at 6 m s^{-1} with a 2 m s^{-1} km^{-1} shear through 10 km, with no shear above that level.

A heat sink spanning the western boundary of the domain is responsible for the generation of the cold pool. Because the simulations are completely dry, the heat sink is necessary to represent the diabatic cooling that would occur within thunderstorms. The heat sink has a zonal width of 5.4 km and a depth of 7 km. Similar to other heat sink implementations (e.g., Dudhia and Moncrieff 1989; Garner and Thorpe 1992; Fovell and Tan 2000; Lin and Joyce 2001; Markowski et al. 2010), the heat sink was implemented by modifying the potential temperature tendency equation and decreasing the potential temperature at each grid point within the heat sink at a prescribed rate. Peak cooling is at the surface, modulated by a cosine function moving up and laterally away from the center of the heat sink, resulting in a meridionally uniform cold pool that develops shortly after the start of the simulation. Limits are placed on how cold parcels within the heat sink can become, similar to an approach adopted by Fovell (2003). When a grid point reaches a prescribed potential temperature perturbation, the cooling is throttled according to a cosine function. If the potential temperature perturbation exceeds a second threshold, set to twice the limit for throttling the cooling, the heat sink does not act on the grid point at that time. The cooling function for the heat sink at each grid point and each time step is

$$\frac{\partial \theta}{\partial t} = \begin{cases} \frac{\partial \theta_{max}}{\partial t} \text{ if } \theta' > \theta_{throttle} \\ \frac{\partial \theta_{max}}{\partial t} \cos\left(\frac{\pi}{2}(\theta' - \theta_{throttle})\right) \text{ if } \theta' \geq \theta_{limit} \text{ and } \theta' \leq \theta_{throttle} \\ 0 \text{ if } \theta' < \theta_{limit} \end{cases} \quad (4.1)$$

where θ' is the potential perturbation at the grid point, $\partial\theta_{max}/\partial$t is the peak rate of cooling, $\theta_{throttle}$ is the perturbation at which throttling begins, and θ_{limit} is the point at which cooling stops. This function is valid for the center of the heat sink and is modulated by a cosine function moving away from the center (Figure 4.1).

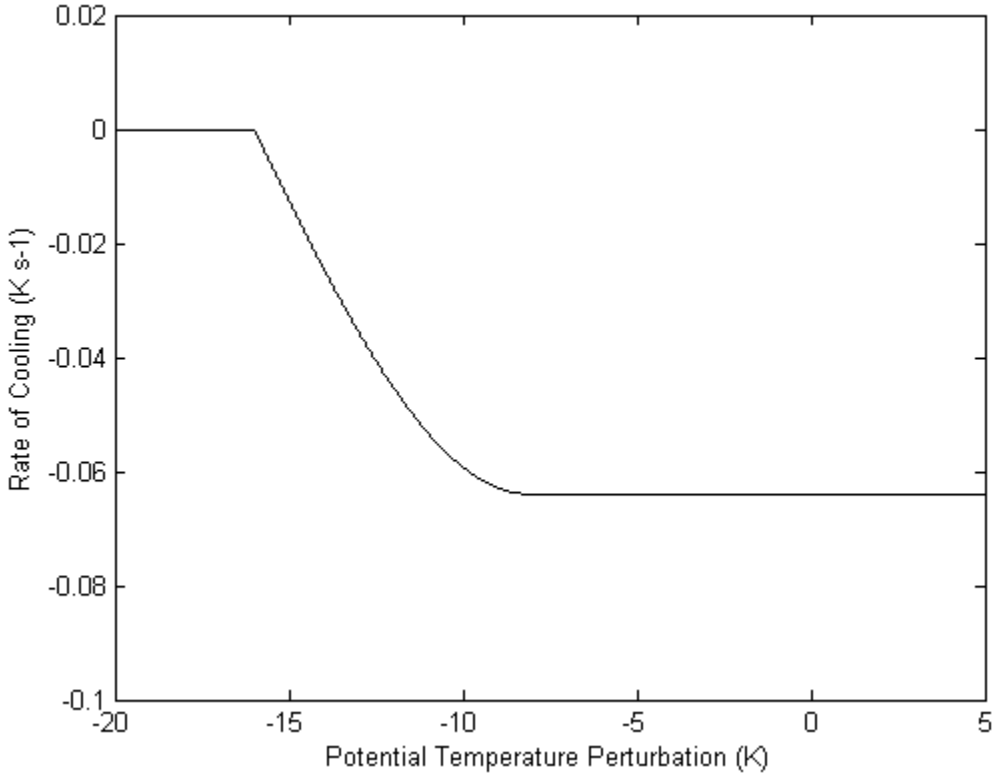

Figure 4.1: The rate of cooling by the heat sink for the strongest density current. The largest permissible potential temperature perturbation is -16 K and throttling begins at -8 K. The maximum rate of cooling is 0.064 K s^{-1}. This rate of cooling is at the center of the heat sink.

Once the gust front reaches 20 km from the western boundary of the domain, the heat sink starts moving eastward. The rate of motion is approximately 80% of the motion of the gust front that would occur if the heat sink remained stationary. This limits the displacement between the heat sink and the head of the density current, resulting in a density current that maintains its structure longer than if the heat sink was not advected.

The heat sink is activated at the start of simulations. The strength of the density current is controlled with the θ_{limit} parameter. The cooling rate of the heat sink is set to $4\times10^{-3}\times\theta_{limit}$ and $\theta_{throttle}$ is set to half of θ_{limit}. The resultant heat sink characteristics are listed in Table 4.1.

Table 4.1: A summary of the parameters used to control the heat sink.

Identifier	Maximum Rate of Cooling	Start of Throttling	Potential Temperature Perturbation Limit	Start of Heat Sink Motion	Rate of Heat Sink Motion
C1	-0.064 K s^{-1}	-8 K	-16 K	830 s	20 m s^{-1}
C2	-0.056 K s^{-1}	-7 K	-14 K	880 s	18.935 m s^{-1}
C3	-0.048 K s^{-1}	-6 K	-12 K	940 s	17.778 m s^{-1}
C4	-0.040 K s^{-1}	-5 K	-10 K	1010 s	16.410 m s^{-1}
C5	-0.032 K s^{-1}	-4 K	-8 K	1115 s	14.815 m s^{-1}
C6	-0.024 K s^{-1}	-3 K	-6 K	1255 s	13.061 m s^{-1}
C7	-0.016 K s^{-1}	-2 K	-4 K	1510 s	10.432 m s^{-1}
C8	-0.008 K s^{-1}	-1 K	-2 K	2110 s	6.867 m s^{-1}

Convection is imposed through a heat source applied over an ellipsoid region with its center at a height of 4 km above ground level, a vertical semi-principal axis of 2.5 km, a zonal semi-principal axis of 2 km, and a meridional semi-principal axis of 5 km. The spatial distribution of the heat source amplitude is prescribed by a cosine function. The amplitude of the heat source is 0.048 K s^{-1} with a maximum potential temperature perturbation of 12 K from the base state using the approach of Markowski et al. (2010) that does not include throttling.

Two sets of simulations were performed to evaluate the impact of the heat source motion relative to the gust front. In one set of simulations, the heat source moves with the density weighted mean wind over the layer from 1.5 km to 8.5 km above ground level, resulting in an eastward motion of approximately 1.25 m s^{-1} using the wind profile from the soundings. Because the motion of the gust front is much faster than the motion of the heat source, this simulates a single pass of a convective cell over the gust front. In each of these simulations, the heat source is started slightly upstream from 10 km west of the center of the domain. The heat source is activated 360 s prior to the gust front reaching 10 km west of the domain center such that the heat source is centered directly above the gust

front when it reaches that point. This ensures that the heat source is in an identical state for all the simulations when the gust front passes below. In the second set of simulations, the heat source is anchored over the peak mass flux above the density current, so that the convection moves with the gust front. The convection is initiated at the same time as in the first set of simulations, but it is over the gust front and moves with it. Table 4.2 summarizes the parameters for each of the simulations.

Table 4.2: A summary of the parameters used to control the heat source. The simulation identifier is defined such that the number following the "C" denotes the relative strength of the cold pool (with 1 being strongest/coldest, as in Table 4.1) and a 1 following the "M" denotes a simulation in which the updraft (heat source) moves rearward of the gust front at the speed of the mean wind, and a "2" denotes a simulation in which the updraft is advected with the gust front at a speed proportional to the cold pool strength.

Identifier	**Heat Source Activation Time**	**Heat Source Motion**
C1M1	870 s	Mean wind
C2M1	940 s	Mean wind
C3M1	1025 s	Mean wind
C4M1	1140 s	Mean wind
C5M1	1295 s	Mean wind
C6M1	1515 s	Mean wind
C7M1	1915 s	Mean wind
C8M1	2910 s	Mean wind
C1M2	870 s	24.845 m s^{-1}
C2M2	940 s	23.952 m s^{-1}
C2M3	1025 s	22.222 m s^{-1}
C2M4	1140 s	20.725 m s^{-1}
C2M5	1295 s	18.692 m s^{-1}
C2M6	1515 s	16.736 m s^{-1}
C2M7	1915 s	13.333 m s^{-1}
C2M8	2910 s	8.850 m s^{-1}

4.3. Results

All of the simulations described above produce mesovortices *above the cold pool* through upward tilting of crosswise horizontal vorticity likely generated by the release of Kelvin-Helmholtz instability. This suggests that horizontal vorticity has been vertically displaced from the head of the density current, tilting vorticity on either side of the updraft (Figure 4.2). These vertical vortices are confined above the cold pool and the

circulations do not reach to the surface. Because only upward tilting and ascent are involved in creating these vortices, there is no mechanism to transport the circulation closer to the surface. Although it is very reasonable that mesovortices should develop through this mechanism, it is unlikely that their presence would directly enhance the potential for damaging wind gusts. The vortices that are produced through this mechanism remain anchored to the updraft when the heat source is advected rearward. The demise of these vortices occurs when they move rearward to the heat sink, likely due to sinking air and positive pressure perturbations at low levels, which cause divergent flow that broadens and weakens the vortices. Although the heat sink is highly parameterized, it is realistic that the implicated processes would also be relevant in real downdrafts.

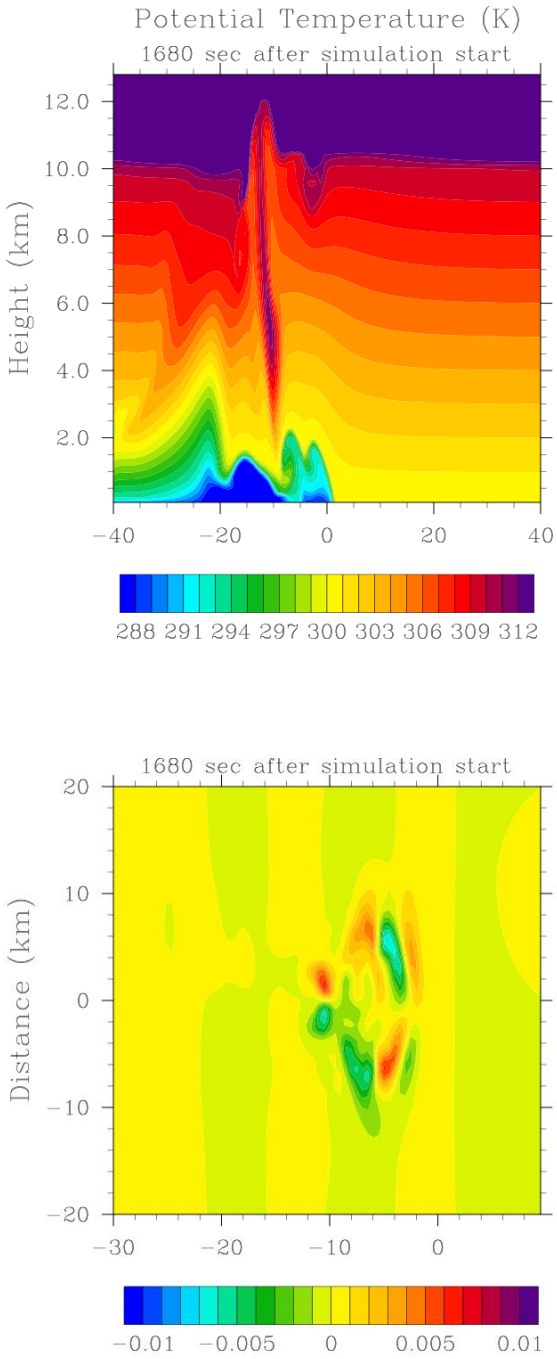

Figure 4.2: A zonal cross-section (top) through the middle of the domain 1680 s after the start of the C1M1 simulation. Two KH billows are evident, indicating the upward displacement of horizontal vorticity generated atop the head of the density current. At the Vertical vorticity (bottom) at a height of 1.68 km shows two vortex couplets associated with upward tilting of horizontal vorticity within the KH billows and downward tilting between the billows causing a vortex couplet with its orientation reversed.

In the simulations that tether the updraft above the gust front, similar mesovortices develop above the gust front but do not reach to the surface. However, several minutes after the development of these mesovortices, downward tilting of crosswise horizontal vorticity occurs rearward of the updraft, as determined through analysis of vortex lines within the cold pool. This mechanism produces a mesovortex couplet initially reaching from the top of the gust front to the surface. The orientation of the vortex couplet is reversed from the upward tilting mechanism, such that the cyclonic mesovortex develops to the south. The resulting vertical vorticity is then stretched to deepen and strengthen the rotation within the mesovortices (Figure 4.3). This produces a larger couplet aloft with an apparently reversed vorticity couplet within as stretching acts on the low-level mesovortices. Unlike when the heat source is advected rearward of the gust front, the updraft does not remain anchored above the mesovortices. Instead, it acts on one horizontal vortex, creating mesovortex couplets as described above, and then moves on to another horizontal vortex, repeating the mechanism. Rather than producing a single vortex couplet that travels rearward with the updraft, mesovortices are generated at discrete intervals that over time result in a series of mesovortex couplets in various stages of development being advected rearward.

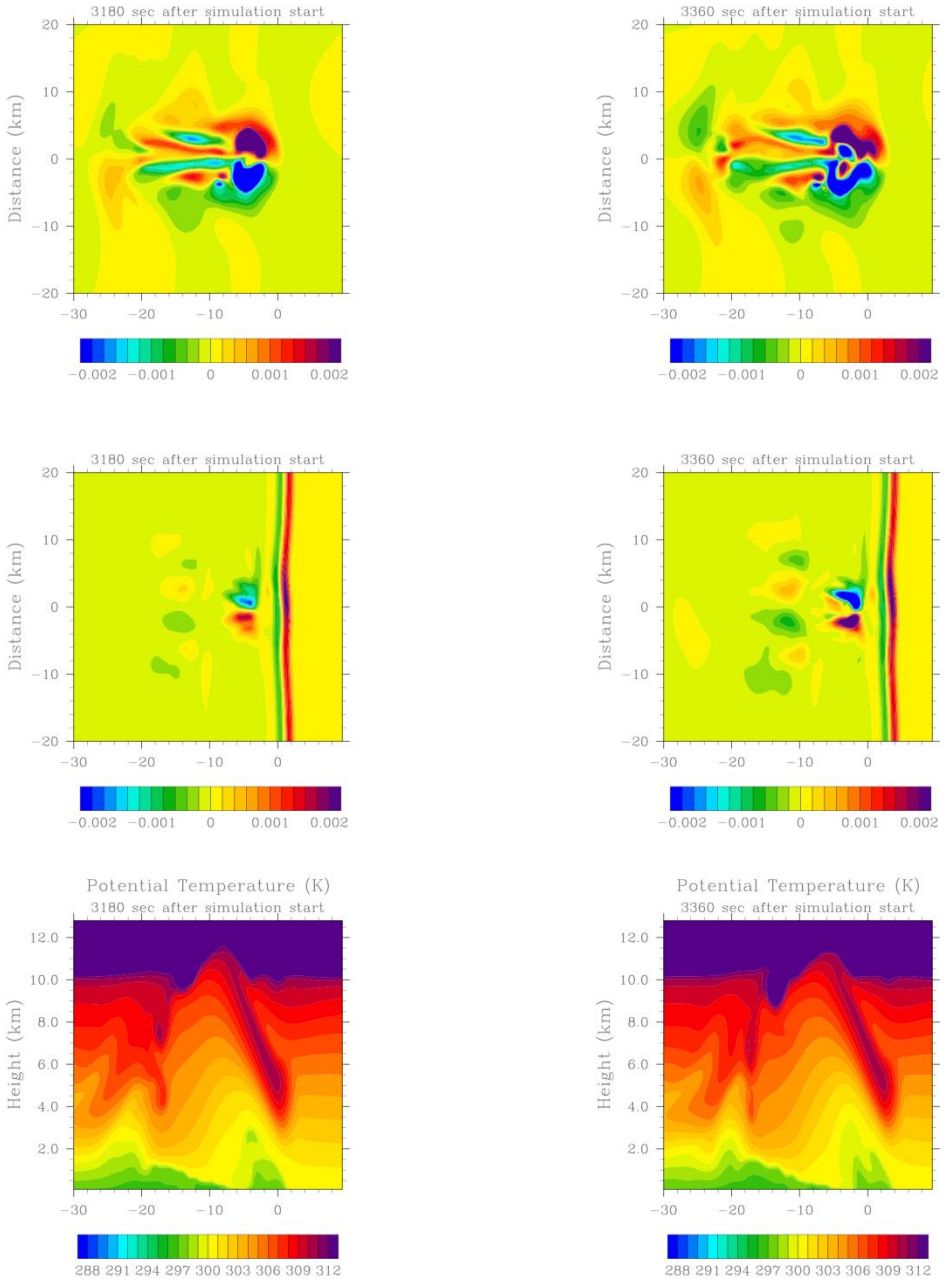

Figure 4.3: Output from the C7M2 simulation, at a time of 3180 s (left) and 3360 s (right). The upper panels show the vertical vorticity in units of s^{-1} at 2 km above ground level, the middle panels show vertical vorticity at the lowest model level, 80 km above the ground, and the bottom panels show cross-sections of potential temperature.

This raises the question of why these processes do not also occur when the heat source and the mesovortices above the gust front are permitted to advect rearward. In the simulations where the updraft advects rearward, the first vortex lines to arch upward are atop the density current. Over time, vortex lines closer to the surface also develop pronounced arches. However, the vortex lines closest to the surface remain nearly horizontal, indicating that the mesovortices do not penetrate all the way to the surface, though they do progress downward. It is possible that, given sufficient time before the heat sink interacts with these vortices that they could become surface-based. To test this, it would be necessary to generate the cold pool through alternative means such as a cold block or by increasing the distance between the heat sink and the gust front. However, there is no evidence that downward tilting of vortex lines occurs at all in the simulations where the heat source is advected rearward, suggesting that tethering the heat source closer to the gust front is necessary to allow the relevant mechanisms to occur. In the simulations where the heat source is tethered to the gust front, following the initial ascent at the bottom of the heat source, a smaller localized region of descent develops behind the heat source. This area of descent does not develop in the simulations where the heat source is advected rearward. The rapid eastward motion of the heat source when tethered to the gust front causes the updraft to be tilted and spread over a wider area than when the heat source is advected rearward. This allows cold air from the density current to be lofted farther upward than would be possible with a single pass from a rearward advected updraft. Once the cold air becomes vertically displaced enough from the updraft (Figure 4.4) it sinks back downward. This is evident by a pocket of cold air aloft, within a KH

billow. The layer between the cold pocket and the top of the density current is absolutely unstable, causing the cold air to accelerate downward, and in the process tilting down horizontal vorticity. The strongest descent occurs at the rear edge of the cold pocket, where the updraft is no longer close enough to the cold air to continue suspending it aloft. Small areas of ascent are evident on the meridional edges of the cold pocket (Figure 4.5). These are highly correlated spatially to the vortices atop the cold pool, which stretch the low-level mesovortices causing them to deepen and intensify. For the stronger cold pools, C4M2 and above, an additional pair of low-level mesovortices extending to the lowest model level is evident at the edges of the aforementioned couplet (Figure 4.6). Analysis of low-level vortex lines indicates a pair of arches on the meridional edges of the descending cold pocket (Figure 4.7). In these stronger cold pools, there is greater descent in the wake of the density current head and a larger gradient in vertical velocity to produce these structures. The primary difference between the simulations in which the updraft is allowed to advect rearward and those where the updraft is tethered to the gust front is that in the latter, the heat source moves and the updraft is spread over a wider area, though the potential temperature perturbations are not quite as large. When the updraft is allowed to advect rearward, parcels remain in the heat sink longer and reach the potential temperature limit, stopping the warming. When the updraft is tethered to the gust front, the heating and ascent is spread over a wider area providing more time for parcels to be lofted, and the overall heating is greater because the cutoff to stop the warming is not reached.

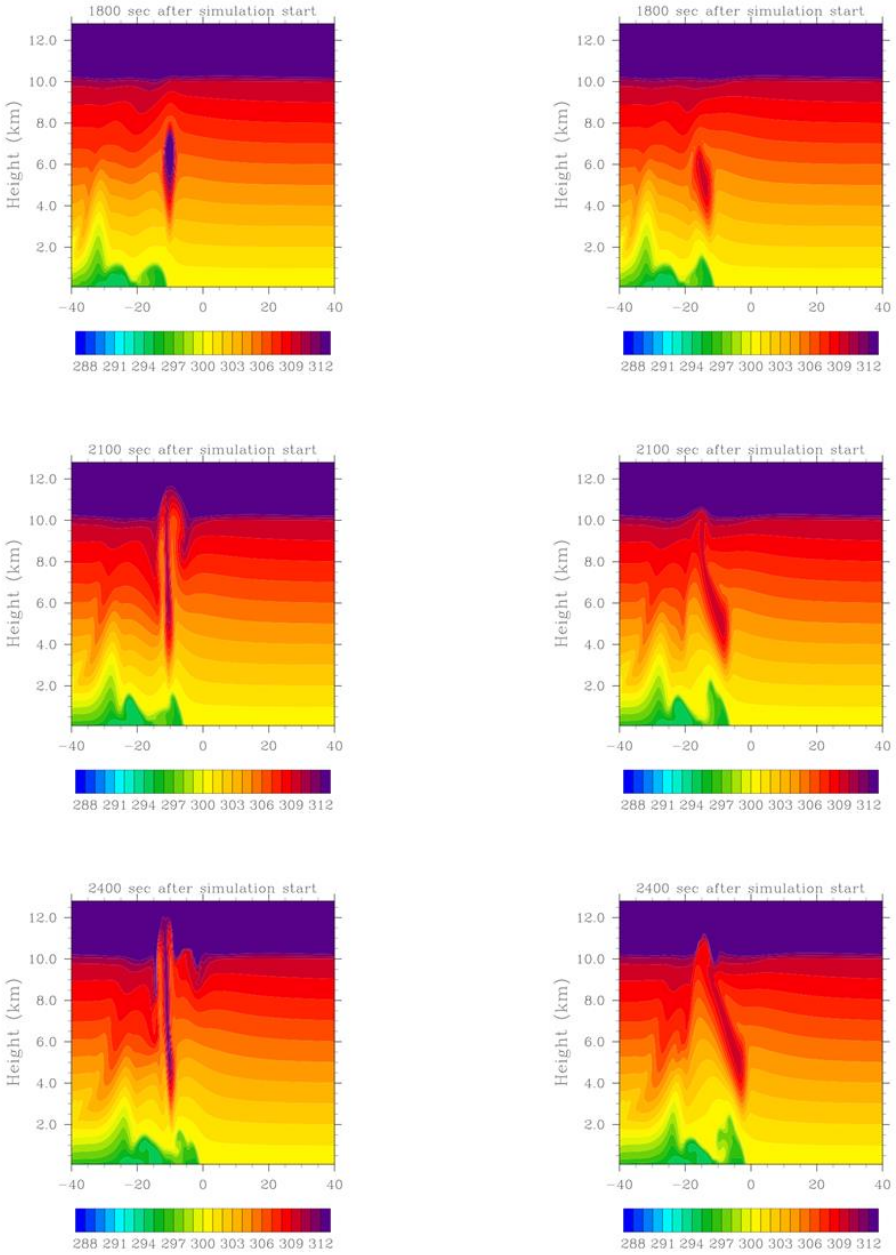

Figure 4.4: Cross sections from 1800 s, 2100 s, and 2400 s into the C6M1 (left) and C6M2 (right) simulations, with the cold pocket/KH billow being lifted from around -10 km at the initial time.

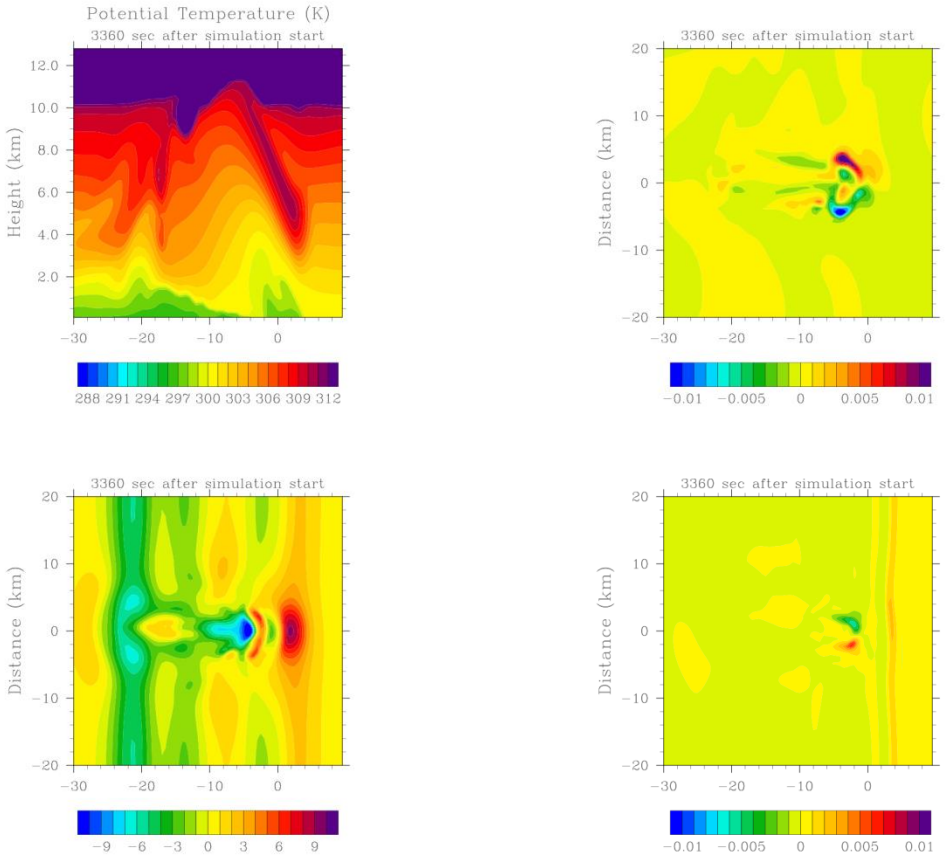

Figure 4.5: The C7M2 simulation after 3360 s, with a cross section of potential temperature (upper-left), the 2 km vertical velocity in m s^{-1} (lower-left), the 2 km vertical vorticity in s^{-1} (upper-right), and the surface vorticity at the lowest model level (lower-right).

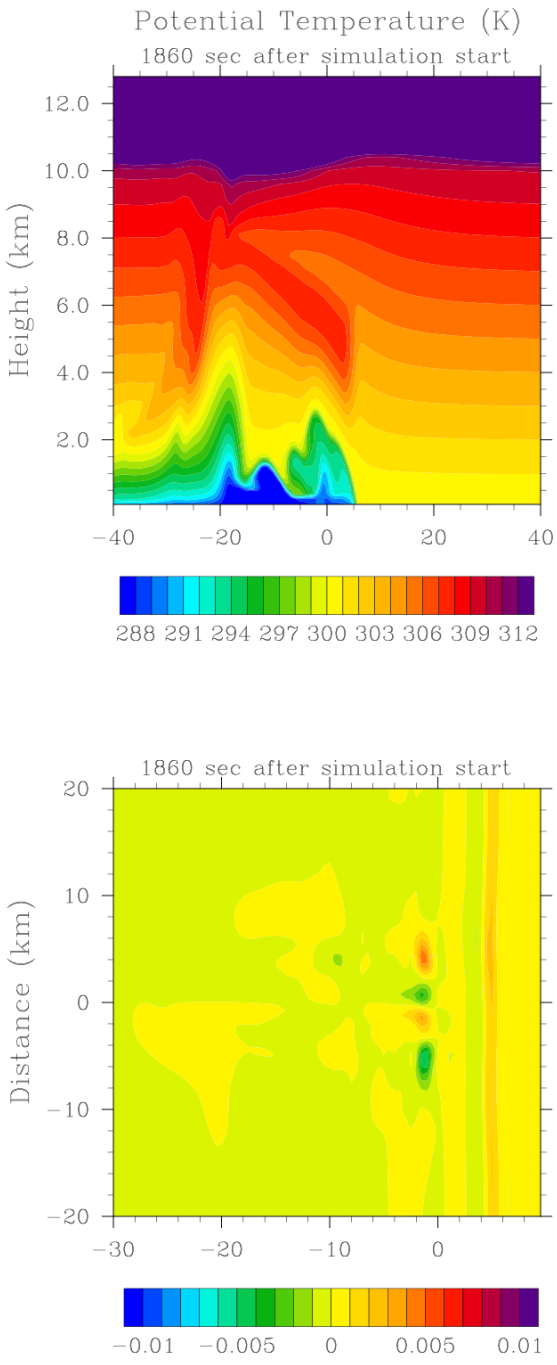

Figure 4.6: Cross section along the zonal axis of potential temperature (top) and vertical vorticity (bottom) in units of s^{-1} at the lowest model level, 80 m above ground level, from the C1M2 simulation, at a time of 1860 s.

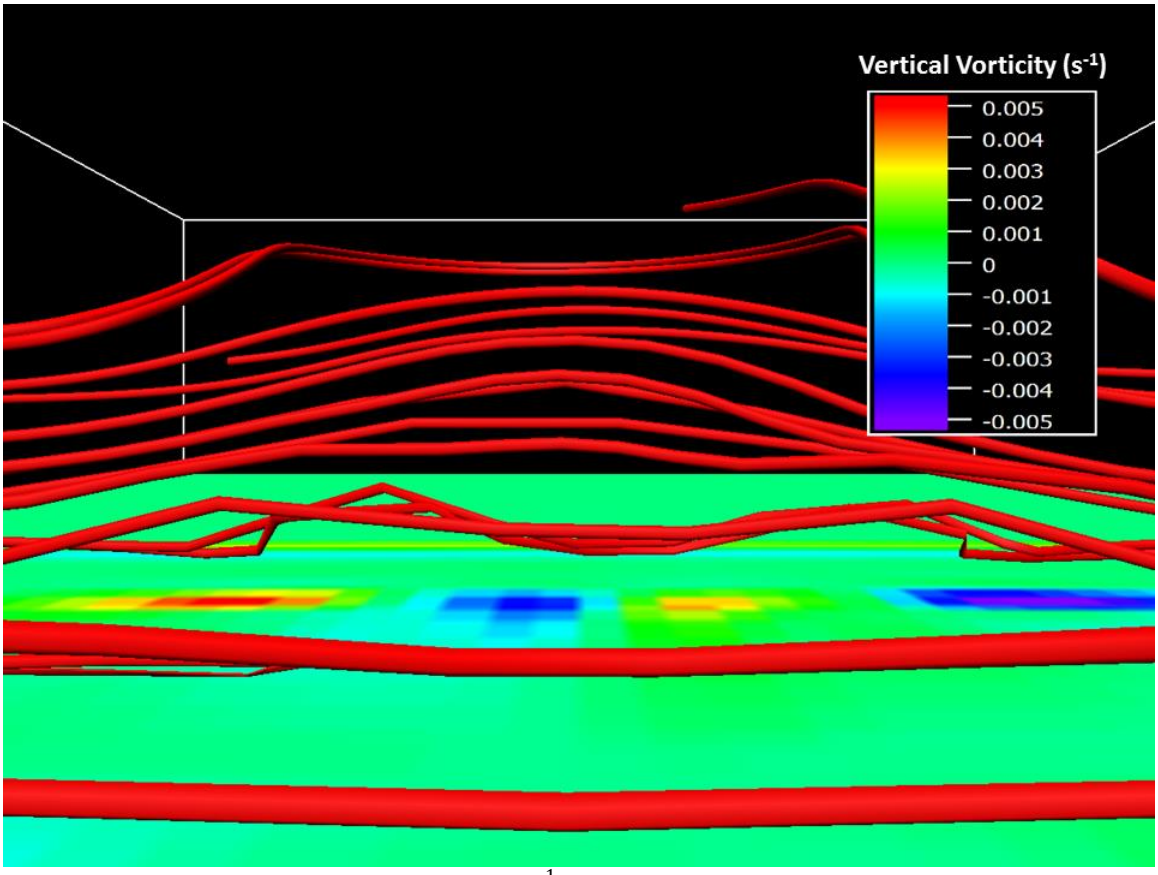

Figure 4.7: Vertical vorticity in units of s^{-1} at the lowest model level, 80 m above ground level, and low-level vortex lines, from the C1M2 simulation, at a time of 1860 s.

Because the primary concern is the production of near-surface vorticity, which does not develop when the heat source is permitted to advect rearward, only the simulations that fix the heat source to the gust front are considered to address the impacts of stability on the ability to generate low-level mesovortices. Regardless of whether upward or downward tilting is involved, increased static stability should add resistance to vertical displacement and limit the ability to tilt horizontal vorticity. This should favor an intermediate state for the optimal generation of low-level vertical vorticity in which the generation of vorticity, whether through the release of Kelvin-Helmholtz Instability or baroclinic processes, is strong but the stability is not too great for the requisite tilting and

stretching. There are many ways to quantify the strength of a vortex including its longevity, diameter, depth, peak vorticity at a given time or throughout the duration of the vortex, etc. However, the diameter is likely related to the scale of the vorticity source and is unlikely to be useful. Longevity and depth are likely to be related to how long the heat source remains over the vorticity. The vertical vorticity tendency was calculated at the lowest model level, 80 m above ground level, from the last time step before the heat source was activated to 10 minutes later (Figure 4.8).

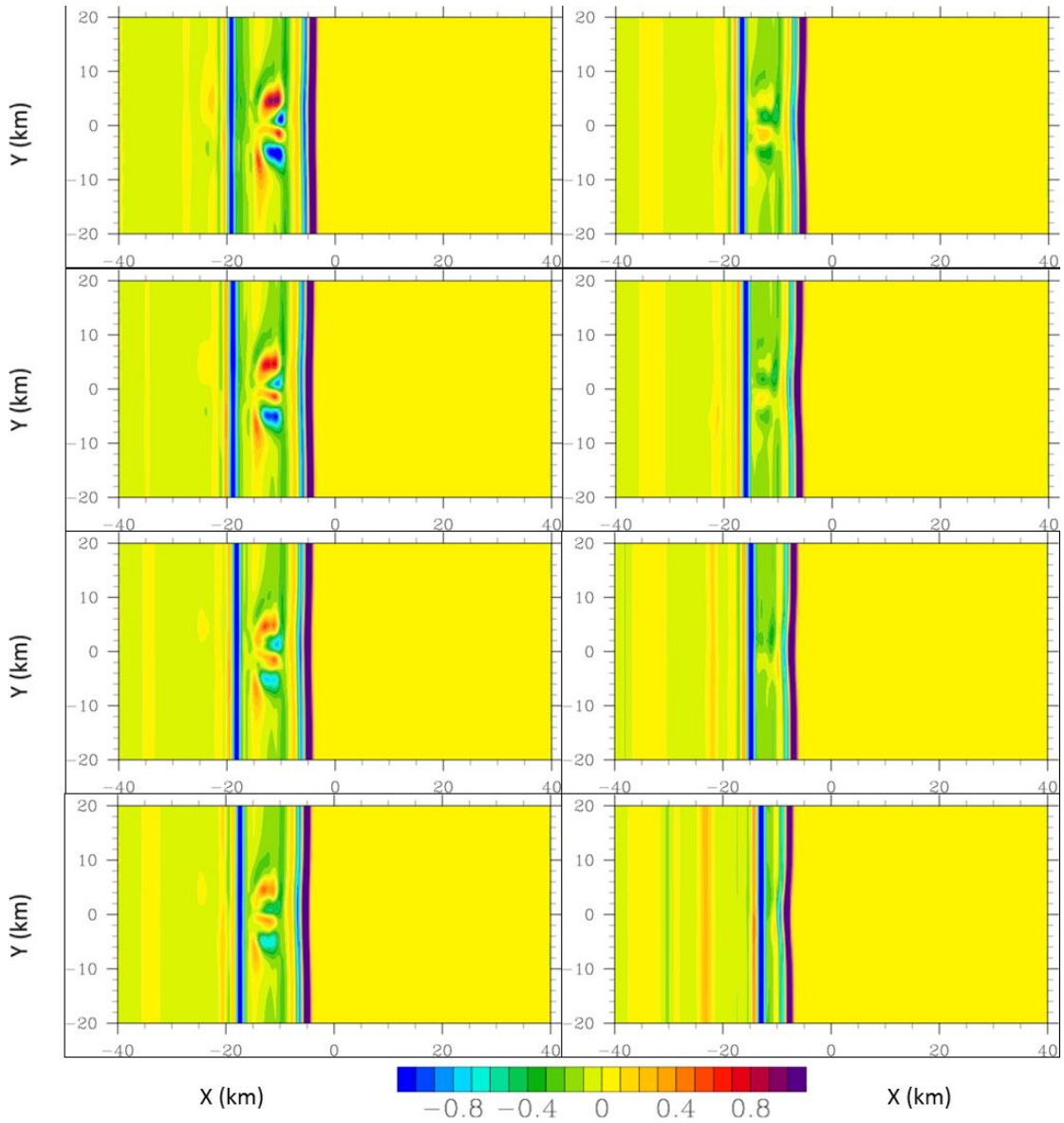

Figure 4.8: Vertical vorticity tendency in units of s^{-2} scaled by 10^6 at the lowest model level, 80 m above ground level. On the left side, the C1M2, C2M2, C3M2, and C4M2 simulations are shown from top to bottom. The right side has C5M2, C6M2, C7M2, and C8M2 from top to bottom.

The vertical vorticity tendency was strongest for the C1M2 simulation, becoming progressively weaker as the strength of the density current was decreased. This is likely due to the origin of the tilting, since the parcels responsible originate within the cold

pool. As shown previously, the downward tilting is caused by lofting a cold pocket upward so that parcels beneath it are absolutely unstable. The instability is strongest when the coldest air is lifted, thus resulting in stronger descending motion and downward tilting. Additionally, the vorticity tendency is strong because the horizontal vorticity is strongest for the C1M2 simulation. However, the generation of vertical vorticity is also influenced by the tilting of horizontal vorticity, which was calculated 10 minutes after the activation of the heat source (Figure 4.9). The strongest tilting appears to occur in the C4M2 simulation. In stronger density currents, the increased stability and resistance to displacing the cold pocket upward likely acts to limit the tilting, though it is still nearly as strong as in the C4M2 simulation. However, because the downward tilting appears to be driven by the creation of the cold pocket and the strength of the instability, weaker density currents are associated with less tilting. Parcels lifted from warmer cold pools have less negative buoyancy and acquire less downward momentum when sinking back into the cold pool, likely limiting some tilting. However, when cold parcels are lifted out of the cold pool, they mix with their environment and there is more potential for colder parcels to warm through mixing and thus have less negative buoyancy when they sink downward. For density currents weaker than in the C4M2 simulation, both the decreased tilting and the weaker source of horizontal vorticity act to limit the strength of vertical vorticity that is generated. However, in the stronger simulations, the horizontal vorticity is stronger and this offsets the small decrease in tilting associated with the increased stability. Because the apparent mechanism for the generation of low-level mesovortices is

different than what is hypothesized to explain tornadogenesis, it should not necessarily be expected that the Goldilocks hypothesis will be applicable to this mechanism.

The applicability of the Goldilocks hypothesis is relevant because stretching of vertical vorticity appears to have a relationship to the cold pool stability. The peak vertical vorticity at each point during the 30 minutes following the activation of the heat source (Figure 4.10) shows that the strongest vortices occur when the cold pool is moderately strong. It appears that there is a greater sensivity to cold pool strength to stretching than tilting. The parcels responsible for causing the tilting downward and initially producing the vertical vorticity originated in the cold pool, and therefore are close to neutrally buoyant when they sink back into the cold pool. However, when the vortices are stretched upward, the environment is not the cold, negatively buoyant density current but the relatively buoyant region above the density current.

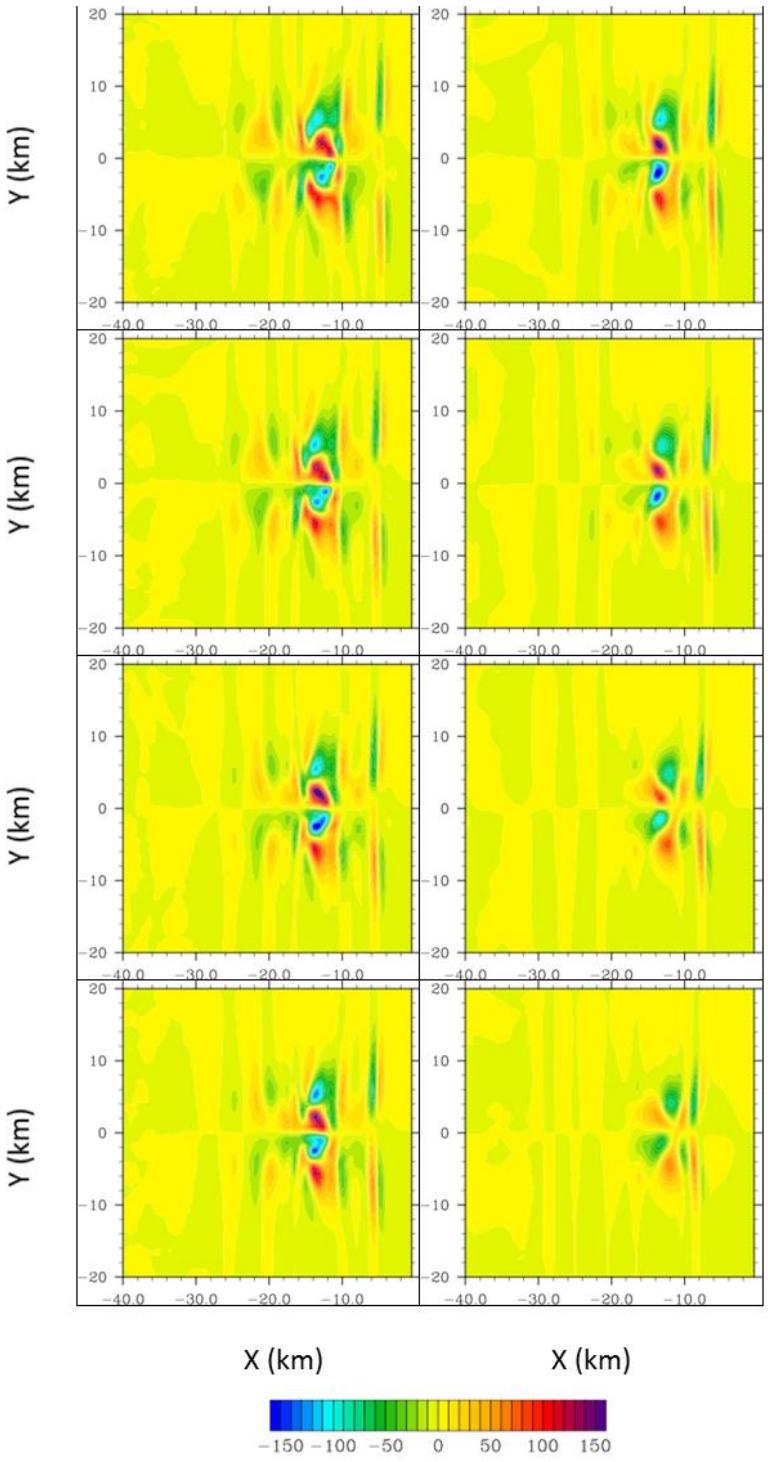

Figure 4.9: Tilting (dw/dy) in units of s-1 scaled by 10^6 at the lowest model level, 80 m above ground level. On the left side, the C1M2, C2M2, C3M2, and C4M2 simulations are shown from top to bottom. The right side has C5M2, C6M2, C7M2, and C8M2 from top to bottom.

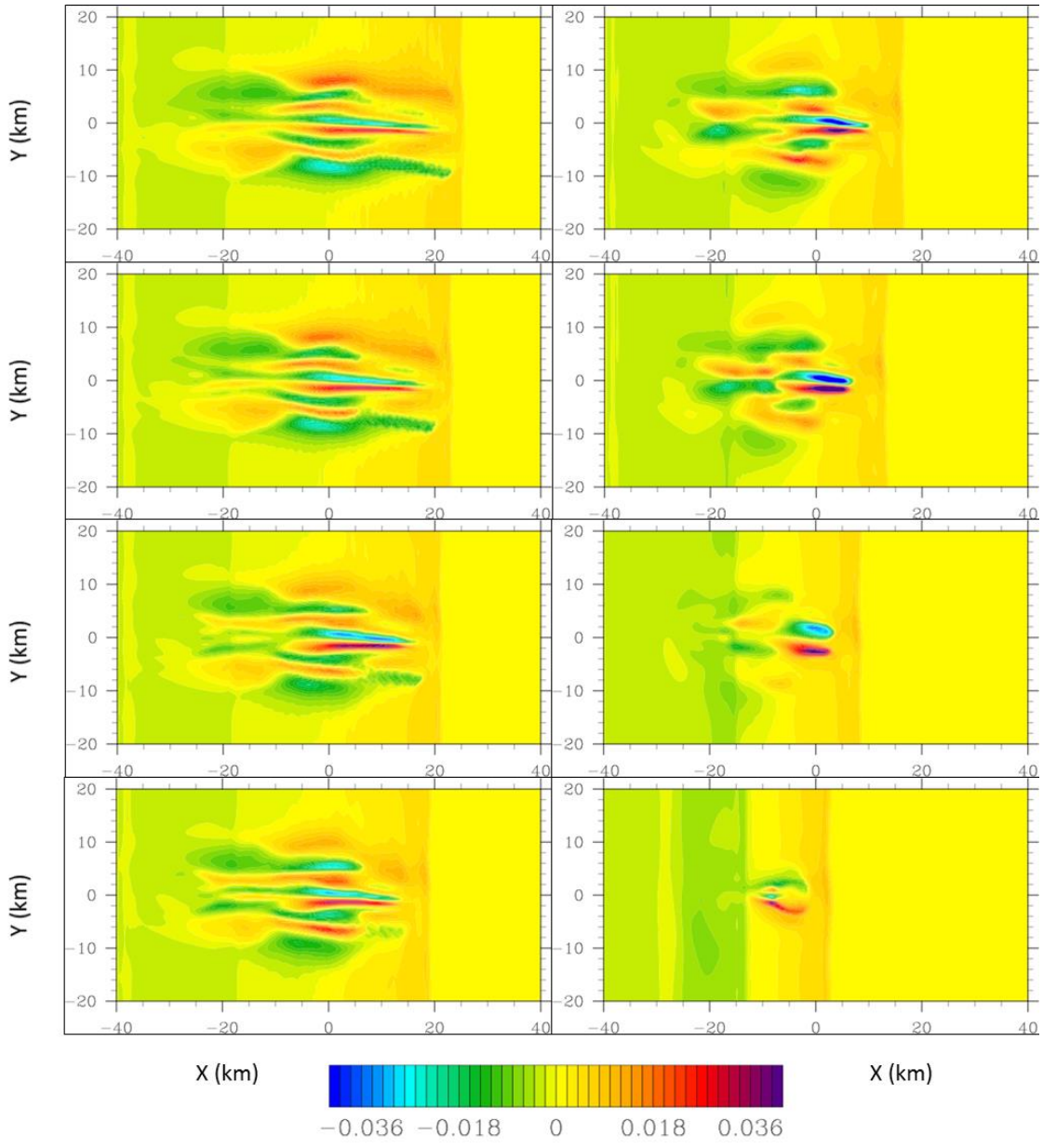

Figure 4.10: Peak vertical vorticity over the 30 minutes after the heat source is activated, in units of s^{-1} at the lowest model level, at a height of 80 m above ground level. On the left side, the C1M2, C2M2, C3M2, and C4M2 simulations are shown from top to bottom. The right side has C5M2, C6M2, C7M2, and C8M2 from top to bottom.

In addition to the 500 m horizontal grid spacing simulations, a second series of simulations were conducted with a horizontal grid spacing of 100 m and a vertical spacing of 50 m at the low levels. All other parameters were the same as the coarser simulations already discussed. In principle, there are seemingly advantages using a finer grid spacing such as better resolution of the head of the density current and mesovortices. However, the 100 m simulations differed substantially from the 500 m simulations. Although numerous vertical vortices developed in the 100 m simulations, they were short-lived and had smaller diameters than their counterparts at 500 m (Figure 4.11). After moving beneath the heat source, numerous horizontal circulations developed on the top of the density current through the same process described at the beginning of the section, resulting in numerous, small vortices. The diameter of these vortices was approximately a few hundred meters, substantially smaller than typical mesovortices. The vortices were short-lived and the vertical vorticity field was dominated by turbulence rather than coherent mesovortices. Even if the vertical vorticity field was smoothed, the structures resolved by the 100 m simulations were not equivalent to those in the 500 m simulations. This is consistent with previous work that evaluated the effects of varying model grid spacing on simulated convection (e.g., Weisman et al. 1997; Bryan et al. 2003; Bryan and Morrison 2012). Bryan et al. (2003) attributed the differences in structures in squall lines between 1 km and 125 m horizontal grid spacing simulations to the ability of higher resolution simulations to resolve turbulent flow that is parameterized at coarser resolutions. The turbulence is amplified by stretching, which results in the numerous, small vortices that are apparent in the vertical vorticity fields.

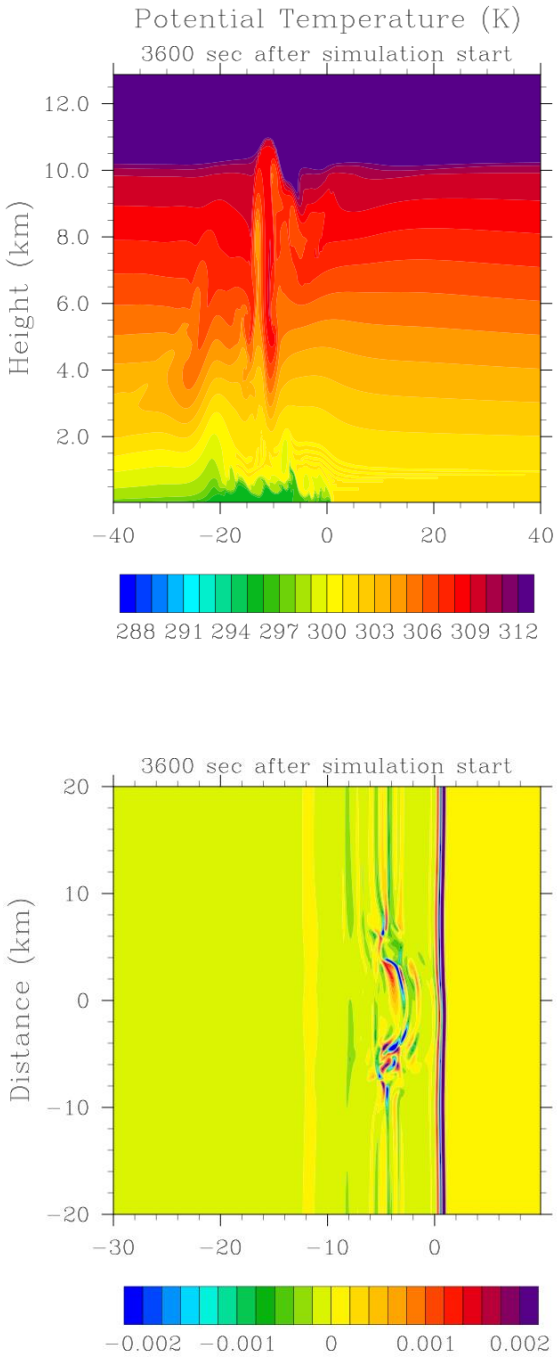

Figure 4.11: Cross-section of potential temperature in the top panel and vertical vorticity in units of s^{-1} in the C6M1 simulation at a height of 0.525 km above ground level after 3600 s.

The differences between the 100 m and 500 m grid spacing can likely be traced to the scale of the source of vertical vorticity. In both cases, the model attempts to produce discontinuities characterized by a strong buoyancy gradient and wind shear at the gust front and atop the density current. However, at coarser resolutions, even if the buoyancy gradient and shear occurs across the same number of grid points as at finer resolutions, the source of vorticity is of a larger scale, thus creating larger vortices. Atop the density current, the instability is governed by the strength of the vertical shear. Even if the bulk wind differential is identical between grid points, by virtue of the different vertical grid spacing, the shear and resulting instability will be weaker for the coarser simulations. If the scale of the vorticity source is held constant between the 100 m and the 500 m simulations, the resulting vortices are similar in scale, though the 100 m resolution better resolves the vortices. Specifically, since the ambient vertical shear is constant between the 100 m and 500 m simulations, the mid-level vortices produced through this process are very similar in diameter (Figure 4.12), indicating that the 100 m simulations can resolve larger vortices provided the source of vorticity is of an appropriately large scale.

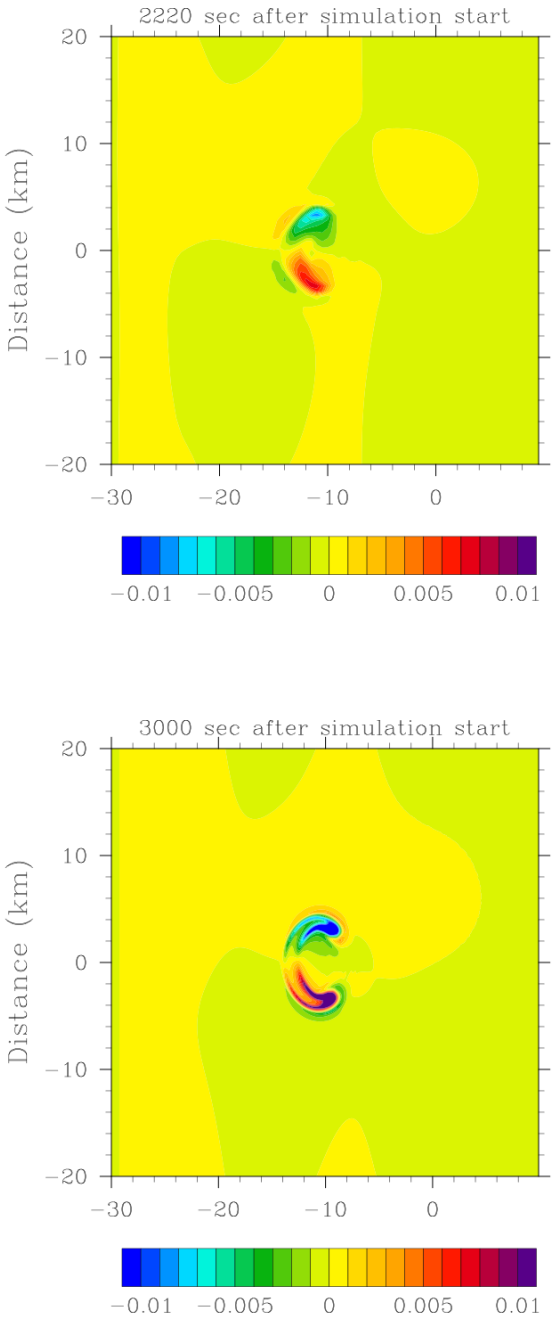

Figure 4.12: Vertical vorticity in two simulations at a height of approximately 5.9 km above ground level. The top panel is simulated at a horiziontal grid spacing of 500 m while the bottom panel has a grid spacing of 100 m.

It is also necessary to consider whether the cold pool structure in the 100 m simulations is realistic. The typical motion of the gust front was on the order of 10 m s^{-1} in the 100 m simulations, meaning that a parcel on the gust front would move from one grid point to the next in a span of approximately 10 seconds. Because the temperature gradient is concentrated within two or three grid points, the buoyancy gradient across the gust front is unrealistic and is inconsistent with observed cold pools such as reported by Engerer et al. (2008, see their Figure 2). A time series of both the 100 m and 500 m simulations shows an almost instantaneous cooling of several degrees with the passage of the gust front (Figure 4.13). Because of the high resolution and the tendency of the model to produce discontinuities, the wind shear at the edge of the density current may be too strong and the source of vorticity may be unrealistically small. Another reason for the discontinuity may be the very large amplitude of the heat sink, rapidly producing large quantities of very cold air that surges outward and produces a discontinuity. It is possible that decreasing the amplitude of the heat sink and conducting the simulation for a longer period of time could produce a similarly strong cold pool but with a weaker temperature gradient at the gust front.

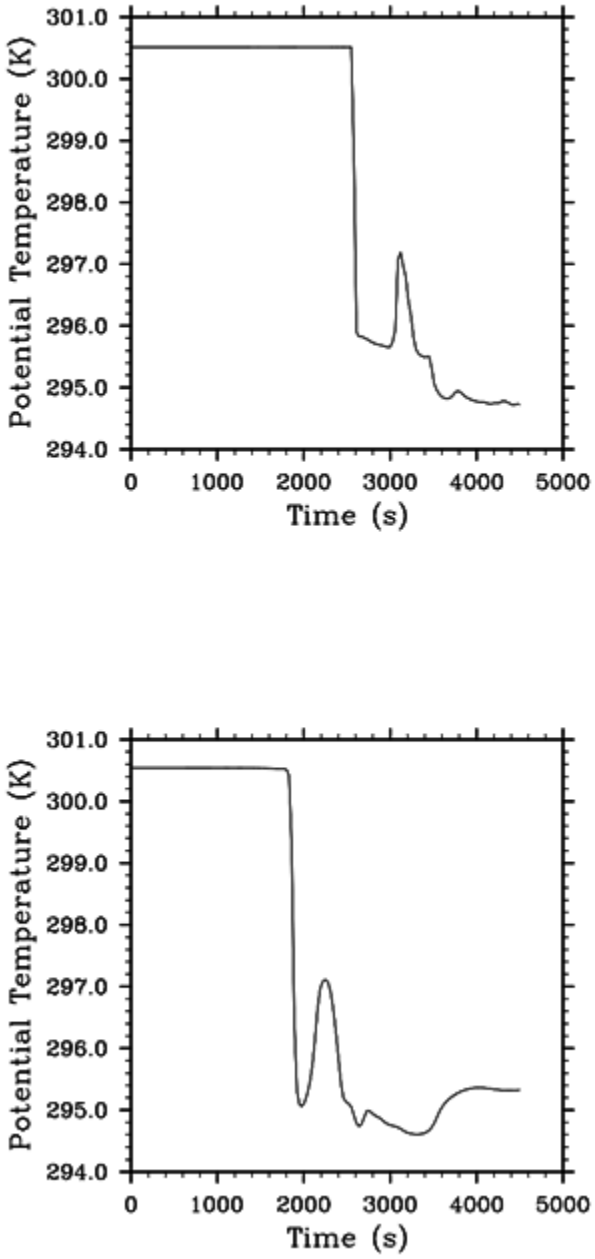

Figure 4.13: A time series of potential temperature at the point 10 km west of the center of the domain at the surface. The top chart is the C6 100 m simulation and the bottom is the C6 500 m simulation.

In summary, the choice of grid point spacing appears to be the primary factor in the scale of the mesovortices that are generated in these simulations. This is because in all simulations, the model attempts to produce a zero order discontinuity at the gust front such that the buoyancy gradient and the scale of the resulting horizontal vorticity are controlled by the grid point spacing to produce unrealistically strong gust fronts. The reasons the model produces such a discontinuity are not entirely certain. However, the ambient easterly flow and the westerly flow in the density current produces strong frontogenesis at the gust front with diffusion that is not sufficiently large to significantly offset the creation of such a strong discontinuity. Additionally, if the surface were initially a constant temperature, heat fluxes would warm the cold side of the boundary more than the warm side, with frontolytic effects; however, heat and moisture fluxes were disabled in these simulations, so this is not a factor here. The scale and behavior of the mesovortices is controlled largely by the very arbitrary choice of the spacing of the grid points and not by physically realistic processes. In the presence of stronger shears that are generated from the finer grid point spacing, the shearing instability is stronger and, when coupled with the ability of higher resolutions to resolve turbulent flow, the turbulent vortices become the dominant low-level circulations instead of the expected mesovortices. When the scale of the vorticity is prescribed, as was the case for the ambient horizontal vorticity that is tilted upward, even the high resolution model is capable of simulating long-lived, coherent vortices of a reasonable scale. Thus, in order to realistically simulate these mesovortices, it would appear necessary to control for the scale of the vorticity source.

4.4. Conclusion

Several numerical simulations were conducted with horizontal grid spacings of 500 m and 100 m to evaluate whether the Goldilocks hypothesis that is proposed to regulate tornadogenesis in supercells is applicable to mesovortex genesis. The simulations were completely dry with a heat sink and heat source to represent the diabatic processes responsible for cold pool generation and the updrafts in moist convection, respectively. Two series of simulations were conducted at 500 m to evaluate the sensitivity of mesovortex generation to the rearward advection of updrafts. When the updrafts were permitted to advect rearward, this resulted in upward tilting of shear vorticity present atop the density current, producing a mesovortex couplet above the cold pool. With time, horizontal vorticity produced by baroclinic generation from temperature gradients deeper in the cold pool was tilted upward, but the vortices never extended all the way to the surface, suggesting that this process alone does not explain the generation of low-level vortices simulated with updrafts that are advected rearward. The vortices generated through this mechanism remained largely underneath the updraft. The ultimate demise of these vortices occurs as they are advected rearward toward the downdraft created by the heat sink.

However, when the updraft remains above the gust front instead of moving rearward, instead of a slow-moving updraft oriented nearly vertically, the updraft becomes tilted back above the density current, spreading the ascent over a wider region. Additionally, many of the parcels forced upward by the updraft are able to move rearward and out from under the region of ascent, allowing them to sink downward.

Although this mechanism does generate mid-level vortices, it is also capable of producing near-surface vortices through downward tilting that occurs when the cold air that was displaced upward sinks back down behind the updraft. The vortices that are produced through downward tilting are intensified through stretching that occurs near the vortices above the cold pool. The optimal case for producing strong, deep mesovortices appears to be when a downdraft brings low-level vertical vorticity in contact with the surface while an updraft acts to displace the vorticity upward accomplishing additional tilting and stretching.

One important assumption in these simulations is that the updraft moves perpendicular to the gust front with all of the diabatic cooling taking place rearward of the updraft (that is, equivalently in a real case, all hydrometeors being deposited rearward of the updraft). This is not entirely realistic because in many squall lines, individual updrafts exhibit a significant line-parallel component to their motion. This allows for the possibility of multiple convective cells interacting simultaneously with the same vortex line such that both an updraft and downdraft are able to tilt and stretch vorticity, maximizing the depth and intensity of the vertical vorticity that is generated. One potential avenue of future work is to investigate the role of line-parallel cell motion to the generation of mesovortices such that relatively deep, low-level vortices are generated, something that is not readily accomplished through the mechanisms simulated here.

The choice of completely dry simulations likely preconditioned the outcome to some degree because the effect of vertical vorticity being brought to the surface by falling hydrometeors was not represented in the simulation. The initial condition of purely zonal

flow prevented any influence of the barotropic mechanism, which was discussed in the previous chapter as an additional process for mesovortex generation, or at least an additional source of cyclonic vorticity. Additionally, in a real environment supportive of mesovortices, it is likely that synoptic-scale cyclonic vorticity would be stretched and favor the cyclonic member of the couplet, a process not represented in these simulations. The selected grid spacing appeared to be responsible for the scale of the mesovortices that were generated, which could also possibly be regulated by the amplitude of the heat sink and the amount of time for which the cold pool was allowed to develop.

In regard to the role of cold pool stability in regulating the generation of mesovortices, the hypothesized relationship between cold pool temperature and tornadogenesis in supercells does not appear directly applicable to the mechanism of low-level mesovortex genesis proposed in this chapter. Instead, sufficiently cold air must be displaced upward by an updraft and then be allowed to sink downward, which tilts down horizontal vorticity that is present within the cold pool. Because colder parcels descend more rapidly, this suggests that stronger cold pools do not necessarily inhibit the generation of low-level vertical vorticity. There does appear to be a point beyond which cold pool stability does resist this downward tilting and limits the tilting and stretching. However, this does not necessarily decrease the strength of the vertical vorticity that is produced because the horizontal vorticity generated under these conditions is sufficient to offset the resistance to vertical motion that is present for stronger cold pools. It is conceivable that the hypothesis could still regulate the upward tilting that produces mesovortices above the cold pool. However, the focus of this chapter is on low-level

mesovortices, and because the mechanism that produces these vortices is different from current hypotheses on tornadogenesis, which does not alone satisfy the Goldilocks hypothesis. This is likely because the potential temperature in the descending parcels is similar to the parcels within the cold pool. However, the Goldilocks hypothesis is relevant because of the role of stability during the stretching of the vortices, which is why the C6M2 simulation eventually produces the strongest vortices.

One apparent caveat of any simulations of mesovortex genesis is that the source of vorticity from the gust front appears to largely be controlled by the grid point spacing of the model, an arbitrary decision when conducting simulations, rather than actual physical processes. This is due to the tendency of the model to create discontinuities regardless of the resolution. This confines the buoyancy gradients and baroclinic vorticity to a smaller area. This is also relevant with respect to shear vorticity atop the cold pool in which a similar wind differential is compressed into a smaller area, although spanning the same number of grid points, resulting in a stronger shear and instability. Although it seems intuitive that higher resolution simulations should be able to resolve turbulent flow that is present in strong cold pools, the turbulence that is generated is likely too strong as a consequence of the unrealistic instabilities produced by the model. For this reason, the 500 m simulations are likely more realistic, especially when resolving features of larger scales such as mesovortices. The ability of the model to tilt ambient vorticity, in which the scale of the source is controlled, and produce vortices of a similar scale regardless of resolution, suggests that it is not that high-resolution models cannot resolve these features but rather that the cold pool is unrealistic. This is underscored by comparing the

temperature gradients in the simulated cold pools to observed cold pools, in which the real cold pools do not have nearly the same cold pool strength.

The main finding of this work is that upward tilting is not alone sufficient to generate low-level vortices. Rather, downward tilting is accomplished as cold pool parcels displaced upward by updrafts are able to sink back downward and tilt down horizontal vorticity as they descend. This process is able to generate low-level vorticity and the resulting vortices can be amplified by upward motion on the flanks of the descending cold pocket. This is a different mechanism than tornadognesis; however, because of the necessity of a strong cold pool to generate strong vorticity and the role of stretching to intensify vertical vorticity, the Goldilocks hypothesis still appears to be relevant.

Chapter 5: Concluding Remarks

The goal of this work was to investigate the processes responsible for the generation of QLCS mesovortices through an observational study and a modeling component. The observational component tracked mesovortices using radar data collected during 44 events from 2009 and 2010 to evaluate the relative frequency and strength of cyclonic and anticyclonic mesovortices and the processes responsible for their generation. However, because the available observations were insufficient to definitively identify the processes responsible for mesovortex formation and some characteristics of the storms responsible for their generation, a modeling component was also conducted. The primary goal of the modeling study was to evaluate the role of cold pool stability in the development of mesovortices. It was initially anticipated that the modeling component would find more evidence of upward tilting of vorticity through the baroclinic mechanism, and that the modeling component would expand upon these findings. However, the importance of the barotropic mechanism and lack of couplets were unexpected findings from the climatology.

Three primary mechanisms for the generation of mesovortices were presented in this dissertation: a barotropic process that produces vortices through shearing instability and the redistribution of ambient vorticity, the upward tilting of crosswise baroclinic vorticity in outflows, and the downward tilting of crosswise baroclinic vorticity. Low-level vorticity appears to be primarily generated through either the barotropic mechanism or the tilting down of baroclinic vorticity whereas mid-level mesovortices appear to be more related to tilting up of baroclinic vorticity.

The mesovortex climatology required tracking of radar-identified circulations through events spanning across the domains of many radars. Because the tracking of circulations in radar data was erratic using the operational algorithm and limited to single-radar domains, a separate algorithm known as the Advanced Algorithm for the Tracking of Objects (AALTO) was developed. AALTO incorporates the best practices of human-based tracking and existing tracking algorithms to generate the best possible tracks. These practices include allowing objects detected by different radars to simultaneously be used to construct tracks, implementing variable search radii for objects to continue existing tracks, and looking both at previous positions and possible future positions along tracks to establish track continuity. Additionally, AALTO is versatile and contains many settings that can be tuned depending on the type of feature being tracked, making it a robust tracking algorithm with applications beyond the scope of the work presented in this dissertation.

In the climatology, cyclonic and anticyclonic mesovortices were independently tracked to determine their relative frequency and characteristics. A large number of anticyclonic mesovortices were found suggesting the role of either one of the baroclinic mechanisms proposed. However, many anticyclonic mesovortices were sufficiently displaced from any cyclonic mesovortices as to suggest a mechanism other than the two baroclinic processes. Low-level shear, especially the line-parallel component, is less important for the generation of anticyclonic mesovortices, and may be less of a factor in the baroclinic processes. The climatology component also found a few events with a disproportionate number of cyclonic mesovortices compared with all events, an outcome

attributed to the barotropic process. The barotropic process generates predominantly cyclonic vortices and appears to be supported by environments with strong low-level line-parallel flow and vertical shear, especially over the lowest 500 m. Barotropic generation is most likely when low-level vertical shear is strong enough that a shearing instability exists and horizontal vorticity can be tilted upward by the gust front.

The modeling component consisted of many idealized simulations with no moisture, and thus no moist convection. Instead, cold pool generation was parameterized through a heat sink and convection was simulated with a heat source. The cold pool strength and the residence time of the heat source above the gust front were varied across simulations. Tilting up of baroclinic horizontal vorticity appears to generate mesovortices above the cold pool regardless of the strength of the cold pool and duration of the heat source over the gust front, but the vortices produced do not reach to the surface. In part this can be explained by the tendency of the most stable parcels to sink to the bottom of the density current and the parcels responsible for vortices above the cold pool originating with less stable parcels at the top of the density current. The development of these vortices is somewhat independent of the processes responsible for the generation of vortices reaching to the surface.

Only the simulations in which the heat source was tethered above the gust front produced mesovortices that extended to the surface. In these simulations, the heat source followed the motion of the gust front resulting in a tilted updraft spanning across a larger area. Parcels within the cold pool are lifted upward before moving rearward and descending back down into the cold pool. Horizontal vorticity is tilted downward by the

sinking air, creating vertical vorticity and stretching it to the surface. Although the updraft immediately begins upward tilting of horizontal vorticity that quickly results in the development of mesovortices above the cold pool, this process is somewhat delayed because of the time needed for the cold parcels that have been lifted to move rearward and sink downward. Although the actual tilting is somewhat diminished by more stable cold pools, it is significantly offset by increased vorticity generation resulting in strong generation of low-level vortices even within the most stable of cold pools. The one link between meosvortices above the cold pool and the near-surface vortices is that pressure perturbations within the mesovortices above the cold pool appear to induce upward motion and stretch the near-surface vortices. The Goldilocks hypothesis is most applicable to the subsequent stretchinig that intensifies the vortices and not to the initial tilting. This is likely because the parcels responsible for the tilting originated in the cold pool and are close to neutrally buoyant with respect to the cold pool. However, parcels originating in the cold pool that are lifted above the cold pool in the stretching process are far less buoyant relative to their environment, such that the stability limits the stretching that can occur in the most stable cold pools. This, when coupled with the weaker generation of horizontal vorticity owing to weaker temperature gradients and vertical shears at the top of the density current in warmer cold pools, explains why the Goldilocks hypothesis is relevant to the stretching and indicates that strong mesovortices are most likely when the cold pool is neither too cold nor too warm.

An additional finding was the dependence of model grid spacing on the scale of mesovortices, which appears to be the primary factor in determining the diameter of these

vortices. Regardless of the grid point spacing, the simulations produce a very strong discontinuity at the gust front, the scale of which is directly related to the grid point spacing. Thus, very high-resolution simulations produced very small vortices and decreasing the resolution produced larger vortices closer in size to observed mesovortices. It is not an issue of the ability of the model to generate large vortices at very fine grid spacing, because when the scale of the source of the vorticity is controlled, the diameter of vertical vortices do not exhibit a strong dependence on model grid spacing.

The principal findings of this work are the large number of anticyclonic mesovortices, the role of barotropic processes in generating low-level cyclonic mesovortices and their relationship to low-level shear, the role of tilting up baroclinic vorticity to produce mid-level mesovortices while tilting down produces low-level mesovortices. Although there is some evidence for the proposed Goldilocks hypothesis that cold pool stability regulates the generation of low-level mesovortices, the process is different from the development of low-level rotation in supercells and the hypothesis is less applicable. It appears that the tilting is, indeed, diminished for more stable cold pools, but this is offset largely by the increased generation of horizontal vorticity available.

References

Atkins, N. T., J. M. Arnott, R. W. Przybylinski, R. A. Wolf, and B. D. Ketcham, 2004: Vortex structure and evolution within bow echoes. Part I: Single-Doppler and damage analysis of the 29 June 1998 derecho. *Mon. Wea. Rev.*, **132**, 2224-2242.

Atkins, N. T., C. S. Bouchard, R. W. Przybylinski, R. J. Trapp, and G. Schmocker, 2005: Damaging surface wind mechanisms within the 10 June 2003 Saint Louis bow echo during BAMEX. *Mon. Wea. Rev.*, **133**, 2275-2296.

Atkins, N. T. and M. St. Laurent, 2009: Bow echo mesovortices. Part II: Their genesis. *Mon. Wea. Rev.*, **137** (5), 1514-1532.

Barjenbruch, B. L., 2008: A technique for developing an objective climatology of supercell and non-supercell thunderstorms, University of Nebraska-Lincoln, 70 pp.

Barjenbruch, B. L. and A. L. Houston, 2006: A technique for developing the ratio of supercell to non-supercell thunderstorms. *Preprints, 23rd Conf. on Severe Local Storms*, Saint Louis, MO, Amer. Meteor. Soc., P2.7.

Benjamin, S. G., and Coauthors, 2004: An hourly assimilation-forecast cycle: The RUC. *Mon. Wea. Rev.*, **132**, 495-518.

Bentley, M. L. and T. L. Mote, 1998: A climatology of derecho-producing mesoscale convective systems in the central and eastern United States, 1986–95. Part I: Temporal and spatial distribution. *Bull. Amer. Meteor. Soc.*, **79**, 2527–2540.

Browning, K. A., 1977: The structure and mechanisms of hailstorms. *Hail: A Review of Hail Science and Hail Suppression, Meteor. Monogr.*, No. 38, Amer. Meteor. Soc., 1-43.

Bryan, G. H. and J. M. Fritsch, 2002: A benchmark simulation for moist nonhydrostatic numerical models. *Mon. Wea. Rev.*, **130**, 2917-2928.

Bryan, G. H., J. C. Wyngaard and J. M. Fritsch, 2003: Resolution requirements for the simulation of deep moist convection. *Mon. Wea. Rev.*, **131**, 2394-2416.

Bryan, G. H. and H. Morrison, 2012: Sensitivity of a simulated squall line to horizontal resolution and parameterization of microphysics. *Mon. Wea. Rev.*, **140**, 202-225.

Bunkers, M. J., B. A. Klimowski, J. W. Zeitler, R. L. Thompson, and M. L. Weisman, 2000: Predicting supercell motion using a new hodograph technique. *Wea. Forecasting*, **15**, 61-79.

Carbone, R. E., 1983: A severe frontal rainband. Part II: Tornado parent vortex circulation. *J. Atmo. Sci.*, **40**, 2639-2654.

Chalon, J.-P., J. C. Fankhauser and P. J. Eccles, 1976: Structure of an evolving hailstorm. Part I: General characteristics and cellular structure. *Mon. Wea. Rev.*, **104**, 564.575.

Craven, J. P. and H. E. Brooks, 2004: Baseline climatology of sounding derived parameters associated with deep moist convection. *Nat. Wea. Digest*, **28**, 13-24.

Coniglio, M. C. and D. J. Stensrud, 2004: Interpreting the climatology of derechos. *Wea. Forecasting*, **19**, 595–605.

Dixon, M. and G. Wiener, 1993: TITAN: Thunderstorm identification, tracking, analysis, and nowcasting – A radar-based methodology. *J. Atmos. Oceanic Technol.*, **10**, 785–797.

Donelan, M. A., B. K. Haus, N. Reul, W. J. Plant, M. Stiassnie, H. C. Graber, O. B. Brown, and E. S. Saltzman, 2004: On the limiting aerodynamic roughness of the ocean in very strong winds. *Geophys.Res. Lett.,* **31,** L18306, doi:10.1029/2004GL019460.

Droegemeier, K. K. and R. B. Wilhelmson, 1985: Three-dimensional numerical modeling of convection produced by interacting thunderstorm outflow. Part I: Control simulation and low-level moisture variations. *J. Atmos. Sci.*, **42**, 2381-2403.

Dudhia, J., and M. W. Moncrieff, 1989: A three-dimensional numerical study of an Oklahoma squall line containing rightflank supercells. *J. Atmos. Sci.,* **46,** 3363–3391.

Dunn, J. and T. Best, 2010: Bow echo and mesovortex evolution during the 2 May 2007 North Texas derecho. *Electronic J. Severe Storms Meteor.*, **6** (4), 1-25.

Dupilka, M. L. and G. W. Reuter, 2006: Forecasting tornadic thunderstorm potential in Alberta using environmental sounding data. Part I: Wind shear and buoyancy. *J. Atmos. Sci.*, **21**, 325-335.

Earth System Research Laboratory, cited 2013: RUC variables. [Available online at ruc.noaa.gov/vartxt.html.].

Engerer, N. A., D. J. Stensrud and M. C. Coniglio, 2008: Surface characteristics of observed cold pools. *Mon. Wea. Rev.*, **136**, 4839-4849.

Esterheld, J. M. and D. J. Giuliano, 2008: Discriminating between tornadic and non-tornadic supercells: A new hodograph technique. *Electronic J. Severe Storms Meteor.*, **3**, 1-50.

Fairall, C. W., E. F. Bradley, J. E. Hare, A. A. Grachev, J. B. Edson, 2003: Bulk parameterization of air–sea fluxes: Updates and verification for the COARE algorithm. *J. Climate*, **16**, 571–591.

Fovell, R. G., 2003: Role of the rear inflow in organizing convective storms. Preprints, *10th. Conf. on Mesoscale Processes*, Portland, OR, Amer. Meteor. Soc., P1.1.

Fovell, R. G. and Y. Ogura, 1988: Numerical simulation of a midlatitude squall line I two dimensions. *J. Atmos. Sci.*, **45**, 3846-3879.

Fovell, R. G. and Y. Ogura, 1989: Effect of vertical wind shear on numerically simulated storm structure. *J. Atmos. Sci.*, **46**, 3144-3176.

Fovell, R. G., and P-H. Tan, 2000: A simplified squall-line model revisited. *Quart. J. Roy. Meteor. Soc.*, **126,** 173–188.

Gallus Jr., W. A., N. A. Snook and E. V. Johnson, 2008: Spring and summer severe weather reports over the Midwest as a function of convective mode: A preliminary study. *Wea. Forecasting*, **23**, 101-113.

Garner, S. T., and A. J. Thorpe, 1992: The development of organized convection in a simplified squall-line model. *Quart. J.Roy. Meteor. Soc.*, **118,** 101–124.

Grzych, M. L., B. D. Lee and C. A. Finley, 2007: Thermodynamic analysis of supercell rear-flank downdrafts from Project ANSWERS. *Mon. Wea. Rev.*, **135**, 240-246.

Johns, R. H. and C. A. Doswell, 1992: Severe local storms forecasting. *Wea. Forecasting*, **7**, 588–612.

Johns, R. H. and W. D. Hirt, 1987: Derechos: widespread convectively induced windstorms. *Wea. Forecasting*, **2**, 32–49.

Johnson, J. T., P. L. MacKeen, A. Witt, E. D. Mitchell, G. J. Stumpf, M. D. Eilts, K. W. Thomas, 1998: The storm cell identification and tracking algorithm: An enhanced WSR-88D algorithm. *Wea. Forecasting*, **13**, 263–276.

Jones, T. A., K. M. McGrath, J. T. Snow, 2004: Association between NSSL mesocyclone detection algorithm-detected vortices and tornadoes. *Wea. Forecasting*, **19**, 872–890.

Junyent, F., V. Chandrasekar, D. McLaughlin, E. Insanic and N. Bharadwaj, 2010: The CASA integrated project 1 networked radar system. *J. Atmos. Oceanic Technol.*, **10** (1), 61-78.

Kerr, B. W. and G. L. Darkow, 1996: Storm-relative winds and helicity in the tornadic thunderstorm environment. *Wea. Forecasting*, **11**, 489-505.

Lahowetz, J., A. Houston, G. Limpert, A. Gibbs, and B. Barjenbruch, 2010: A technique for developing a US climatology of thunderstorms: The ThOR Algorithm. *Preprints, 25th Conf. on Severe Local Storms*, Denver, CO, Amer. Meteor. Soc., 16B.1.

Lakshmanan, V., K. Hondl, and R. Rabin, 2009: An efficient, general-purpose technique for identifying storm cells in geospatial images. *J. Ocea. Atmos. Tech.*, **26**, 523-537.

Lakshmanan, V. and T. Smith, 2010: An objective method of evaluating and devising storm tracking algorithms. *Wea. Forecasting*, **29**, 721-729.

Lakshmanan, V., T. Smith, G. Stumpf, and K. Hondl, 2007: The Warning Decision Support System–Integrated Information. *Wea. Forecasting*, **22**, 596–612.

Lakshmanan, V., T. Smith, K. Hondl, G. J. Stumpf, and A. Witt, 2006: A real-time, three dimensional, rapidly updating, heterogeneous radar merger technique for reflectivity, velocity and derived products. *Wea. Forecasting*, **21**, 802-823.

Lee, B. D. and R. B. Wilhelmson, 1997: The numerical simulation of non-supercell tornadogenesis. Part I: Initiation and evolution of pretornadic misocyclone circulations along a dry outflow boundary. *J. Atmos. Sci.*, **54**, 32-60.

Lee, B. D. and R. B. Wilhelmson, 2000: The numerical simulation of nonsupercell tornadogenesis. Part III: Parameter tests investigating the role of CAPE, vortex sheet strength, and boundary layer vertical shear. *J. Atmos. Sci.*, **57**, 2246-2261.

Lese, A., 2006: Observations and quantification of low-level mesovortex evolution within the 4 July 2004 southwest Missouri high wind event. Preprints, *23rd Conf. on Severe Local Storms*, Saint Louis, MO, Amer. Meteor. Soc., 6.1.

Lese, A. D. and S. Martinaitis, 2010: Observations and quantification of counter-rotating mesovortex couplets within the 8 May 2009 southern Missouri derecho. Preprints, *25th Conf. on Severe Local Storms*, Denver, CO, Amer. Meteor. Soc., 3B.3.

Lin, Y-L., and L. E. Joyce, 2001: A further study of the mechanisms of cell regeneration, propagation, and development within two-dimensional multicell storms. *J. Atmos. Sci.*, **58,** 2957–2988.

MacKeen, P. L., H. E. Brooks, and K. L. Elmore, 1999: Radar reflectivity-derived thunderstorm parameters applied to thunderstorm longevity forecasting. *Wea. Forecasting*, **14** (2), 289-295.

Markowski, P. M., 2002: Hook echoes and rear-flank downdrafts: A review. *Mon. Wea. Rev.*, **130**, 852-876.

Markowski, P. M., E. N. Rasmussen and J. M. Straka, 1998: The occurrence of tornadoes in supercells interacting with boundaries during VORTEX-95. *Wea. Forecasting*, **13**, 852-859.

Markowski, P. M., J. M. Straka and E. N. Rasmussen, 2002: Direct surface thermodynamic observations within the rear-flank downdrafts of nontornadic and tornadic supercells. *Mon. Wea. Rev.*, **130**, 1692-1721.

Markowski, P. M. J. M. Straka and E. N. Rasmussen, 2003: Tornadogenesis resulting from the transport of circulation by a downdraft: Idealized numerical simulations. *J. Atmos. Sci.*, **60**, 795-823.

Markowski, P., Y. Richardson, E. Rasmussen, J. Straka, R. Davies-Jones and R. J. Trap, 2008: Vortex lines within low-level mesocyclones obtained from pseudo-dual-doppler radar observations. *Mon. Wea. Rev.*, **136**, 3513-3535.

Markowski, P. M., M. Majcen, and Y. Richardson, 2010: Near-surface vortexgenesis in idealized three-dimensional numerical simulations involving a heat source and a heat sink in a vertically sheared environment. Preprints, *25th Conf. on Severe Local Storms*, Denver, Co, Amer. Meteor. Soc., P1.1.

Mesigner, F. and Coauthors, 2006: North American Regional Reanalysis. *Bull. Amer. Meteor. Soc.*, **87**, 343-360.

Miller, D. J., 2006: Observations of low level thermodynamic and wind shear profiles on significant tornado days. Preprints, *23rd Conf. on Severe Local Storms*, Saint Louis, MO, Amer. Meteor. Soc.

Mitchell, E. D., S. V. Vasiloff, G. J. Stumpf, A. Witt, M. D. Eilts, J. T. Johnson and K. W. Thomas, 1998: The National Severe Storms Laboratory tornado detection algorithm. *Wea. Forecasting*, **13**, 352-366.

Montiverdi, J. P., C. A. Doswell, III and G. S. Lipari, 2003: Shear parameter thresholds for forecasting tornadic thunderstorms in northern and central California. *Wea. Forecasting*, **18**, 357-370.

Mueller, C. K. and R. E. Carbone, 1987: Dynamics of a thunderstorm outflow. *J. Atmo. Sci.*, **44** (15), 1879-1898.

Oppermann, C. D. and A. L. Houston, 2012: A climatology of Great Plains supercells from 2005-2007. Preprints, *26th Conf. on Severe Local Storms*, Nashville, TN, Amer. Meteor. Soc., P4.64.

Przybylinski, R. W., G. K. Schmocker, and Y-J Lin, 2000: A study of storm and vortex morphology during the "intensifying stage" of severe wind mesoscale convective systems. Preprints, *20th. Conf on Severe Local Storms*, Orlando, FL, Amer. Meteor. Soc., 173-176.

Rayleigh, Lord, 1880: On the instability of certain fluid motions. *Proc. London Math. Soc.*, **11**, 57.

Roberts, R. D. and J. W. Wilson, 1995: The genesis of three nonsupercell tornadoes observed with dual-doppler radar. *Mon. Wea. Rev.*, **123**, 3408-3436.

Rotunno, R., J. B. Klemp and M. L. Weisman, 1988: A theory for strong, long-lived squall lines. *J. Atmos. Sci.*, **45**, 463-485.

Schmocker, G. K., R. W. Przybylinski, and E. N. Rasmussen, 2000: The severe bow echo event of 14 June 1998 over the mid-Mississippi Valley region: A case of vortex development near the intersection of a preexisting boundary and a convective line. Preprints, *20th Conf. on Severe Local Storms*, Orlando, FL, Amer. Meteor. Soc., 169-172.

Straka. J. M., E. N. Rasmussen, R. P. Davies Jones and P. M. Markowski, 2007: An observational and idealized numerical examination of low-level counter-rotating vortices toward the rear flank of supercells. *Electron. J. Severe Storms Meteor.*, **2**, 1-22.

Stumpf, G. J., A. Witt, E. D. Mitchell, P. L. Spencer, J. T. Johnson, M. D. Eilts, K. W. Thomas, and D. W. Burgess, 1998: The National Severe Storms Laboratory mesocyclone detection algorithm for the WSR-88D. *Wea. Forecasting*, **13**, 304–326.

Thompson, R. L., R. Edwards, J. A. Hart, K. L. Elmore and P. M. Markowski, 2003: Close proximity soundings within supercell environments obtained from the Rapid Update Cycle. *Wea. Forecasting*, **18**, 1243-1261.

Thorpe, A. J. and M. J. Miller, 1978: Numerical simulations showing the role of the downdraft in cumulonimbus motion and splitting. *Quart. J. Roy. Meteor. Soc.*, **104**, 873-893.

Trapp, R. J., G. J. Stumpf, K. L. Manross, 2005: A reassessment of the percentage of tornadic mesocyclones. *Wea. Forecasting*, **20**, 680–687.

Trapp, R. J. and M. L. Weisman, 2003: Low-level mesovortices within squall lines and bow echoes. Part II: Their genesis and implications. *Mon. Wea. Rev.*, **131** (11) 2804-2823.

Trapp, R. J., D. M. Wheatley, N. T. Atkins, R. W. Przybylinski, and R. Wolf, 2006: Buyer beware: some words of caution on the use of severe wind reports in postevent assessment and research. *Wea. Forecasting*, **21**, 408–415.

Wakimoto, R. M., H. V. Murphey, C. A. Davis and N. T. Atkins, 2006: High winds generated by bow echoes. Part II: The relationship between the mesovortices and damaging straight-line winds. *Mon. Wea. Rev.*, **134** (10), 2813-2829.

Wakimoto, R. M. and J. W. Wilson, 1989: Non-supercell tornadoes. *Mon. Wea. Rev.*, **117**, 1113-1140.

Weisman, M. L., 1992: The role of convectively generated rear-inflow jets in the evolution of long-lived mesoconvective systems. *J. Atmos. Sci.*, **49**, 1826-1847.

Weisman, M. L., W. C. Skamarock and J. B. Klemp, 1997: The resolution dependence of explicitly modeled convective systems. *Mon. Wea. Rev.*, **125**, 527-548.

Weisman, M. L. and C. A. Davis, 1998: Mechanisms for the generation of mesoscale vortices within quasi-linear convective systems. *J. Atmos. Sci.*, **55**, 2603-2622.

Wheatley, D. M., R. J. Trapp and N. T. Atkins, 2006: Radar and damage analysis of severe bow echoes observed during BAMEX. *Mon. Wea. Rev.*, **134** (3), 791-806.

Wheatley, D. M. and R. J. Trapp, 2008: The effect of mesoscale heterogeneity on the genesis and structure of mesovortices within quasi-linear convective systems. *Mon. Wea. Rev.*, **136**, 4220-4241.

Wilhelmson, R. B. and C.-S. Chen, 1982: A simulation of the development of successive cells along the cold outflow boundary. *J. Atmos. Sci.*, **39**, 1466-1483.

Xu, Q, 1992: Density currents in shear flows – A two fluid model. *J. Atmos. Sci.*, **49**, 511-524.